MAPPING FOREST ABOVEGROUND BIOMASS IN THE BRAZILIAN AMAZON USING AIRBORNE LIDAR, LANDSAT IMAGERY, AND DEEP LEARNING

A DISSERTATION SUBMITTED TO THE GRADUATE DIVISION
OF THE UNIVERSITY OF HAWAIʻI AT MĀNOA IN PARTIAL
FULFILLMENT OF THE REQUIREMENTS FOR THE DEGREE OF

DOCTOR OF PHILOSOPHY
IN
GEOGRAPHY AND ENVIRONMENT
DECEMBER 2021

By
Qian Zhang

Dissertation Committee:
Qi Chen (Chair)
Tomoaki Miura (University Representative)
David Beilman
Yan Yan Wu
Yi Qiang

Keywords: Remote sensing, Brazilian Amazon, Tropical forest, forest aboveground biomass, Deep learning

ABSTRACT

The Amazon forest is playing a critical role in the global carbon cycle and implementation of Reduce Deforestation and Forest Degradation (REDD+). However, the range of possible carbon emissions in this region is broad. Most carbon in the Amazon forest is stored in biomass and biomass can be the potential carbon emission when disturbances occur (e.g., deforestation, degradation, and fires). Therefore, the accurate estimation of biomass can help better predict carbon emissions in the Amazon forest. However, the biomass estimations of previous studies show little agreement on their values and spatial distributions in this region. In addition, deforestation and degradation in the Brazilian Amazon have changed significantly from large-scale patterns to fine-scale patterns since the early 2000s. However, existing biomass maps for the Brazilian Amazon forests are limited in capacity to capture fine-scale biomass variations due to their coarse spatial resolutions. Besides, due to the high level of biomass and heterogeneity of tropical forests, the commonly used regression models perform worse in tropical forests compared to boreal and temperate forests. Deep learning is a promising way to improve the accuracy of biomass estimations, which are increasing in success across a variety of remote sensing tasks. The application of deep learning models in estimating forest biomass is still in a nascent stage. Given the aforementioned research gaps, this research proposed a deep learning framework to estimate and map aboveground biomass on a fine-scale for the Brazilian Amazon with inventory data, airborne LiDAR data, and Landsat imagery. Three stages are involved in the framework development.

In the first stage, a multiplicative power model was developed to link airborne LiDAR metrics with biomass inventory data. To determine the best fitting approach to estimate parameters for the multiplicative power model, three multiplicative power models fitted by nonlinear least-square (NLR), linear ordinary least-square (OLSR), and weighted linear least-square (WLSR) were compared by ANOVA and Tukey's Test. The results show that significant performance differences existed among the three models at a 99% confidence level. More extreme predictions and lower accuracies were produced by NLR compared to OLSR or WLSR. OLSR had the most accurate prediction performance. Accordingly, OLSR was used to fit the LiDAR-based model that was used in the subsequent stages to calculate biomass for each LiDAR transect in the Brazilian Amazon forests.

In the second stage, a deep feedforward fully connected neural network (DNN) model was developed to estimate and map aboveground biomass with airborne LiDAR data and Landsat 8 imagery. The effects of hyperparameter values on the DNN model performances were comprehensively investigated. The results show that the model with Scaled Exponential Linear Unit (SELU) had the best performance compared to other activation functions. Besides, both too large and too small learning rates could not achieve optimal results. The learning rate of 0.001 was chosen for the Adam optimizer. The DNN model with these optimal hyperparameters significantly outperformed the Random Forest model, Support Vector Regression model, and linear regression model with the R^2 of 0.64 and RMSE of 55.7 Mg/ha. This stage provides new insight into the application of deep learning in estimating forest biomass.

In the last stage, Landsat time-series imagery was utilized to enhance the relationship between Landsat spectral reflectance and biomass. An RNN-FNN model integrating the long short-term memory network (LSTM) and the fully connected neuron network (FNN) was proposed to capture time dependencies in Landsat time-series data. The RNN-FNN model was compared to the Random Forest model and linear regression model implemented with single-date predictors. The results indicate that the RNN-FNN model significantly outperformed the Random Forest model and linear regression model. The RNN-FNN model yielded an R^2 of 0.63 and RMSE of 25.5 Mg/ha with 10-year time-series data (2004-2013). At last, the RNN-FNN model was used to generate a map of biomass density for the study area, which demonstrated the practical value of the proposed model.

The proposed framework that bridges inventory data, airborne LiDAR data, and Landsat imagery provides an effective way for forest managers to estimate and understand the spatial distribution of aboveground biomass in the Brazilian Amazon forests. In addition, this research illustrates the value of deep learning in estimating forest biomass and provides practical guidance for future studies on biomass estimations with deep learning.

Table of Contents

Table of Contents iv
List of Figures vi
Chapter 1 Introduction 1
1.1 Research Background and Motivations 1
1.2 Existing Methods Used for Mapping Forest Aboveground Biomass and Their Limitations 2
1.3 Objective and Research Questions 5
1.4 Thesis Structure 6
Chapter 2 Estimating Forest Aboveground Biomass in the Brazilian Amazon Using Airborne LiDAR and Ground Inventory Data 8
2.1 Introduction 9
2.2 Study Area and Data Processing 11
2.3 Methods 15
2.4 Results 18
2.5 Discussion 27
2.6 Conclusions 28
Chapter 3 Mapping Forest Aboveground Biomass in the Brazilian Amazon Using Airborne LiDAR, Landsat Imagery, and Deep Neural Network 29
3.1 Introduction 30
3.2 Study Area and Data 37
3.3 Methods 40
3.4 Results 46
3.5 Discussion 50
3.6 Conclusions 53
Chapter 4 Mapping Forest Aboveground Biomass in the Brazilian Amazon using Airborne LiDAR, Landsat time-series Imagery, and Recurrent Neural Network 54
4.1 Introduction 55
4.2 Study Area and Data 57
4.3 Methods 60
4.4 Results 63
4.5 Discussion 67
4.6 Conclusions 69
Chapter 5 Conclusion 70
5.1 Main Findings 70
5.2 Future Research Opportunities 72
REFERENCE 74

List of Tables

Table 2.1 Summery of inventory sites 11
Table 2.2 LiDAR metrics related to height distribution and vertical structural complexity of all returns . 15
Table 2.3 Summary of performances of three regression models 21
Table 2.4 Analysis of variance of the Pseudo R2, RMSE, %RMSE, and Bias according to three regression models with 1000 bootstrap realizations 25
Table 2.5 Summary of Tukey's Test 25
Table 2.6 Summary of performances of three regression models with 1000 bootstrap realizations 26
Table 3.1 Summary of studies on estimating forest biomass in literature 31
Table 3.2 Summary of existing regression studies with deep learning 34
Table 3.3 Summary of predictors 39
Table 3.4 Two schemes of predictors 46
Table 3.5 Architecture and hyperparameters of the proposed DNN model 46
Table 3.6 Comparison of DNN model performance with different activation functions 47
Table 3.7 Comparison of DNN model performance with different optimization algorithms 47
Table 3.8 Comparison of DNN model performance and training time with different values of epoch and batch size 48
Table 3.9 Comparison of DNN model performance with different weight initialization 49
Table 3.10 Comparison of DNN, RF, SVR, and linear regression model with two schemes 49
Table 3.11 Comparison of DNN model performances with different structures 52
Table 4.1 WRS-2 Path/Row and acquisition date of three scenes Landsat 7 ETM+ imagery covering airborne LiDAR inventory sites 60
Table 4.2 Coefficients for the Tasselled Cap Functions for Landsat ETM+ 60
Table 4.3 Architecture and hyperparameters of the proposed RNN-FNN model 65
Table 4.4 RNN-FNN model performance with different time-series lengths 65
Table 4.5 Performance comparison of RNN-FNN model, linear regression model, and RF 66

List of Figures

Figure 2.1 Location of inventory sites in the Brazilian Amazon 13
Figure 2.2 Box plot of Field AGBD at field inventory sites 19
Figure 2.3 Variable selection by RF........ 20
Figure 2.4 Comparison of OLSR (A), WLSR (B) and NLR (C) for AGBD predictions. The dashed lines are 1:1 line........ 22
Figure 2.5 Box plot of the residuals for three models at field inventory sites 23
Figure 2.6 Box plot of the residuals for three models at different AGBD levels........ 24
Figure 2.7 Cumulative probabilities of AGBD obtained from the field inventory and three regression models 26
Figure 2.8 Summary statistics for three regression models with 1000 bootstrap realizations 27
Figure 3.1 Location of study area (A); False color Landsat imagery of forested areas in the study area (B); LiDAR data overlaid on Landsat scene of the study area (C)........ 38
Figure 3.2 Structure of a fully connected feedforward neural network (A); structure of a neuron (B) 41
Figure 3.3 Plot of loss values 48
Figure 3.4 Map of AGBD generated by DNN model for the study area 50
Figure 4.1 Location of study area (A); False color Landsat imagery of forested areas in the study area (B); LiDAR data overlaid on Landsat scene of the study area (C)........ 58
Figure 4.2 Architecture of the proposed RNN-FNN model........ 61
Figure 4.3 Structure of the LSTM cell (Modified and adopted from Reddy et al. (2018)) 61
Figure 4.4 Structure of input 3D tensor of LSTM with 3 time steps and 10 time steps 63
Figure 4.5 Average vegetation Index dynamics over the 10-year time-series (2004-2013) in TAL site (A), FNA site (B), and JAM site (C) 64
Figure 4.6 Map of AGBD generated by the RNN-FNN model for the study area 67

Chapter 1 Introduction

1.1 Research Background and Motivations

Greenhouse gas (GHG) increases are mainly responsible for climate change over the past 1000 years (Crowley, 2000). Terrestrial ecosystems impact GHG concentration in both carbon emission and sequestration. Studies indicate that terrestrial ecosystems annually release 10-20% of the total global CO_2 to the atmosphere and sequester about 30% (Harris et al., 2012; Houghton et al., 2017; Friedlingstein et al., 2019; Xu et al., 2021). Forests significantly affect the carbon fluxes as a result of management (e.g., afforestation) and disturbances caused by direct and indirect human influences (e.g., deforestation, wood harvesting, fires, and droughts). Therefore, both IPCC reports and Paris Agreement indicate that climate change mitigation goals cannot be achieved without the inclusion of forests (IPCC, 2014; IPCC, 2019; UNFCCC, 2015). A recent study found that global forests were a net carbon sink of -7.6 ± 49 $GtCO_2eyr^{-1}$from 2001 to 2019 (Harris et al., 2021), but the gross emission in tropical forests was still as high as the energy-related carbon that the United States emitted in 2019 (Harris et al., 2021; U.S. Energy Information Administration, 2020).

Amazon basin contains more than 50% of the world’s remaining tropical forests (Fritz et al., 2003). Therefore, the Amazon forest plays a critical role in the global carbon cycle and the achievement of climate change mitigation goals. However, the value and spatial distribution of carbon stock in Amazon forests remain uncertain (Brown et al., 1992; Fearnside, 1997; Malhi et al., 2006; Saatchi et al., 2007; FAO, 2010; Tejada et al., 2020). Houghton et al. (2001) compared seven estimates of carbon stock in Amazon forests. The results indicate large differences in their values varying from a high of 93 ± 23 PgC (Malhi et al., 2006) to a low of 38.9 PgC (Olson et al., 1983). At the same time, their spatial distributions showed little agreement as well (only 5% area agreement of the Brazilian Amazon) (Saatchi et al., 2007; Houghton et al., 2001; Tejada et al., 2019).

The spatial distribution of tropical forest biomass is important in understanding the carbon cycle for two reasons. First, spatially explicit estimates of biomass can reduce the uncertainty in estimates of carbon emission from disturbances over large areas (Baccini et al., 2012). Houghton et al. (2000) indicated that more than 60% of the uncertainty in their estimates of annual forest carbon flux from the Brazilian Amazon resulted from uncertain estimates of forest biomass. The Brazilian Amazon forests have 56% carbon stored in biomass (Pan et al., 2011) and biomass can be the potential carbon emission when disturbances occur (e.g., deforestation, degradation, and fires). Disturbances may occur in forest areas with biomass that are significantly different from the average biomass, so linking specific locations of disturbed areas would decrease certain uncertainty compared to using average biomass in calculations of carbon emission. Second, spatial distribution can help detect and measure the spatial changes of carbon stock, such as changes in forest areas and changes in land cover types. The importance of the spatial distribution of biomass has been recognized by researchers and several attempts have been made to generate biomass maps for the Brazilian Amazon (Avitabile et al., 2016; Nogueira et al., 2015; Mitchard et al., 2014; Baccini et al., 2012; Saatchi et al., 2011; Nogueira et al., 2008; Saatchi et al., 2007).

However, existing biomass maps for the Brazilian Amazon forests are limited in capacity to capture fine-scale biomass variations due to their coarse spatial resolutions. Deforestation and degradation in the Brazilian Amazon have changed significantly from large-scale patterns to fine-scale patterns since the early 2000s. Tyukavina et al. (2017) reported that non-stand-replacement disturbances (e.g., fires and selective logging) exceeded human clearing of forest in the area by 2013 (53% versus 47%). An average of 21% of aboveground carbon loss was from selective logging (Putz et al., 2012) and an average of 30% was from fire (Alencar et al., 2006). However, the spatial resolutions of existing biomass maps range from 1000 m to 500 m (Saatchi et al., 2007; Nogueira et al., 2008; Saatchi et al., 2011; Baccini et al., 2012; Mitchard et al., 2014; Nogueira et al., 2015; Avitabile et al., 2016), which have limited sensitivity to fine-scale variations in forest structure. Therefore, a fine-scale biomass map across large areas of the Brazilian Amazon is needed to better understand the global carbon cycle and mitigate climate change.

1.2 Existing Methods Used for Mapping Forest Aboveground Biomass and Their Limitations

The existing methods used for mapping spatial distribution of forest aboveground biomass can be classified into three classes. The first class includes biogeochemical models (e.g., Olson et al., 1983; Potter et al, 1999). The implementation of biogeochemical models often requires a large number of vegetation input variables (e.g., leaf area index, canopy height, and the fraction of absorbed photosynthetically active radiation) to simulate ecological processes (e.g., photosynthesis, C allocation, and respiration) (Asner and Ollinger, 2009). For example, the Century model and PnET-CN model require more than 30 input variables to simulate the growth and mortality of plants, the subsequent accumulation, and turnover of soil organic matter (SOM) (Parton et al., 1988; Aber et al., 1997). The second class is to apply GIS-based interpolations or extrapolations to estimate biomass (e.g., Brown et al., 1992; Fearnside et al., 1997; Houghton et al., 2000). This method heavily relies on a sufficient number of field measurements and other environmental factors, such as rainfall, tree species, and elevation. Additionally, a clear understanding of the indirect relationships between forest biomass and environmental factors is required, which sometimes is challenging. The two classes of biomass mapping methods rely on the volume and variety of field measurements, which are time-consuming, labor-intensive, and difficult to collect especially in tropical forests.

The last class generates biomass maps using remote sensing data. Remote sensing provides a promising way to overcome the obstacle of the requirement of large volume field measurements with several advantages, such as low cost, continuous data collection, and availability in inaccessible areas. Several biomass maps have been generated using remote sensing data (e.g., Saatchi et al., 2007; DeFries et al., 2000; Chen et al., 2015; de Almeida et al., 2019; Jiang et al., 2020). For example, Saatchi et al. (2011) generated a pantropical biomass map with the resolution of 1 km based on forest inventory data, large footprint LiDAR data from Geoscience Laser Altimeter System (GLAS), and Moderate Resolution Imaging Spectroradiometer (MODIS). Baccini et al. (2012) generated a pantropical biomass map with a resolution of 500 m based on forest inventory data, GLAS, and MODIS.

Although remote sensing-based methods are practical and feasible for mapping and estimating biomass over a large area, some studies show that the insensitivity or saturation of sensor signals significantly limits the application of optical and radar data on estimating biomass in forests with moderate to high biomass levels (Waring et al., 1995; Carlson et al., 1997; Turner et al., 1999).

Hyde et al. (2006) reported that passive multispectral and hyperspectral sensors are of limited use especially in dense forests. Steininger (2000) found that Landsat TM signals saturate when the aboveground biomass approaches 150 MgC/ha or the forest age reaches over 15 years in the successional secondary forests in Manaus, Brazil. Toan et al. (2004) indicated that the saturations of AirSAR and E-SAR signals occur around 30, 50, and 150–200 MgC/ha at C, L, and P bands in temperate, boreal, and tropical forests. The Brazilian Amazon consists of dense tropical forests. The average value of biomass estimations in the Amazon basin is 177 MgC/ha (Houghton et al., 2001). As a result, the applications of satellite optical imagery and radar are limited due to the high level of biomass in the Brazilian Amazon forests.

Light detection and ranging (LiDAR) is a promising approach to mitigate the saturation problem suffered by optical imagery and radar. LiDAR systems can keep sensitive at a high level of biomass with an ability to penetrate the canopy through small leaf gaps for detecting horizontal and vertical vegetation structure simultaneously (Lefsky et al., 2002). LiDAR does not saturate even at 1300 MgC/ha (Means et al., 1999). Therefore, LiDAR can be used as an extensive sampling tool to provide supplemental ground information especially in areas where adequate inventory plots are not available (Nelson et al., 2012; Gobakken et al., 2012). Although the availability of airborne LiDAR data is rapidly increasing, collecting wall-to-wall LiDAR data over large areas is still challenging due to its high acquisition cost (Pflugmacher et al., 2012).

The cost-free Landsat imagery provides wall-to-wall coverage over large areas (White et al., 2016; Brosofske et al., 2014; Cohen et al., 2004). The combination of airborne LiDAR and Landsat has been a research topic of great interest to generate wall-to-wall forest aboveground biomass maps even at regions with high-level biomass. In addition, integrating vertical structure information derived from 3D LiDAR data and horizontally continuous spectral reflectance derived from 2D Landsat imagery has the potential to improve the accuracy in mapping forest aboveground biomass. Ediriweera et al. (2014) explored the use of LiDAR and Landsat data to map forest biomass and found that models incorporating both remote sensing sources performed better than using either alone.

Due to the high level of biomass and heterogeneity of tropical forests, the previous studies with conventional machine learning models and parametric regression models have lower estimation accuracies in tropical forests compared to boreal and temperate forests (e.g., Bourgoin et al., 2018; Santos et al., 2019; Kashongwe et al., 2020). The success of deep learning in a variety of computer vision tasks brings a new insight into improving the accuracy of forest biomass estimations. Although the use of deep learning on estimating tropical forest biomass is very limited, its potential on solving other complex and challenging prediction problems has been demonstrated by several studies. For example, Khaki et al. (2020) proposed a deep learning framework to forecast corn and soybean yield across the Corn Belt in the United States. The proposed model outperformed other conventional machine learning models. Ercanl (2020) designed a deep neural network model to predict tree height. The model achieved the RMSE of 0.694 m. Training a deep learning model requires a huge number of samples, which may be the major obstacle to utilizing deep learning techniques in biomass estimation. The airborne LiDAR can be used as sampling tools to significantly increase the number of sample data for deep learning models.

To further improve the accuracy of biomass estimation in tropical forests, the ready availability of Landsat time-series imagery offers additional help. Landsat time-series imagery in a consistent, long temporal coverage format has led to the new application of forest disturbance and recovery history in forest management (e.g., Huang et al., 2010; Frazier et al., 2014; Zald et al., 2016; Nguyen et al., 2020). By quantifying disturbance and recovery dynamics, Landsat change metrics can improve the estimation accuracy and partially mitigate Landsat saturation in tropical forests (Lu, 2006; Zald et al., 2016). In contrast to the single-date image, the temporal trajectory method can capture abrupt spectral changes (e.g., harvesting and fires) and show the regrowth process in forested pixels. The method allows for trend analysis of forest biomass with disturbances and recovery history (Deo et al., 2016). Although previous studies have demonstrated that temporal trajectory methods can aid in forest aboveground biomass modeling (e.g., Powell et al., 2010; Pflugmacher et al. 2012, 2014; Zald et al., 2016; Matasic et al., 2018; Nguyen et al., 2019), few studies utilize temporal data for estimating biomass in tropical forests. Therefore, the performance of modeling with disturbance and recovery history derived from Landsat time-series imagery in the Brazilian Amazon forests should be further explored.

1.3 Objective and Research Questions

The overarching goal of this research is to propose a deep learning framework for mapping forest aboveground biomass in the Brazilian Amazon with field inventory data, airborne LiDAR data, and Landsat imagery. The framework consists of two stages. At the first stage, the relationship between airborne LiDAR metrics and aboveground biomass is determined by multiplicative power models. At the second stage, wall-to-wall aboveground biomass maps are generated by deep learning with metrics derived from Landsat and Landsat time-series imagery. This research provides new insight into estimating and mapping biomass in tropical forests with state-of-art deep learning models.

Three key research questions are explored in this research:

Question 1: *Which is the best fitting approach to estimate model parameters for multiplicative power models used to explore the relationship between airborne LiDAR metrics and aboveground biomass?*

This question aims to contrast different fitting approaches and find the best one to develop a multiplicative power model. The multiplicative power model would be used to calculate biomass for each LiDAR transect in the subsequent chapters.

Question 2: *Can the deep learning techniques improve the accuracy of aboveground biomass estimation in tropical forests with airborne LiDAR and Landsat 8 imagery?*

This question aims to determine the most accurate model for upscaling the biomass from LiDAR transects to wall-to-wall Landsat imagery.

Question 3: *How can the forest disturbance and recovery history derived from Landsat time-series data improve the accuracy of biomass estimation with state-of-art deep learning?*

This question aims to further improve the estimation accuracy of biomass with the disturbance and regrowth history in the Brazilian Amazon forests.

1.4 Thesis Structure

The thesis consists of five chapters. These chapters build upon each other, but they can be read independently. The subsequent chapters are organized as follows.

Chapter 2 explores the relationship between airborne LiDAR metrics and aboveground biomass and compares the different fitting approaches for multiplicative power models.

Chapter 3 develops a deep feedforward fully connected neural network (DNN) model to estimate aboveground biomass with airborne LiDAR and Landsat 8 imagery.

Chapter 4 proposes a recurrent neural network - fully connected neural network (RNN-FNN) to estimate forest aboveground biomass with disturbance and regrowth history derived from Landsat time-series imagery.

Chapter 5 summarizes the main research findings and discusses future research opportunities.

Chapter 2 Estimating Forest Aboveground Biomass in the Brazilian Amazon Using Airborne LiDAR and Ground Inventory Data

Abstract

Light detection and ranging (LiDAR) systems provide an effective way to quantify forest biomass. Many studies demonstrated the strong relationship between aboveground biomass and height metrics derived from small-footprint airborne LiDAR. Multiplicative power models were commonly used to represent the relationship between biomass and LiDAR metrics. There are two approaches to fit the models. The first one is to directly estimate the parameters without log-transformation. The other one is to fit the linear model on a log-transformed scale using the ordinary least-squares and then back-transform the final model form. However, the differences between the two fitting approaches for the biomass-LiDAR metrics model are not systematically evaluated in literature. In this study, the performances of three multiplicative power models fitted with nonlinear least-square (NLR), ordinary least-square (OLSR), and weighted least-square (WLSR) approaches were compared by ANOVA and Tukey's Test. The ANOVA results indicate significant differences among the three models (OLSR, WLSR, and NLR) in both fitting and prediction phases with 1000 bootstrap realizations in terms of the R^2_{pseudo}, RMSE, %RMSE, and Bias. Furthermore, the results of Tukey's Test indicate that significant differences existed between the NLR and OLSR or WLSR at 99% confidence level. More extreme predictions were generated by NLR compared to OLSR and WLSR. NLR had a worse prediction performance. In contrast, OLSR and WLSR were more accurate in prediction. In conclusion, fitting the biomass-LiDAR multiplicative power models needs careful cautions of selecting fitting approaches.

2.1 Introduction

Quantifying the aboveground biomass of Amazonian forests is extremely important for understanding the global carbon cycle (Fearnside, 1997). Remote sensing techniques have been widely used for estimating aboveground biomass (e.g., Kashongwe et al., 2020; Zhang et al., 2019; Silveira et al., 2019b; Silveira et al., 2019a; Santos et al., 2019; Bourgoin et al., 2018; Babcock et al., 2018; Wang et al., 2018; Matesci et al., 2018; Phua et al., 2017; Jiménez et al., 2017; Garcia et al., 2017; Zald et al., 2016; Cortés et al., 2014). Field measurements are needed to further improve the accuracy of the remote sensing-based estimations. However, extensive field measurements of forest structure are very difficult and expensive to obtain in Amazonian forests (d'Oliveira et al., 2012). Light detection and ranging (LiDAR) systems provide an ability to penetrate the canopy through small leaf gaps for detecting horizontal and vertical vegetation structure simultaneously (Lefsky et al., 2002). The basic measurement made by a LiDAR system is the distance between the sensor and a target surface, obtained by determining the elapsed time between the emission of a short duration laser pulse and the arrival of the reflection of that pulse (the return signal) at the sensor's receiver. The distances derived from LiDAR, combined with the position of the sensor and the direction of the laser beam, uniquely determine 3D coordinates of the objects illuminated (Lefsky et al., 2002, Chen, 2013). LiDAR can generate reliable tree height measurements across all stand conditions (Jurjević et al., 2020). Therefore, LiDAR can significantly reduce the need for intense forest inventory measurements.

Many studies demonstrated the strong relationship between aboveground biomass and height metrics derived from small-footprint airborne LiDAR in tropical, temperate, and boreal forests (Drake et al., 2002a, 2002b; Naesset et al., 2004; Hennaway et al., 2008, Dubayah et al., 2010, Beets et al., 2011b). However, there are no generalized models and predictor sets applicable across a range of forest conditions. Previous studies showed that the best LiDAR height metric used to predict biomass varies from 80th (Patenaude et al., 2004) to 25th (d'Oliveira et al., 2012) percentile heights. Chen (2013) summarized that height metrics can be calculated from either vegetation returns (returns with a certain height, such as 0.5 m, 2 m, or 3 m above the ground surface) or complicated methods (such as an expectation-maximization algorithm). Differences in vegetation structure may explain the variability, however, model forms and variable selection procedures should not be ignored (Chen, 2013). For example, even though Dubayah et al.

(2010), Asner et al., (2012), d'Oliveira et al. (2012), Meyer et al. (2013), and Andersen et al. (2014) all focused on tropical forests, the best LiDAR height metrics differ significantly. Three different model forms are used by these five tropical studies: multivariate linear models (Dubayah et al., 2010; Asner et al., 2012; Andersen et al., 2014); power models (Meyer et al. 2013); univariate linear models (d'Oliveira et al., 2012). In addition, different variable selection procedures were applied as well. Dubayah et al. (2010) used a Bayesian model averaging approach. Meyer et al. (2013) used a relative importance analysis and Akaike information criterion (AIC). d'Oliveira et al. (2012) and Andersen et al. (2014) used the best subset approach. Although these studies have been made to explore the relationship between airborne LiDAR metrics and aboveground biomass, they all focused on small forested areas such as the Amaon basin (e.g., Dubayah et al. 2010: in La Selva; Andersen et al., 2014 and d'Oliveira et al., 2012: in Antimary State Forest, Acre State, Western Brazilian Amazon; Meyer et al., 2013: in Barro Colorado Island). Therefore, a more general understanding of the relationship between airborne LiDAR metrics and aboveground biomass across the entire the Brazilian Amazon is needed.

Multiplicative power models were commonly used to represent the relationship between biomass and LiDAR metrics (e.g., Knapp et al., 2020; Chen et al., 2016; Longo et al., 2016). There are two approaches to fit the models. The first one is to directly estimate the parameters without log-transformation (e.g., Longo et al., 2016; Asner et al., 2014). The other one is to fit the linear model on a log-transformed scale using the ordinary least-squares and then back-transform the final model form (e.g., Wangda et al., 2019; Asner et al., 2012). Mascaro et al. (2011) contrasted the two fitting approaches for biomass allometric equations using harvest data from six tree species. They indicated that directly fitting allometric equations with untransformed variables while assuming additive errors may bias stand-level biomass estimates by up to 100 percent for smaller diameter trees. However, the differences between the two fitting approaches for the biomass-LiDAR metrics model are not explored.

Given the aforementioned research gap, the main goal of this study is to develop a multiplicative power model for estimating forest aboveground biomass in the Brazilian Amazon with the most extensive field measurements and airborne LiDAR. Additionally, we mathematically compared the differences among three multiplicative power models fitted by nonlinear least-square, ordinary least-square, and weighted least-square in estimating biomass with airborne LiDAR metrics.

2.2 Study Area and Data Processing

2.2.1. Study sites and field data

This study covers the Brazilian Amazon region (total 51.46 million hectares). Field inventory data were provided by the US Forest Service and the Brazilian Corporation for Agriculture Research (EMBRAPA) under the Sustainable Landscapes Brazil program. Three sizes of square plots (50*50 m, 40*40 m, and 30*30 m), fixed-sized transects (20*500 m), and DBH-dependent probability sampling transects were used in this field inventory (**Table 2.1**). For square plots with the size of 50*50 m and fixed-size transects, trees with diameter at breast height (DBH) equal to or greater than 35 cm were measured. Trees with DBH equal to or greater than 10 cm were only measured within subplot areas. A correction factor calculated as the ratio of trees with DBH greater than 35 m and trees with DBH greater than 10 cm in a given area was used to correct the uncertainty caused by different sampling strategies of plot and subplot areas. For square plots with the sizes of 40*40 m or 30*30 m, trees with DBH equal to or greater than 10 cm or 5 cm were measured within the plot area. DBH-dependent probability sampling transects used a diameter factor of 10.0 along five 500 m transects including trees with DBH greater than 5 cm. In order to minimize the effect of plot size for calculating aboveground biomass, the fixed-sized transects and DBH-dependent probability sampling transects were divided into segments with an equal size of 20*50 m. Additionally, these segments were apart from each other at least 50 m to avoid autocorrelation for aboveground biomass in tropical forests (Saatchi et al., 2011).

Table 2.1 Summery of inventory sites

State	Municipality	Region	Site	Field inventory date	Plot Size (m*m)	LiDAR inventory date
Pará (PA)	Paragominas	Fazenda Andiroba	AND	2013	50*50	2013
		Fazenda Cauaxi	CAU	2012	20*500	2012
		Paragominas-I	PAR	2013	20*500	2013
	Belterra	Tapajos National Forest	TAP	2009	500 long	2008
	Oriximina	Saraca-Taquera National Forest	FST	2013	50*50	2013
	Tome-Acu		TAC	2014	30*30	2013
	Santarem-III		SAN	2014	50*50	2014

Table 2.1 (Continued) Summery of inventory sites

Acre (AC)	Senador Guiomard	Bonal	BON	2013	50*50	2013
	Porto Acre	Humaita	HUM	2014	50*50	2013
	Rio Branco	Talisma	TAL	2014	50*50	2013
Amazonas (AM)	Adolpho Ducke Forest Reserve		DUC	2011	500 long	2012
Mato Grosso (MT)	Canarana and Querencia	Fazenda Tanguro	TAN	2012	20*500	2012
	Feliz Natal-I		FNA	2013	50*50	2013
	Feliz Natal and Uniao do Sul		FN2	2015	50*50	2016
Rondônia (RO)	Itapoa do Oeste	Jamari National Forest	JAM	2013	50*50	2013

In total, 198 field plots and 207 transect segments were established from 2009 to 2014 across five Brazilian states: Acre (AC), Amazonas (AM), Mato Grosso (MT), Para (PA), and Rondonia (RO) (**Figure 2.1**). The field inventory sites cover different forest statuses, including intact, degradation, deforestation, and secondary growth. DBH was measured at 1.3 m above the ground. Wood density of live trees was obtained from the Global wood density database (Chave et al., 2009; Zanne et al., 2009). When the species of live tree is unknown or not available in the database, the average value of wood density at genus or family level was used. Wood density of standing dead trees was from Keller et al. (2004) and Palace et al. (2007). Individual tree heights were measured using a clinometer and tape as the height to the highest point of the tree crown for most inventory sites. The heights were not available for certain individual trees at two sites in Sao Felix do Xingu Municipality (SFX) and Belterra Municipality (TAP), PA State. The missing tree heights were estimated by the DBH-height relationship following Feldpausch et al. (2012):

$$\mathrm{H} = \mathrm{a}(1 - \exp{(-\mathrm{b}D^{c})}) \qquad 2.1$$

where H is height in m, D is DBH in cm, and a, b, c are model parameters. The models were fitted by tree heights measurements within plots of the TAP site.

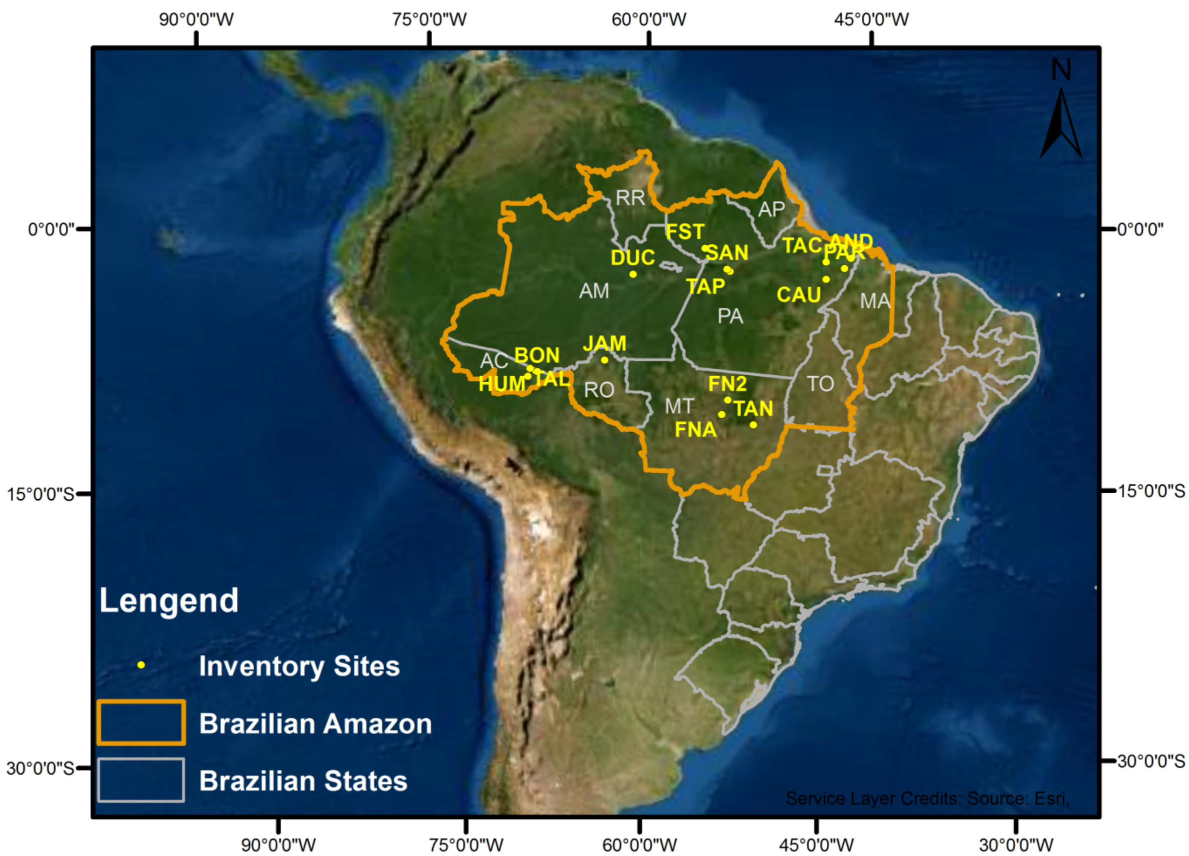

Figure 2.1 Location of inventory sites in the Brazilian Amazon

2.2.2. Field aboveground biomass calculation with allometric models

The aboveground biomass (AGB) of individual trees was estimated using the following allometric models for different vegetation types:

For living trees (Chave et al., 2014):

$$\mathrm{AGB} = 0.0673 \times (\rho D^2 H)^{0.976} \qquad 2.2$$

For standing dead trees (Longo et al., 2016; Chambers et al., 2000):

$$\mathrm{AGB} = 0.1007 \times \rho D^2 H^{0.818} \qquad 2.3$$

For living palm (Long et al., 2016; Goodman et al., 2013):

$$\mathrm{AGB} = 0.03781 \times D^{2.7483} \qquad 2.4$$

For living lianas (Long et al., 2016; Schnitzer et al., 2006):

$$\mathrm{AGB} = 0.3798 \times D^{2.657} \qquad 2.5$$

where ρ is the wood density of living trees or standing dead trees (g/cm^3), D is DBH (cm), and H is tree height (m). The AGB of each tree within inventory plots were summed. The AGB density (AGBD, Mg/ha) for each plot was then calculated by the total AGB of the plot dividing the plot area.

2.2.3. Airborne LiDAR data processing

Airborne LiDAR data were acquired from 2012 to 2015, corresponding to the acquisition dates of field inventories. Airborne LiDAR survey was conducted by Geoid Laser Mapping Ltda. with different sensors, including Optech ALTM 3100 used for 2012, Optech ALTM Orion M-200 used for 2013 and 2014, Optech ALTM Orion-M300 used for 2015. The average flight altitude was 850-900m above ground and the percentage of flightline overlap was around 65%. The average return density is 34 pt/m^2.

The '*lidR*' package (Roussel and Auty, 2019) in R software (R Core Team., 2013) was used to process airborne LiDAR data. The relative height of laser points was calculated as the difference between Z coordinates and the Digital Terrain Model (DTM) generated by the ground return points. A total of 27 LiDAR metrics related to height distribution (e.g., mean, standard deviation, and skewness) and vertical structural complexity (i.e., the Shannon index) of all returns were extracted for each plot and transect segment (**Table 2.2**). The Shannon index was commonly used to descript the species diversity in biological systems (Magurran, 2013). According to the '*lidR*' package, it was used to quantify the diversity and evenness of an elevation distribution of laser points.

Table 2.2 LiDAR metrics related to height distribution and vertical structural complexity of all returns

Lidar Metrics	Description
H_{max}	Maximum return height
H_{mean}	Average return height
H_{sd}	Standard deviation of return heights
H_{skew}	Skewness of return height distribution
H_{kurt}	Kurtosis of return height distribution
$H_{entropy}$	Normalizes Shannon vertical complexity index
H_{5-95th}	Percentiles of return height distribution

2.3 Methods

2.3.1 Airborne LiDAR estimates of aboveground biomass

Variable selections

First, a natural logarithmic transformation was applied on both response variables and predictors selected by the Random Forest (RF) algorithm (Breiman, 2001). RF ranks variables by assessing the impacts of variables on the estimation accuracy. RF was provided by randomForest package (Liaw and Wiener, 2002). The top ten variables selected by RF were used as candidate predictors for the stepwise subset selection. The stepwise subset selections both in forward and in backward modes were then applied to select the most relevant LiDAR metrics, simultaneously considering the Bayesian Information Criterion (BIC) (Schwarz, 1978). The statistically significant variables with the lowest BIC were used to establish the models.

Model establishments

In this study, we evaluated three multiplicative power models fitted by nonlinear least-square, ordinary least-square, and weighted least-square in estimating biomass with airborne LiDAR metrics.

(i) Multiplicative power models fitted by ordinary least-square.

Four steps for the model establishment. First, the multiplicative power models were developed as follows:

$$Y = \beta_0 X_1^{\beta_1} X_2^{\beta_2} \cdots X_n^{\beta_n} e^{\varepsilon} \qquad 2.6$$

Where Y is the AGBD, X_1, X_2, …, X_n are LiDAR-metric variables, and β_0, β_1, β_2, …, β_n are model parameters, and ε is the unexplained error term.

Second, a natural logarithmic transformation was applied on both response variables and predictors (Equation 2.6). The linear model on log-scale was developed as follows:

$$\ln(\mathrm{Y}) = \beta_0 + \beta_1 \ln X_1 + \beta_2 \ln X_2 + \cdots + \beta_n \ln X_n + \varepsilon \qquad 2.7$$

where$Y$is the modeled AGBD, X_1, X_2, …, X_n are LiDAR-metric variables, and β_0, β_1, β_2, …, β_n are model parameters, and ε is the unexplained error term.

Third, the ordinary least-square regression (OLSR) with *lm* function in R software was applied to estimate the parameters of the linear model on log-scale (Equation 2.7), which minimized the sum of squares (SS_{OLSR}):

$$SS_{OLSR} = \sum_{i=1}^{n} \left(\ln(Y_i) - \ln(\widehat{Y_i})\right)^2 \qquad 2.8$$

where n is the number of filed plots, $\ln(Y_i)$ is field-based log-scale AGBD for plot i, and $\ln(\widehat{Y_i})$ is predicted log-scale AGBD for plot i with Equation 2.7.

At last, the final linear models on log-scale fitted by OLSR were then back-transformed to multiplicative power model form. The distribution of $\ln(Y)$ is normal, the distribution of Y is skewed. Therefore, the determining of the antilogarithm of $\ln(Y_i)$ yields the median of the skewed arithmetic distribution rather than the mean (Baskerville., 1972). Therefore, a correction factor (CF) is needed to account for the back-transformation error (Baskerville., 1972; Mascaro et al., 2011; Asner., 2014). The CF is computed as follows:

$$\mathrm{CF} = e^{(MSE/2)} \qquad 2.9$$

where MSE is the mean square error of the linear model on log-scale.

(ii) Multiplicative power models fitted by weighted least-square.

The fitting procedure is similar to the fitting procedure of OLSR but with weighted least-square. The weighted least-square regression (WLSR) was applied to estimate the parameters of the linear model on log-scale (Equation 2.7), minimizing the weighted sum of squares (SS_{WLSR}):

$$SS_{WLSR} = \sum_{i=1}^{n} W_i\left(\ln(Y_i) - \ln(\widehat{Y}_i)\right)^2 \quad 2.10$$

where $W_i$is the weights for plot i. W_i can be generated as a combination of prior knowledge, intuition, and evidence derived from inspection of residuals obtained from unweighted OLSR analysis (Willett and Singer, 1988). In this study, we assigned $W_i$equal to$1/\sigma^2_{iOLSR}$, assuming uncorrelated errors with error variances (Arevalo et al., 2007). σ^2_{iOLSR} is the error variance using OLSR approach.

(iii) Multiplicative power models fitted by nonlinear least-square.

The nonlinear least-square regression (NLR) was directly applied on Equation 2.6b.

$$Y = \beta_0 X_1^{\beta_1} X_2^{\beta_2} \cdots X_n^{\beta_n} + \varepsilon \quad 2.6b$$

The *nls* function of '*stats*' Package in R software was used, which applies a Gauss-Netwton algorithm to minimize the sum of squares (SS_{NLR}):

$$SS_{NLR} = \sum_{i=1}^{n}\left(Y_i - \widehat{Y}_i\right)^2 \quad 2.11$$

where n is the number of filed plots, $Y_i$is field-based AGBD for plot i, and $\widehat{Y}_i$is predicted AGBD for plot i with Equation 2.6b.

Note that the sum of squares SS_{NLR} and SS_{OLSR} given by equation (2.7) and (2.11) are not equivalent and the importance of choosing the proper regression model to estimate the model parameters has been highlighted by Baskerville (1972) and Zar (1968).

2.3.2 Model validation and statistical comparisons

For each multiplicative power model with different fitting techniques (OLSR, WLSR, and NLR), the pseudo coefficient of determination (R^2_{pseudo}), root mean square error (RMSE), relative root mean square error ($\%RMSE$), and Bias were calculated to assess and compare the modeling performance:

$$R^2_{pseudo} = 1 - \frac{\sum_{i=1}^{n}(Y_i - \widehat{Y}_i)^2}{\sum_{i=1}^{n}(Y_i - \bar{Y})^2} \quad 2.12$$

$$\text{RMSE} = \sqrt{\frac{\sum_{i=1}^{n}(Y_i - \widehat{Y_i})^2}{N}} \quad 2.13$$

$$\%RMSE = \frac{RMSE}{\bar{Y}} \quad 2.14$$

$$\text{Bias} = \frac{1}{n}\sum_{i=1}^{n}(Y_i - \widehat{Y_i}) \quad 2.15$$

where $\bar{Y}$ is the mean value of field-based AGBD for all plots, n is the number of samples. In order to further assess the prediction performance of each model, the leave-one-out cross-validation (LOOCV) was used to calculate R^2_{pseudo}, RMSE, %RMSE, and Bias. The reasons that LOOCV is preferred over k-fold cross-validation were studied by Hawkins et al. (2003). LOOCV is almost unbiased since almost all samples are available for model fitting. Repeating k-fold cross-validation can increase the precision of the estimates but still maintaining a small bias (Raschka, 2018).

The one-way analysis of variance (ANOVA) was applied to examine the performance differences among models by analyzing the results in terms of R^2_{pseudo}, RMSE, %RMSE, and Bias based on bootstrapping sampling. Furthermore, a Tukey's test was executed for pairwise comparison to determine whether the differences between each two models were statistically significant.

2.4 Results

In total, 403 inventory plots were used to estimate the aboveground biomass (AGB) with allometrics models. The plot AGB density (AGBD) ranged from 5.5 Mg/ha to 1333.5 Mg/ha across five Brazilian states, with the median value of 195.0 Mg/ha and the mean value of 230.1 Mg/ha. The AGBD variability shows different patterns with different inventory sites (**Figure 2.2**). The variances of AGBD within TAP, CAU sites in PA State and DUC site in AM State are higher than other sites. The existence of large trees significantly contributes to the variations.

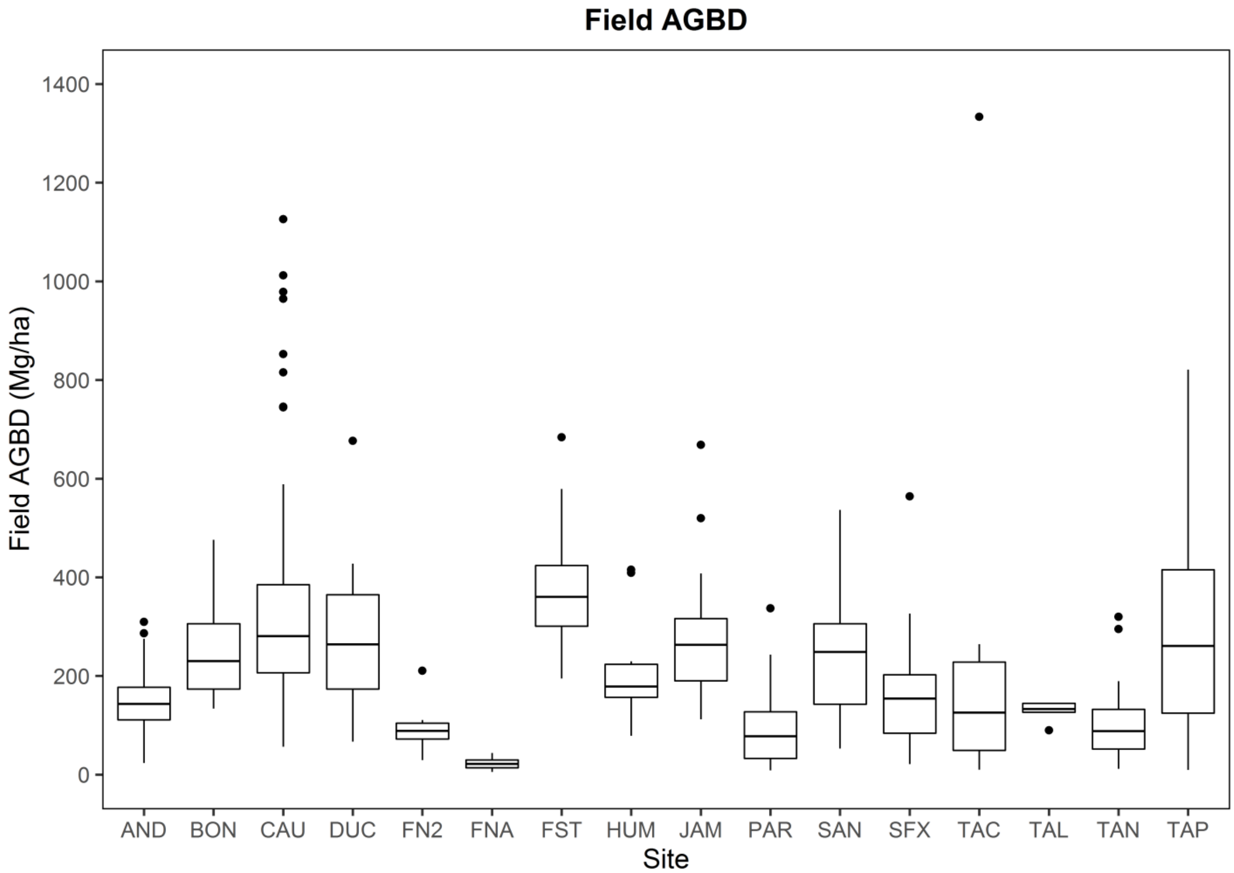

Figure 2.2 Box plot of Field AGBD at field inventory sites

The variables were also ranked based on MSE index (%IncMSE) from RF (**Figure 2.3**). MSE index indicated the percentage increase of MSE by removal of the ranked variables. Ten variables were selected by RF as candidate predictors for the stepwise subset selection, including $\mathrm{H_{65th}}$, $\mathrm{H_{60th}}$, $\mathrm{H_{70th}}$, $\mathrm{H_{90th}}$ $\mathrm{H_{mean}}$, $\mathrm{H_{kurt}}$, $\mathrm{H_{skew}}$, $\mathrm{H_{aboveHmean}}$, $\mathrm{H_{entropy}}$ and $\mathrm{H_{max}}$.

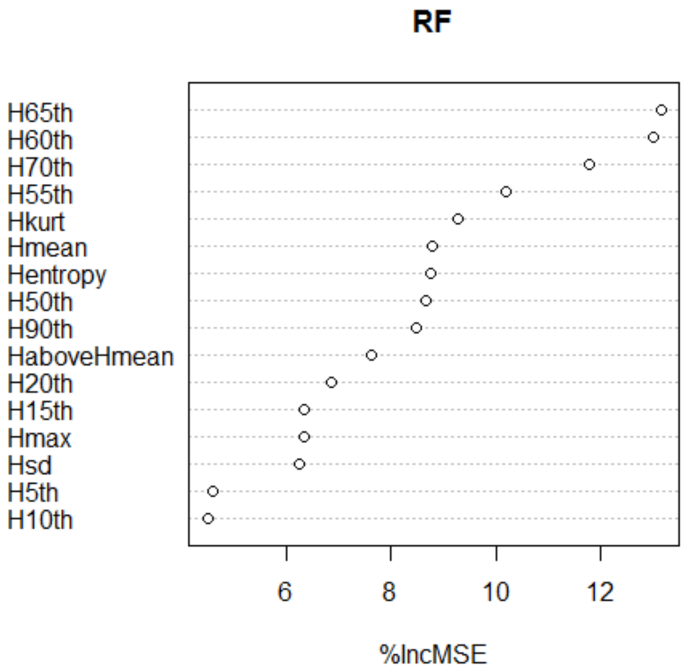

Figure 2.3 Variable selection by RF

The final variables selected by stepwise subset selection, both in forward and in backward modes, are $\mathrm{H_{max}}$, $\mathrm{H_{65th}}$, $\mathrm{H_{90th}}$, and $\mathrm{H_{entropy}}$. The selected four variables suggest that the variance of AGBD was influenced by not only the height distribution but also the vertical structural diversity. The final multiplicative power models using different fitting techniques (OLSR, WLSR, and NLR) with all inventory plots are as follows:

(i) OLSR:

$$\widehat{AGBD}_{OLSR} = 0.52 H_{max}^{-0.75} H_{entropy}^{-1.78} H_{65th}^{1.49} H_{90th}^{0.83} * 1.24 \quad 2.16$$

(ii)WLSR:

$$\widehat{AGBD}_{WLSR} = -0.09 H_{max}^{-0.59} H_{entropy}^{-1.87} H_{65th}^{1.50} H_{90th}^{0.82} * 1.24 \quad 2.17$$

(iii)NLR:

$$\widehat{AGBD}_{NLR} = 0.45 H_{max}^{-0.40} H_{entropy}^{-1.64} H_{65th}^{1.49} H_{90th}^{0.52} \quad 2.18$$

Table 2.3 Summary of performances of three regression models

Models	Re-substitution				Cross-validation			
	R^2_{Pseudo}	RMSE (Mg/ha)	$\%RMSE$	Bias (Mg/ha)	R^2_{Pseudo}	RMSE (Mg/ha)	$\%RMSE$	Bias(Mg/ha)
OLSR	0.42	143.7	62.4%	-13.5	0.41	144.7	62.9%	-13.5
WLSR	0.41	144.9	63.0%	-17.0	0.40	146.4	63.6%	-17.1
NLR	0.43	142.0	62.0%	2.2	0.41	144.6	62.8%	1.6

The three models yielded similar results (**Figure 2.4**). The distributions of residual in CAU, DUC, and TAP inventory sites were more spread due to the higher AGBD variance existing in the three sites (**Figure 2.5**). Otherwise, there was no clear pattern of residuals associating with inventory sites' characteristics. The R^2_{pseudo}, RMSE, %RMSE, and Bias of each model were summarized in **Table 2.3**. NLR performed slightly better than OLSR and WLSR with the lowest Bias and highest R^2_{pseudo}in re-substitution. All of the three models underestimated the AGBD when the value was larger than 400 Mg/ha. In other words, the modeled AGBD in the study area started to saturate at 400 Mg/ha (**Figure 2.6**). A similar saturation level of molded AGBD based on Lidar data was reported by previous studies conducted in the Amazon region (e.g., Longo et al., 2016; de Almeida et al., 2019). Among the three models, the NLR generated larger residuals when AGBD was larger than 200 Mg/ha comparing to the other two models.

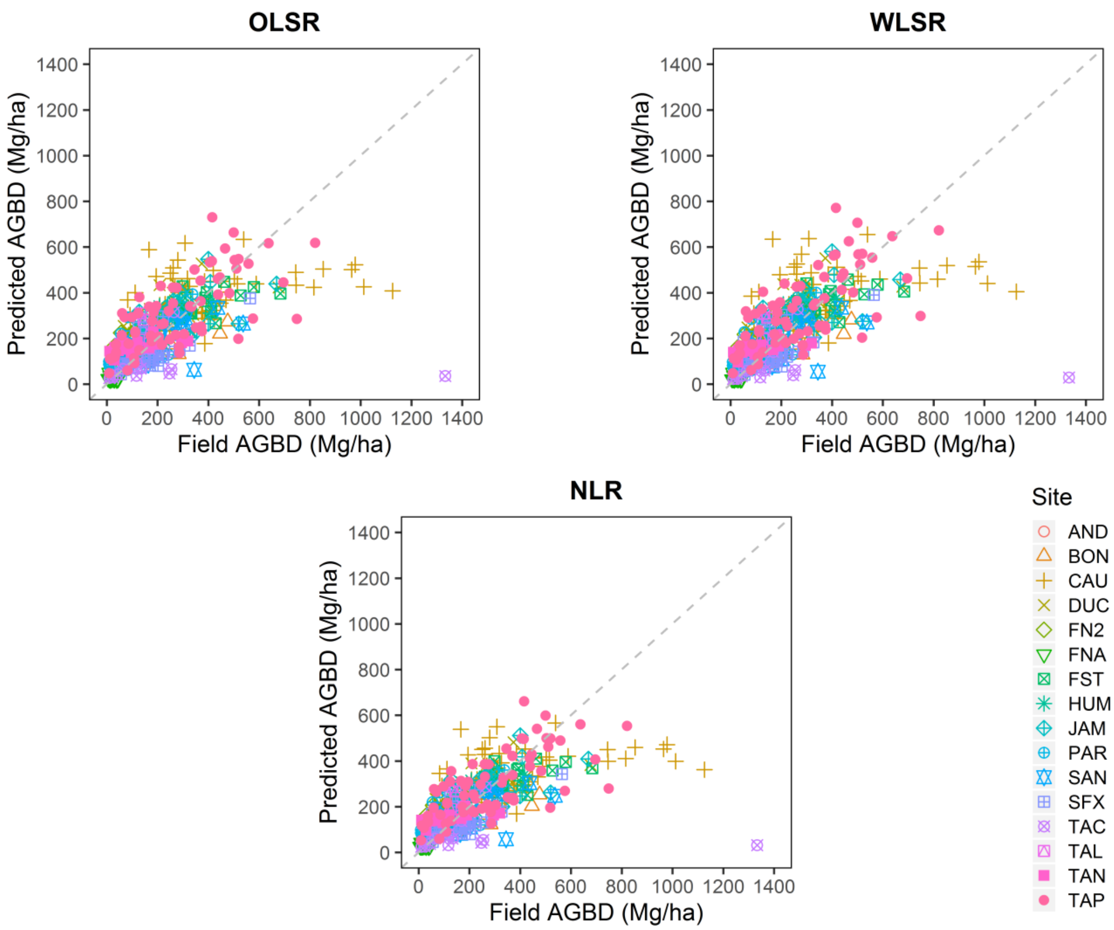

Figure 2.4 Comparison of OLSR (A), WLSR (B) and NLR (C) for AGBD predictions. The dashed lines are 1:1 line

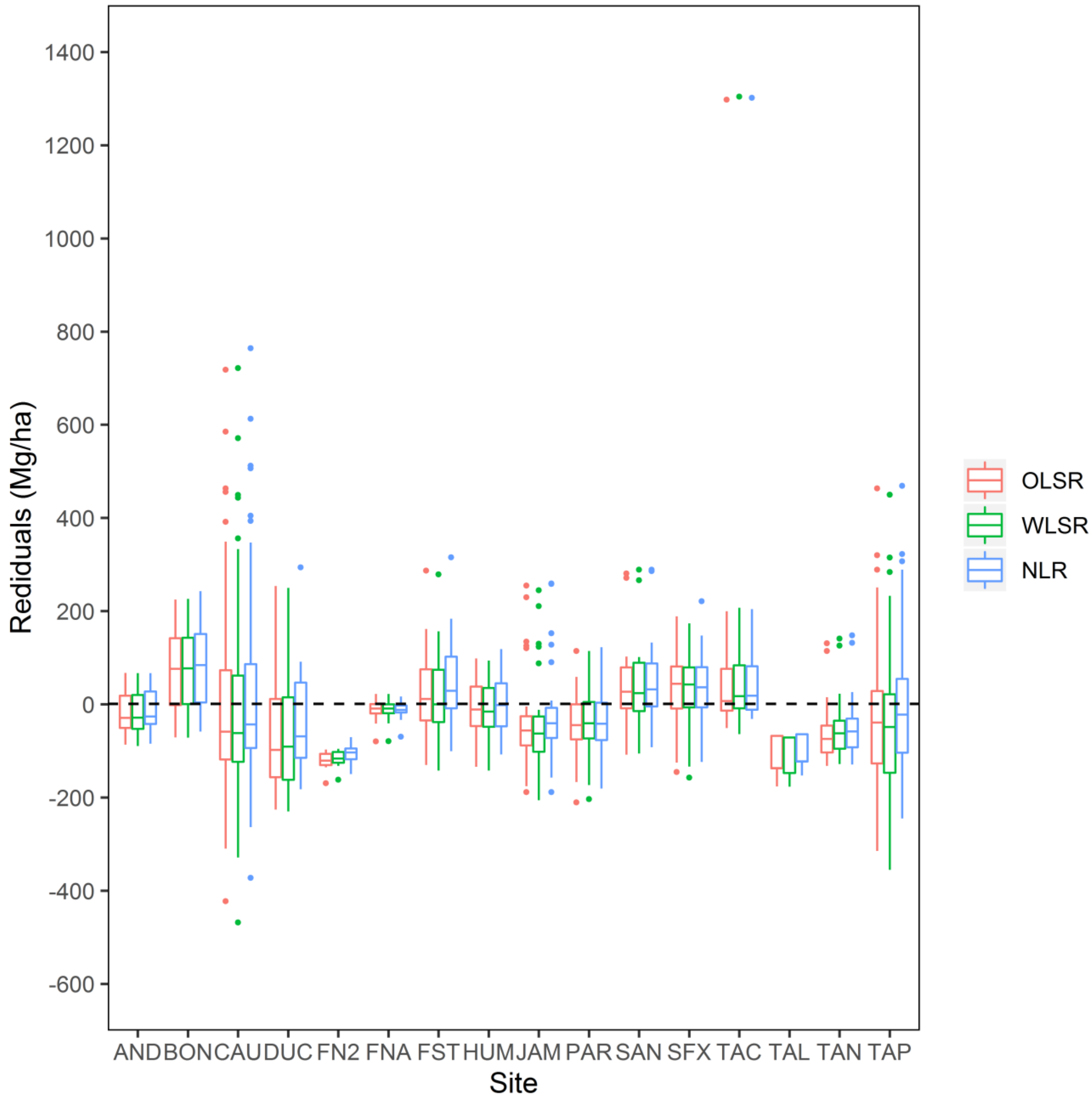

Figure 2.5 Box plot of the residuals for three models at field inventory sites

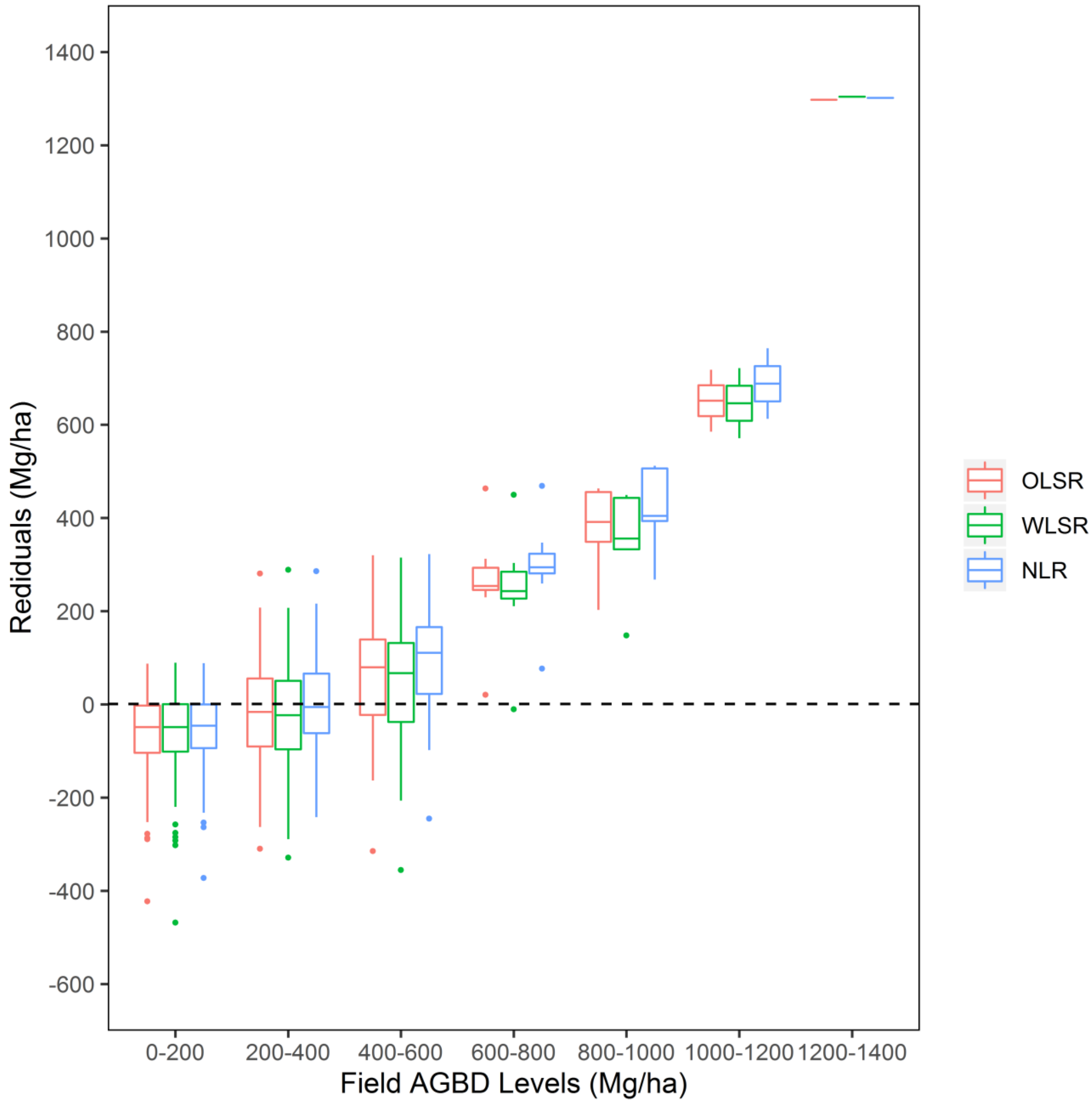

Figure 2.6 Box plot of the residuals for three models at different AGBD levels

The ANOVA results (**Table 2.4**) indicate significant differences among the three models in fitting and prediction phases with 1000 bootstrap realizations in terms of the R^2_{pseudo}, RMSE, %RMSE, and Bias. Furthermore, the results of Tukey's Test (**Table 2.5**) show that significant performance differences existed between NLR and OLSR or WLSR at 99% confidence level according to the R^2_{pseudo}, RMSE, %RMSE. But all three models presented significant differences in terms of Bias. **Figure 2.7** shows the cumulative probabilities of AGBD obtained from the field inventory and regression models. NLR predicted AGBD well when the value is larger than 200 Mg/ha and smaller than 400 Mg/ha. The predicted AGBD values generated by OLSR and WLSR match the values from inventories between 400 Mg/ha and 600 Mg/ha. **Table 2.6** summarizes the performances of the three models with 1000 bootstrap realizations. The fitting performance of NLR is slightly better than OLSR and WLSR. However, the prediction performance of NLR was worse than OLSR and WLSR. **Figure 2.8** demonstrates the distributions of R^2_{pseudo}, RMSE, %RMSE, and Bias. More extremes values were generated by NLR model in cross-validation comparing to OLSR and WLSR, which infers that NLR had a worse prediction performance. On the other hand, OLSR and WLSR were more accurate in prediction.

Table 2.4 Analysis of variance of the Pseudo R2, RMSE, %RMSE, and Bias according to three regression models with 1000 bootstrap realizations

Source	Re-Substitution					Cross-validation				
	Degree of freedom	Sum of squares	Mean square	F value	p-value	Degree of freedom	Sum of squares	Mean square	F value	p-value
Pseudo R^2	2	0.41	0.205	34.94	<0.001	2	51	25.415	8.47	<0.001
RMSE	2	6321	3,160.600	12.02	<0.001	2	113,538	56,769	24.93	<0.001
%RMSE	2	0.12	0.060	15.71	<0.001	2	2.15	1.073	25.46	<0.001
Bias	2	204,000	102,000	12,864	<0.001	2	176,409	88,205	5549	<0.001

Table 2.5 Summary of Tukey's Test

Source	Re-Substitution models			Cross-validation models		
	Groups	Difference	p-value	Groups	Difference	p-value
Pseudo R^2	OLSR-NLR	-0.021	<0.001	OLSR-NLR	0.282	<0.001
	WLSR-NLR	-0.027	<0.001	WLSR-NLR	0.270	0.001
	OLSR- WLSR	-0.006	0.217	OLSR- WLSR	-0.011	0.988
RMSE	OLSR-NLR	2.663	<0.001	OLSR-NLR	-13.696	<0.001
	WLSR-NLR	3.372	<0.001	WLSR-NLR	-12.290	<0.001
	OLSR- WLSR	0.709	0.591	OLSR- WLSR	1.406	0.787
%RMSE	OLSR-NLR	0.012	<0.001	OLSR-NLR	-0.060	<0.001
	WLSR-NLR	0.015	<0.001	WLSR-NLR	-0.053	<0.001
	OLSR- WLSR	0.003	0.508	OLSR- WLSR	0.006	0.784
Bias	OLSR-NLR	-15.513	<0.001	OLSR-NLR	-14.171	<0.001
	WLSR-NLR	-18.959	<0.001	WLSR-NLR	-17.762	<0.001
	OLSR- WLSR	-3.446	<0.001	OLSR- WLSR	-3.591	<0.001

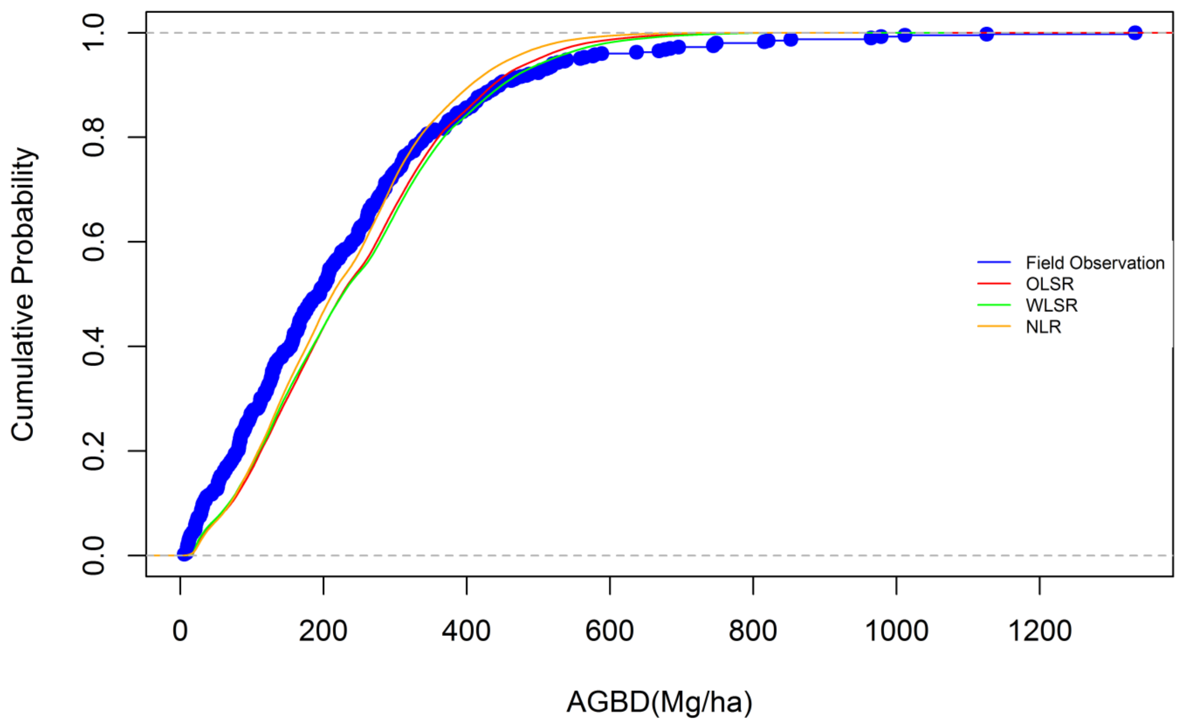

Figure 2.7 Cumulative probabilities of AGBD obtained from the field inventory and three regression models

Table 2.6 Summary of performances of three regression models with 1000 bootstrap realizations

Models	Re-substitution				Cross-validation			
	Mean R^2_{Pseudo}	Mean RMSE (Mg/ha)	Mean $\%RMSE$	Mean Bias (Mg/ha)	Mean R^2_{Pseudo}	Mean RMSE (Mg/ha)	Mean $\%RMSE$	Mean Bias (Mg/ha)
OLSR	0.42	143.1	62.2%	-13.1	0.41	144.6	62.8%	-13.2
WLSR	0.42	143.8	62.5%	-16.6	0.40	146.0	63.4%	-16.8
NLR	0.44	140.4	61.0%	2.4	0.13	158.3	68.8%	1.0

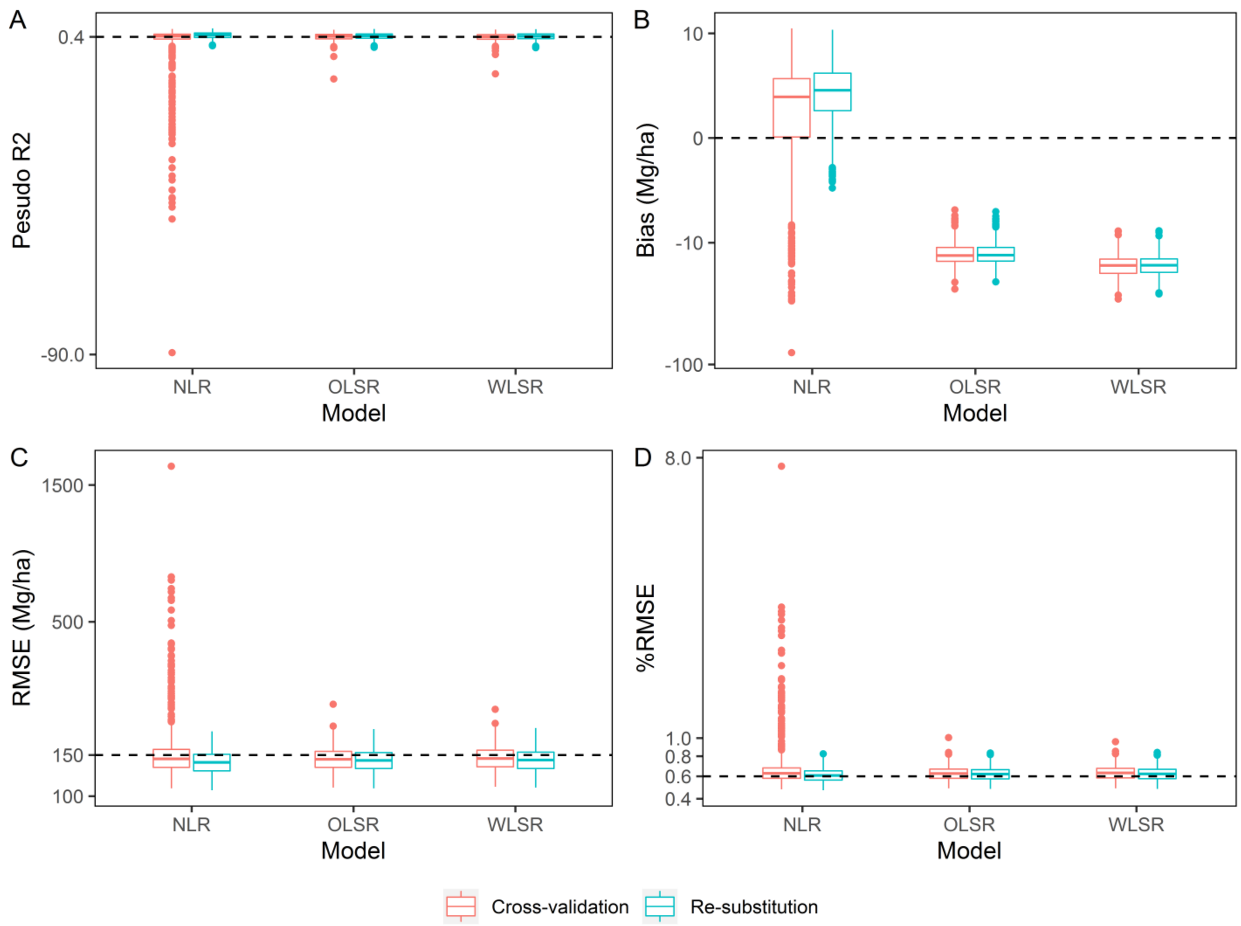

Figure 2.8 Summary statistics for three regression models with 1000 bootstrap realizations

2.5 Discussion

The model accuracy in this study is lower than a similar study conducted in the same study area by Longo et al. (2016). Four reasons may explain the discrepancy: (1) field plots used in the two studies are not identical. Although most of them are similar, we do not have the thirty-two 50*50 m plots in the Belterra region and twenty-nine 40*40 m plots in São Félix do Xingu region. And Longo et al. (2016) did not include 70 TAP plots; (2) the data collected in different years for DUC and JAM sites were used in the two studies; (3) the transect segmentations and tree height estimations in CAU, DUC, PAR, TAN, and TAP sites brought more uncertainties. Although we carefully controlled the segment areas, they may inevitably involve additional errors; (4) we did not exclude the extremely large value of AGBD in TAC site as an outlier. The last reason may be the major cause of the low model accuracy in this study. The extremely large AGBD value is associated with an American oil palm plantation. The unique DBH-H relationship of American oil palm trees results in a very high residual. Chen et al. (2016) indicated that the AGBD of American oil palm needs to be modeled separately from other vegetation types. In this study, modeling American oil palm with other vegetation types can help us compare the fitting and prediction performance of the three models. Additionally, several large AGBD values exist in CAU site due to the absence of large trees in plots. These extreme values contribute to the lower R^2_{Pseudo}, higher RMSE, and Bias of all three models compared to previous studies. The log-transformation applied in OLSR and WLSR mitigates the effect of extremely large values in the model fitting process. The pattern can be observed that the residuals of NLR are consistently larger than the value of OLSR and WLSR when the AGBD value is larger than 200 Mg/ha (Figure 2.6).

2.6 Conclusions

This study developed a multiplicative power model to estimate forest aboveground biomass with 403 inventory plots distributed across five Brazilian states. The final variables selected by stepwise subset selection are H_{max}, H_{65th}, H_{90th}, and $H_{entropy}$. The values of AGBD in the field inventory plots range from 5.5 Mg/ha to 1333.5 Mg/ha with the median value of 195.0 Mg/ha and the mean value of 230.1 Mg/ha. The variances of AGBD within TAP, CAU inventory sites in PA State and DUC inventory site in AM State are higher than other sites. The ANOVA results indicate significant differences among the three multiplicative power models (OLSR, WLSR, and NLR) in both fitting and prediction phases with 1000 bootstrap realizations in terms of the R^2_{pseudo}, RMSE, %RMSE, and Bias. Furthermore, the results of Tukey's Test indicate that significant differences existed between the NLR and OLSR or WLSR at 99% confidence level. More extreme predictions were generated by NLR compared to OLSR and WLSR. NLR had a worse prediction performance. In contrast, OLSR and WLSR were more accurate in prediction. Therefore, fitting the biomass-LiDAR multiplicative power models needs careful cautions of selecting fitting approaches.

Chapter 3 Mapping Forest Aboveground Biomass in the Brazilian Amazon Using Airborne LiDAR, Landsat Imagery, and Deep Neural Network

Abstract

Deforestation and degradation in the Brazilian Amazon forest have changed significantly from large-scale patterns to fine-scale patterns since the early 2000s. However, existing forest biomass maps for this region cannot resolve fine-scale variations in forest structure due to their coarse resolutions (500 m – 1000 m). The availability of Landsat imagery provides the opportunity to estimate forest biomass in a higher spatial resolution. However, the application of Landsat in estimate biomass is significantly limited in tropical forests due to the saturation of sensor signals at moderate to high biomass levels. Airborne LiDAR systems can keep sensitive at a high level of biomass with an ability to penetrate the canopy through small leaf gaps for detecting horizontal and vertical vegetation structure simultaneously. Therefore, airborne LiDAR can be used as an extensive sampling tool to mitigate the saturation with supplemental ground information and increase the number of sample data. In this study, we propose a deep feedforward fully connected neural network (DNN) model to estimate and map aboveground biomass with airborne LiDAR data and Landsat 8 imagery. The results show that the proposed DNN model significantly outperformed the Random Forest model, Support Vector Regression model, and linear regression model with the R^2 of 0.64 and RMSE of 55.7 Mg/ha. An aboveground biomass map was generated by the DNN model for the study area located in the Arch of Deforestation. After comprehensively exploring the effects of DNN's hyperparameters on the model performance, we provide practical guidance for future studies on forest biomass estimation with deep learning.

3.1 Introduction

Tropical forests contain roughly 471 billion metric tons of carbon (Pan et al., 2011). Between 10% and 15% of global carbon dioxide emissions originate from deforestation and degradation in tropical forests (Van der Werf et al., 2009). Roughly 77% - 80% of the forest loss in the Brazilian Amazon has occurred along an arch-shaped region called the "Arch of Deforestation" (Fearnside, 2017; Silva et al., 2021). Deforestation and degradation in this region have changed significantly from large-scale patterns to fine-scale patterns since the early 2000s. Tyukavina et al. (2017) indicated that small-scale clearing is the second-largest disturbance type in Acre, Amazonas, and Rondônia. Non-stand-replacement disturbances (fires and selective logging) exceeded human clearing of forest in areas (53% versus 47%) by 2013. An average of 21% of aboveground carbon loss is from selective logging (Putz et al., 2012) and an average of 30% is from fire (Alencar et al., 2006). Additionally, the Sustainable Palm Oil Production Program launched in 2010 incentivizes oil palm development to a fine-scale pattern. Benami et al. (2017) analyzed the extent and change in oil palm cultivation from 2006 to 2014 and found that 94% of new recently established sites are smaller than 9 ha. However, the existing two forest biomass maps for tropical forests based on Moderate Resolution Imaging Spectroradiometer (MODIS) and Geoscience Laser Altimeter System (GLAS) cannot resolve fine-scale variations in forest structure due to their coarse resolutions (500 m and 1000 m) (Baccini et al., 2012; Saatch et al., 2011).

Compared to using MODIS and GLAS, the combination of Landsat imagery and small-footprint airborne LiDAR can be more effectively capture the forest structure variability at a finer 30 m resolution (Brosofske et al., 2014; White et al., 2016). Deo et al. (2018) evaluated the accuracy of aboveground biomass models based on a range of spatial resolutions of predictors derived from Landsat imagery. The results showed that the accuracy of models decreased with increasing pixel size of the predictors from 30 m to 1000 m. The RMSE increased from 64.38 Mg/ha to 69.89 Mg/ha, and the adjusted R^2 decreased from 0.23 to 0.09. Therefore, the fine resolution provided by the combination of small-footprint airborne LiDAR and Landsat imagery has the potential to improve the estimation accuracy of biomass and generate biomass maps that can represent fine-scale variability.

Conventional machine learning models and parametric regression models have been used to estimate forest biomass with airborne LiDAR and Landsat imagery (Kashongwe et al., 2020; Zhang et al., 2019; Silveira et al., 2019b; Silveira et al., 2019a; Santos et al., 2019; Bourgoin et al., 2018; Babcock et al., 2018; Wang et al., 2018; Matesci et al., 2018; Phua et al., 2017; Jiménez et al., 2017; Garcia et al., 2017; Zald et al., 2016; Cortés et al., 2014). However, the model performance is affected by several factors, including forest type, selected explanatory variables, sample size, and validation procedures (**Table 3.1**). Due to the high level of biomass and heterogeneity of tropical forests, models only with spectral variables performed worse in tropical forests compared to boreal and temperate forests (Table 3.1). Previous studies showed that involving auxiliary data (such as climate, soil, and topographic data) is an effective way to improve the accuracy of biomass estimations in tropical forests (e.g., Silveira et al., 2019). However, the availability of auxiliary data is limited, especially at fine-spatial scales (i.e., 5 - 100 m) for large areas.

Table 3.1 Summary of studies on estimating forest biomass in literature

Region	Mapping Area	Forest Type	Modeling Method	Explanatory Variables	Accuracy	Publication
Canada	~ 552 million ha	Boreal	Random Forest	Surface reflectance; spectral indices; disturbance history; geographic position; topographic variables.	R^2 = 0.515; RMSE = 34.37 Mg/ha	Matesci et al., 2018
Maryland, Unites States	~25,600 km^2	Temperate	Random Forest	Vegetation indices	R^2 = 0.70; RMSE = 35.81 Mg/ha	Wang et al., 2018
Saskatchewan, Canada	~37 million ha	Boreal	Random Forest	Spectral indices; change metrics; topographic variables.	R^2 = 0.50; RMSE = 54.61kg/ha	Zald et al., 2016
Alaska, Unite States	730,000 ha	Boreal	Geostatistical linear model	Surface reflectance; spectral indices; percentage tree cover	R^2 = 0.25-0.55; Square-root transformed CV-RMSE = 1.96 -2.14 $\sqrt{Mg/ha}$	Babcock et al., 2018

Table 3.1 (Continued) Summary of studies on estimating forest biomass in literature

Galicia, Spain	3,600 km^2	Temperate	Linear and exponential regression models	Surface reflectance; spectral indices.	R^2 = 0.60-0.82; RMSE = 5.2 -17.0 Mg/ha	Jiménez et al., 2017
Pantanillos, Chile	400 ha	Temperate	Random Forest	Surface reflectance; spectral indices.	R^2 = 0.77; RMSE = 33.75 Mg/ha	Cortés et al., 2014
California, Unite States	~ 104,000 ha	Temperate	Support Vector	Surface reflectance; spectral indices; Elevation.	R^2 = 0.73-0.79; RMSE = 75.43-87.18 Mg/ha	Garcia et al., 2017
Conghua, China	100 km^2	Temperate	Stacked Sparse Autoencoder network	Surface reflectance; spectral indices.	R^2 = 0.935; RMSE = 15.67 Mg/ha	Zhang et al., 2019
Mai Ndombe province, Congo	~10,000 km^2	Tropical	Random Forest	Surface reflectance	R^2 = 0.11; RMSE = 83.77 Mg/ha	Kashongwe et al., 2020
Sabah, Malaysia	4,924 ha	Tropical	Multiple regression	Surface reflectance; spectral indices; texture metrics.	R^2 = 0.81; RMSE = 112.15 Mg/ha;	Phua et al., 2017
Mato Grosso, Brazil	66,600 km^2	Tropical	Multiple linear regression	Surface reflectance; spectral indices; texture metrics.	R^2 = 0.49; RMSE = 58 Mg/ha	Santos et al., 2019
Minas Gerais state, Brazil	Not reported	Tropical	Random Forest plus residual kriging	Surface reflectance; spectral indices; geographic, topographic and climate data	RMSE = 7.72-57.36 Mg/ha	Silveira et al., 2019b
Minas Gerais state, Brazil	Not reported	Tropical	Random Forest	Surface reflectance; spectral indices; geographic, topographic and climate data	R^2 = 0.86; RMSE = 20.08 Mg/ha	Silveira et al., 2019a
Paragominas municipality, Brazil	19,342 km^2	Tropical	Random Forest	Surface reflectance; spectral indices; texture metrics.	R^2 = 0.28; RMSE = 97.1 Mg/ha	Bourgoin et al., 2018

Developing a model that can take full advantage of spectral information is crucial to efficiently map the biomass of tropical forests over a large area. In recent years, the success of deep learning in a variety of computer vision tasks brings a new insight into forest biomass estimations. Although very limited studies apply deep learning on estimating tropical forest biomass, the potentials of deep learning on solving complex and challenging prediction problems have been demonstrated by previous studies (**Table 3.2).** Lacking training data may be the main obstacle to the application of DNN on biomass estimations. The performance of a deep structure essentially depends on the volume and variety of sample data (Bengio et al., 2013). The deeper structure of DNN allows it to more efficiently represent highly nonlinear functions than shallow networks with one or two hidden layers (Dalto et al., 2015). However, the number of trainable parameters significantly increases when the structure become deeper. Consequently, a larger training dataset is required to train these parameters. Small-footprint airborne LiDAR can be used as a sampling tool to significantly increase the data size (Wulder et al., 2012a), which can be further used as training and test data for the implementation of DNN.

Besides, the selection of hyperparameter values, such as base architecture, kernel initialization, activation function, learning rate, and optimization method, also significantly affects the accuracies of DNN models (Bengio, 2009). However, there is very limited guidance and theoretical solutions for deep structure design and hyperparameter tuning (Lathuilière et al., 2020; Ithapu et al., 2017). Only the effects of learning rate and base architecture are examined in previous studies (Narine et al., 2019; Ercanl, 2020; Astola et al., 2021). Narine et al. (2019) examined the effects of DNN structures and learning rates on the model performances of forest biomass predictions. The results show that a model with 3 hidden layers (with 500, 300, and 60 neurons, respectively) performed best. And learning rates of 0.001 were the optimal option. The model explained 48% of the variance in simulated AGB with RMSE of 20.29 Mg/ha. Ercanl (2020) designed a DNN model to predict tree height-diameter relationships. The author tested the number of hidden layers ranged from 3 to 10 and the number of neurons in each hidden layers ranged from 10 to 100. The experimental results indicate that the model with 8 hidden layers and 100 neurons in each hidden layer had the best performance. Astola et al. (2021) examined the effects of DNN's depth and width on predicting forest structural variables. They found that the DNN with two hidden layers (with 67and 24 neurons, separately) was the best model in terms of RMSE% and BIAS%. Besides the depth and width of DNN and learning rates, the effects of other hypterparameters on the model accuracy have not been explored yet.

Table 3.2 Summary of existing regression studies with deep learning

Study	Study Objective	Forest Type	Deep Learning Model	Number of Hidden Layer	Number of Neurons in Each Hidden Layer	Other Hyperparameters	Accuracy	Datasets
Shao et al., (2017)	Predicting forest aboveground biomass	Tropical forest	Stacked Sparse Autoencoder network (SSAE)	N/A	N/A	N/A	R^2 = 0.589-0.812; RMSE = 21.753-30.453 Mg/ha	Filed inventory, airborne LiDAR, Landsat, and Sentinel-1A.
Wang et al., (2018)	Predicting crop yields	N/A	Recurrent neural network (RNN)	1 LSTM layer; 1 fully connected layers	N/A	N/A	R^2 = -1.75-0.66; RMSE = 0.26-0.52 bushels/acre	Field inventory, MODIS.
Ayrey et al., (2019)	Predicting forest attributes (total biomass, basal area, mean tree height, volume et al.)	Boreal forest	Convolutional neural network (CNN)	Based on Inception-V3	N/A	N/A	RMSE for biomass is 36 Mg/ha	Field inventory, airborne LiDAR, Sentinel-2, Landsat, and MODIS
Long et al., (2019)	Predicting canopy height	Boreal forest	Convolutional neural network (CNN)	2 convolutional layers	N/A	Learning rate: 0.0001; Optimizer: Adam; Activation function: ReLU; Batch size: 36; Epochs: 500.	MAE = 1.7 m-4.3m	Sentinal-2 and airborne LiDAR.
Narine et al., (2019)	Predicting forest aboveground biomass	Temperate forest	Deep fully connected network (DNN)	3 fully connected layers for no noise scenario; 2 fully connected layers for no noise scenario; 2 fully connected layers for no noise scenario	500-300-60; 300-160; 600-400	Learning rate: 0.008-0.0001; Optimizer: RMSprop; Activation function: ReLU; Batch size: 100; Epochs: 100.	R^2 = 0.64-0.67; RMSE = 15.47-16.09 Mg/ha	Field inventory, ICESat-2, and Landsat.

Table 3.2 (Continued) Summary of existing regression studies with deep learning

Nevavuori et al., (2019)	Predicting crop yields	N/A	Convolutional neural network (CNN)	2 convolutional layers; 2 fully connected layers	N/A	Learning rate: 0.0001; Optimizer: Adadelta; Activation function: ReLU; Batch size: 128; Epochs: 50.	MAE = 484.3-680.4 kg/ha	Field inventory and UAV.
Zhang et al., (2019)	Predicting forest aboveground biomass	Temperate forest	Stacked Sparse Autoencoder network (SSAE)	N/A	N/A	N/A	R^2 = 0.935; RMSE = 15.67 Mg/ha; rRMSE = 11.407%	Field inventory, airborne LiDAR, and Landsat.
Ercanl, (2020)	Predicting tree height-diameter relationships	Temperate forest	Deep fully connected network (DNN)	8 fully connected layers	100 in each layer	Activation function: Rectifier; Epochs: 1000.	r = 0.984; RMSE = 0.694 m	Field inventory.
Khaki et al., (2020)	Predicting crop yields	N/A	Combine convolutional neural networks and recurrent neural network (CNN-RNN)	4 convolutional layers; 1 LSTM layer.	N/A	Learning rate: 0.0003 with Adam; Optimizer: Adam and SGD; Activation function: ReLU; Batch size: 25; Epochs: 350000.	RMSE = 15.74-16.48 bushels/acre	Field inventory.
Hawrylo et al., (2020)	Predicting growing stock volume	Temperate forest	Deep fully connected network (DNN)	2 fully connected layers	70-70	Optimizer: rmsprop; Activation function: LeakyReLU.	R^2 = 0.13-0.46; RMSE = 103.23 - 72.61 m^3/ha; rRMSE = 20.99% - 37.11%	Field inventory, airborne LiDAR, and Landsat.
Wolanin, (2020)	Predicting crop yields	N/A	Convolutional neural network (CNN)	2 convolutional layers	N/A	Learning rate: 0.01-0.0001; Optimizer: Adam; Activation function: ReLU; Batch size: 100; Epochs: 100.	NSE = 0.868	Field inventory, MODIS, and meteorological data.

Table 3.2 (Continued) Summary of existing regression studies with deep learning

Shah et al., (2020)	Predicting canopy height	Temperate forest	Convolutional neural network (CNN)	4 convolutional layers; 1 fully connected layers	N/A	Activation function: ReLU (convolutional layer), Linear (fully connected layer); Epochs: 2000.	MAE = 3.092m	Landsat and airborne LiDAR.
Astola et al., (2021)	Predicting forest structural variables (stem volume, basal area, stem diameter, and tree height)	Boreal forest	Deep fully connected network (DNN)	2 fully connected layers	67-24	Learning rate: 0.0001; Optimizer: Adam; Activation function: ReLU; Batch size: 100; Epochs: 250.	R^2 = 0.65-0.71; rRMSE = 28.2%-42.4%	Field inventory, Sentinel-2, and airborne LiDAR.
Khaki et al., (2020)	Predicting crop yields	N/A	Combine convolutional neural network (CNN) and fully connected network (DNN)	7 convolutional layers; 2 fully connected layers	100-50	Learning rate: 0.0005; Optimizer: Adam; Activation function: ReLU; Batch size: 32; Epochs: 4000.	Corn: MAE = 12.71-18.24 bushels/acre Soybean: MAE = 3.66-6.05 bushels/acre	Field inventory, MODIS.
Liu et al., (2021)	Predicting forest structural parameters (stem diameter, tree height, stem volume, and stem density)	Temperate forest	Combine deep full connected network (DNN) and radial basis neural network (RBN)	5 fully connected layers 1 RBN layer	100-80-60-40-20	Learning rate: 0.001; Optimizer: Adam; Activation function: ReLU; Batch size: 100; Epochs: 100.	R^2 = 0.67-0.86; rRMSE = 6.95%-20.34%	Field inventory, airborne LiDAR.
Ogana and Ercanl, (2021)	Predicting tree height-diameter relationships	Tropical forest	Deep fully connected network (DNN)	6-7 fully connected layers	100 in each layer	Activation function: Rectifier; Epochs: 1000.	RMSE = 1.939 – 3.887 m	Field inventory.

Given the aforementioned research gaps, this study developed a deep feedforward fully connected neural network regression model (DNN) to estimate and map aboveground biomass in the Arch of Deforestation with airborne LiDAR and Landsat 8 imagery. Specifically, we make the following contributions: (1) we comprehensively investigated the effects of hyperparameter values selection on the DNN model performances with a large size of sample data; (2) we compared the model accuracies of DNN model, linear regression model, and two conventional machine learning methods, i.e., Random Forest (RF), Support Vector Regression (SVR); (3) we examined the importance of spectral bands and vegetation indices derived from Landsat 8 imagery in estimating aboveground biomass; (4) we generated an accurate aboveground biomass map for the study area located in the Arch of Deforestation.

3.2 Study Area and Data

3.2.1 Study area

The study area is located in the Arc of Deforestation, Brazil (**Figure 3.1A**). This region corresponds to one Landsat scene (WRS-2 Path/Row 232/066). GlobeLand30 was applied to understand the land cover and land use in the study area, which is a 30-meter resolution global land cover data product developed by China (Jun et al., 2014). GlobeLand30 can be downloaded from the National Geomatics Center of China (http://www.ngcc.cn/ngcc/html/1/396/400/16121.html). According to the land cover map, eight land cover classes exist in the study area including Cultivated land, Forest, Grassland, Shrub land, Wetland, Water bodies, Artificial surfaces, and Bare land. The Forest class is defined as the land covered with trees and vegetation cover over 30%. Accordingly, the areas classified as Forest were extracted for further analysis (**Figure 3.1B**).

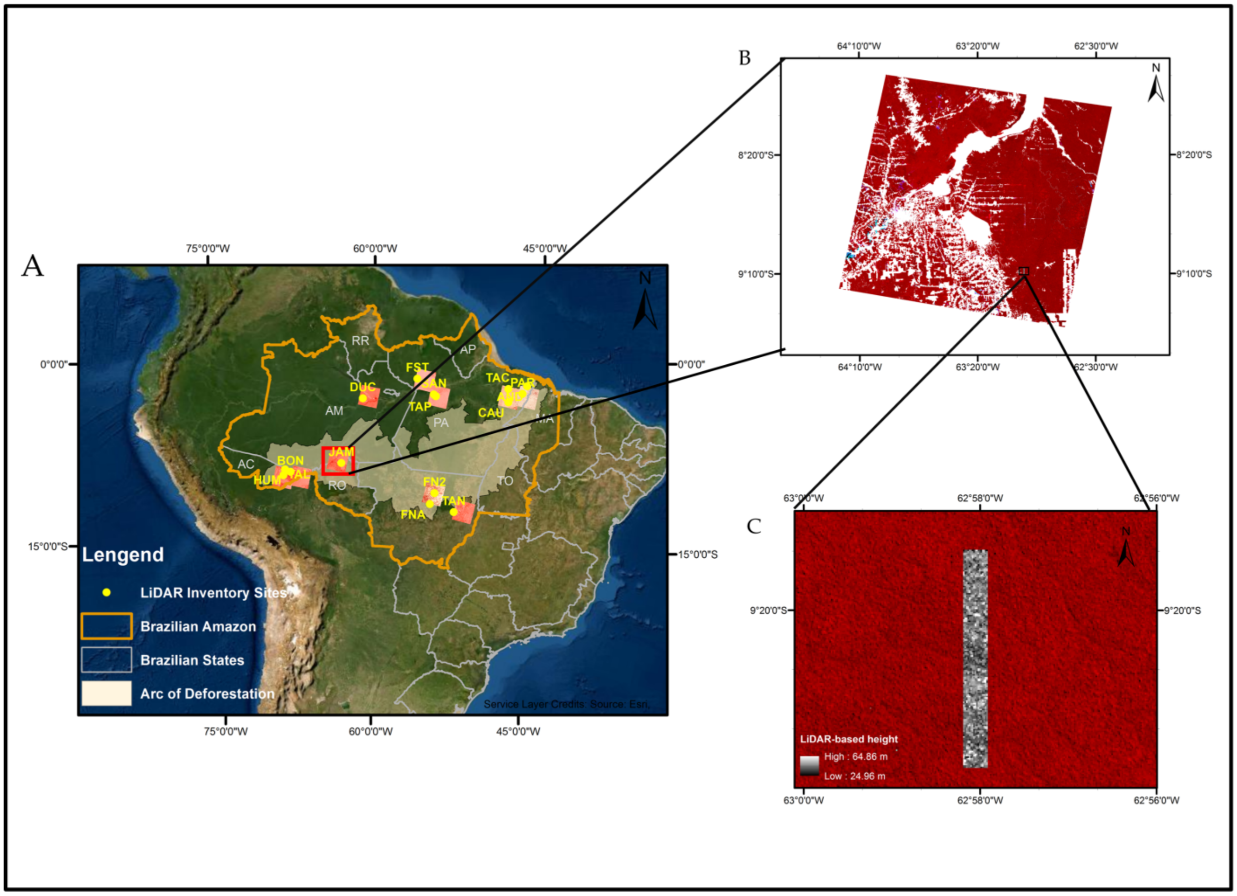

Figure 3.1 Location of study area (A); False color Landsat imagery of forested areas in the study area (B); LiDAR data overlaid on Landsat scene of the study area (C)

3.2.2 Lidar data-based aboveground biomass calculations

In total, twenty airborne LiDAR transects are available across the Brazilian Amazon (Figure 3.1A). The airborne LiDAR data were acquired in 2012 - 2015 by Geoid Laser Mapping Ltda with the ALTM 3100 and Optech ALTM Orion M-200 sensor. The average flight altitude was 850-900 m above ground and the percentage of flightline overlap was around 65%. The average return density is 34 pt/m2. The '*lidR*' package (Roussel and Auty, 2019) in R software (R Core Team., 2013) was used to extract LiDAR metrics. According to Equation 3.1 developed in Chapter 2, the LiDAR-based aboveground biomass density (AGBD) was generated in a 30*30 m grid corresponding to the spatial resolution of Landsat imagery. The LiDAR-based AGBD was used to calibrate and validate the DNN model.

$$\widehat{AGBD} = 0.52H_{max}^{-0.75}H_{entropy}^{-1.78}H_{65th}^{1.49}H_{90th}^{0.83} * 1.24 \quad (3.1)$$

3.2.3 Landsat 8 imagery acquisition and predictor generation

Surface reflectance imagery derived from Landsat 8 Collection 2 Level 1 Operational Land Imager (OLI) data is available on the United States Geological Survey for Earth Observation and Science. The surface reflectance products were generated with specialized software called Land Surface Reflectance Code (LaSRC) (Vermote et al., 2016). LaSRC applied atmospheric correction routines to the standard data product of the Landsat sensors with help of auxiliary data such as water vapor, ozone, and Aerosol Optical Thickness (AOT) retrieved from MODIS. Additionally, the bidirectional effect associated with the geometric relationships between the Sun and sensor angles was reduced by LaSRC (Otto et al., 2020). In total, thirteen Landsat-8 surface reflectance images acquired from 2013 to 2016 were downloaded, corresponding to the acquisition dates of field inventories and airborne LiDAR data.

Vegetation indices and Tasseled Cap components derived from spectral bands were widely used to estimate forest aboveground biomass, but their importance in explaining biomass variations varies with vegetation types and modeling methods (Gómez et al., 2014; Silveira et al., 2019). Therefore, their importance was evaluated in this study. We involved 7 surface reflectance bands (SR), 4 commonly used vegetation indices, and 3 Tasseled Cap components as predictor variables (**Table 3.3**).

Table 3.3 Summary of predictors

Predictors Abbreviation	Name	Details/Formula	Reference
B1	SR Band 1	Coastal aerosol, 0.43-0.45 µm	
B2	SR Band 2	Blue, 0.45-0.51 µm	
B3	SR Band 3	Green, 0.53-0.59 µm	
B4	SR Band 4	Red, 0.64-0.67 µm	
B5	SR Band 5	Near Infrared, 0.85-0.88 µm	
B6	SR Band 6	Shortwave infrared 1, 1.57-1.65 µm	
B7	SR Band 7	Shortwave infrared 2, 2.11-2.29 µm	
NDVI	Normalized Difference Vegetation Index	$\frac{NIR - RED}{NIR + RED}$	Tucker, 1979
EVI	Enhanced Vegetation Index	$2.5 * \frac{NIR - RED}{NIR + 6 * RED - 7.5 * Blue + 1}$	Huete et al., 2002
EVI 2	Enhanced Vegetation Index 2	$2.4 * \frac{NIR - RED}{NIR + RED + 1}$	Jiang et al., 2008

Table 3.3 (Continued) Summary of predictors

NIRv	Near-infrared reflectance of vegetation	$NIR * NDVI$	Badgley et al., 2017
TCB	Tasseled Cap Brightness	$0.3037\ Blue + 0.2793\ Green + 0.4743\ Red + 0.5585\ NIR + 0.5082\ SWIR1 + 0.1863\ SWIR2$	Kauth and Thomas, 1976
TCG	Tasseled Cap Greenness	$(-0.2848)\ Blue - 0.2435\ Green - 0.5436\ Red + 0.7243\ NIR + 0.0840\ SWIR1 - 0.1800\ SWIR2$	Kauth and Thomas, 1976
TCW	Tasseled Cap Wetness	$0.1509\ Blue + 0.1973\ Green + 0.3279\ Red + 0.3406\ NIR - 0.7112\ SWIR1 - 0.4572\ SWIR2$	Kauth and Thomas, 1976

3.3 Methods

3.3.1 Deep neural network

In this study, the effects of structure design and hyperparameter values selection on the DNN model performances were comprehensively evaluated with massive amounts of sample data. The predictor variables (Landsat SR bands, vegetation indices, and Tasseled Cap components, as discussed in Section 3.2.2) were fed into a DNN to generate numerical AGBD outputs. The trainable parameters were optimized in the process of learning, which can be used to predict AGBD across the entire study area. The DNN in this study was built on Keras with TensorFlow backend in Python. The free Google Colaboratory 12GB GPU was used to train the DNN.

Base architecture

The DNN implemented in this study is a fully connected feedforward neural network, which consists of an input layer, multiple hidden layers, and an output layer. The hidden layers contain multiple neurons, and the neurons between layers are fully connected (**Figure 3.2A**). In this study, the number of hidden layers and neurons in each layer is determined by trial and error. Inspired by the suggestions for shallow structures provided by Doukim et al. (2010) and Huang (2003), deeper structures with the combinations of the number of 1, 2, 4, 8, 16, 32, 64, and 128 neurons and the number of 6, 8, 10, 12, 14, and 16 hidden layers were tested to identify the optimal structure.

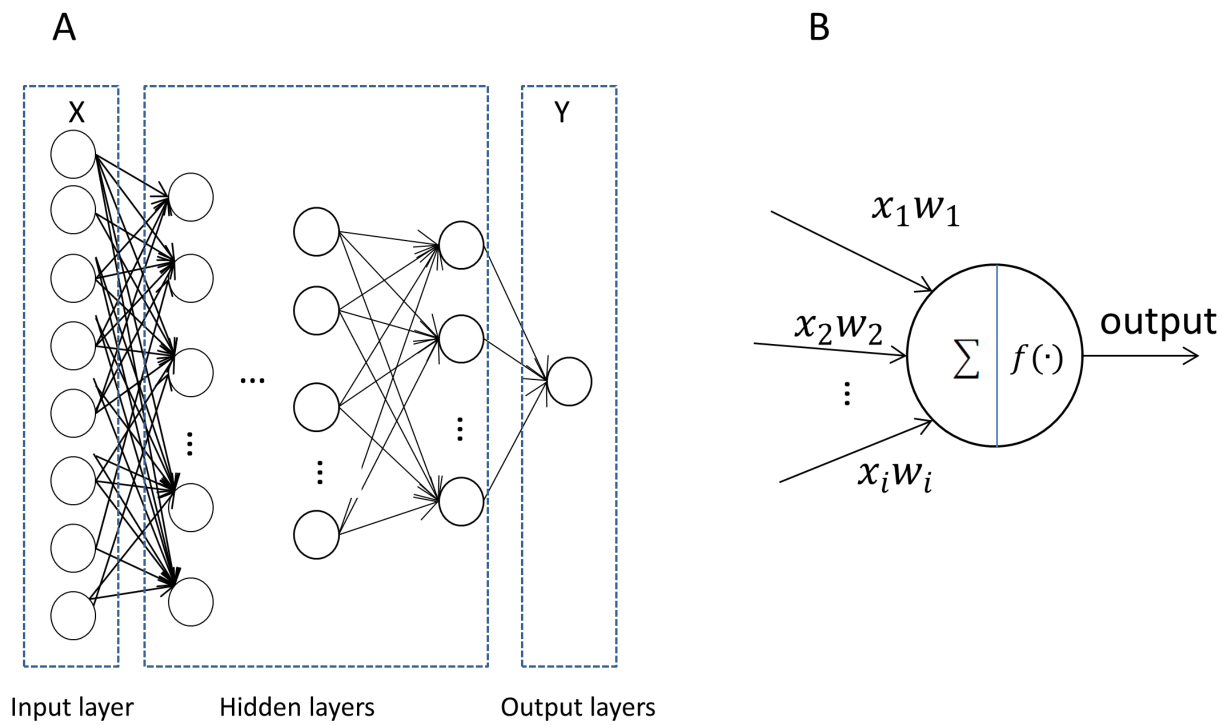

Figure 3.2 Structure of a fully connected feedforward neural network (A); structure of a neuron (B)

The output of *i*th neuron (**Figure 3.2B**) in the *l*th layer can be mathematically represented as follows:

$$y_i^l = f(\sum_{j=1}^{n} w_{ij} x_j^{l-1} + b_i^l) \quad 3.2$$

where $f(\cdot)$ is the activation function. w_{ij} and b_i^l are the weight and bias respectively. x_j^{l-1} is the output of jth neuron from $l-1$ layer, $j = 1,2 \ldots . n$.

Activation function

Activation function *f(.)* determines the output value of each neuron as demonstrated in Equation 1, which adds non-linearity to the output so that the neural network can solve nonlinear problems. Many efficient activation functions are proposed and applied to solve complex learning tasks (e.g., Szegedy et al., 2013; Mourgias-Alexandris et al., 2019; Ide and Kurita, 2017). Given the regression problem in this study, six unbounded activation functions are explored.

Rectified Linear Unit (ReLU) is the most widely used activation function of neural networks (Nair and Hinton, 2010). It overcomes the vanishing gradient problem, allowing neural networks to train faster and perform better. Therefore, ReLU has become the default activation function for many successful deep networks, such as VGG-16 (Simonyan and Zisserman, 2014), Faster R-CNN (Ren et al., 2015). The ReLU function can be written as follows:

$$f(x) = \max(0, x) \tag{3.3}$$

If x is positive, the output value is equal to x. Otherwise, the output value is equal to 0. In other words, only the positive neuron will be activated.

Leaky ReLU is proposed to mitigate the "dying ReLU problem" by allowing a small, non-zero gradient when the x is negative (Maas et al., 2013). The Leaky ReLU function can be demonstrated by,

$$f(x) = \begin{cases} x, \ if\ x > 0; \\ 0.01x, \ else. \end{cases} \tag{3.4}$$

Parametric ReLU (PReLU) generalizes Leaky ReLU to a situation where the slope α is input-specific and trainable (He et al., 2015), instead of 0.01 in the Leaky ReLU function:

$$(x) = \begin{cases} x, \ if\ x > 0; \\ \alpha x, \ else. \end{cases} \tag{3.5}$$

Exponential Linear Unit (ELU) pushes mean unit activations closer to zero, which speeds up learning by bringing the normal gradient closer to the unit natural gradient (Clevert et al., 2015). The ELU function can be written as follows:

$$f(x) = \begin{cases} x, \ if\ x > 0; \\ \alpha(e^x - 1), \ else. \end{cases} \tag{3.6}$$

where α is the predefined parameter and α >= 0.

Scaled Exponential Linear Unit (SELU) introduces an internal normalization technique to avoid the vanishing and exploding gradient problem. It ensures training a deep network with many layers and robust learning (Klambauer et al., 2017). The SELU function can be given by,

$$f(x) = \lambda \begin{cases} x, \ if \ x > 0; \\ \alpha(e^x - 1), \ else. \end{cases} \qquad 3.7$$

where λ and α equal to 1.05070098 and 1.67326324, which follows the suggestions provided by Klambauer et al. (2017).

Swish is a smooth, non-monotonic function, which requires a single scalar input to realize the self-gating. Compared to the non-smooth nature of ReLU, the smoothness of Swish plays a beneficial role in optimization and generalization, reducing the sensitivity to initialization and learning rates (Ramachandran et al., 2017). The Swish function can be demonstrated by,

$$f(x) = x * \frac{1}{1+e^{-\beta x}} \qquad 3.8$$

Optimization

A number of optimization algorithms are proposed to minimize the value of the cost function by adjusting the parameters iteratively. There is no clear conclusion in the literature regarding the best optimization algorithm for DNN regression problems. In this study, the effects of seven popular optimization algorithms on the accuracy of modeling ABGD are explored. The loss function was defined with the mean squared error (MSE).

Stochastic Gradient Descent (SGD) algorithm is an iterative optimization process of the first order. SGD converges fast on large datasets because it employs a single sample at each iteration to avoid data redundancy.

Adagrad is an optimization algorithm with parameter-specific learning rates. It adapts the learning rate to the parameters' update frequency. Adagrad uses a different learning rate for every parameter at every time step (Duchi et al., 2011). Dean et al. (2012) concluded that Adagrad greatly improved the robustness of SGD for training a large-scale distributed deep network.

Adadelta is a more robust extension of Adagrad. Adadelta introduces a new dynamic learning rate using only first-order information. According to Zeiler (2012), Adadelta does not require manual setting of a learning rate and appears robust to large gradients, noise, and architecture choice.

Root Mean Square Propagation (RMSProp) is proposed to overcome Adagrad's drawback of diminishing learning rates by changing the gradient accumulation into an exponentially weighted moving average (Hinton and Tieleman, 2012). Specifically, Adagrad adjusts the learning rate according to the history of the squared gradient, while RMSProp only considers recent gradients for that weight (Lathuilière et al., 2019). Hinton and Tieleman (2012) suggested a good default value for the learning rate is 0.001.

Adaptive Momentum Estimation (Adam) updates the RMSProp by incorporating momentum. Adam implements the exponential moving average of the gradients to scale the learning rate. Adam is computationally efficient and requires little memory. Adam always has a good performance on problems that are large in terms of data/parameters (Kingma and Ba, 2014). Two variants of Adam are also evaluated. They are Adamax (Kingma and Ba, 2014) and Nadam (Dozat, 2016).

Other hyperparameters

Batch size and learning rate

In practice, the optimal choices of batch size and learning rate can significantly reduce training time and improve performance. The overfitting may occur if the learning rate is too small. In contrast, the training will diverge if the learning rate is too large. According to empirical experiences documented in the literature (Smith, 2018), the learning rates tested in this study are 0.01, 0.001, and 0.0001. Given the AGBD regression problem and 12GB GPU memory limitation, the batch sizes of 500, 800, 1000, and 1200 were tested.

Weight and bias initialization

The convergence rate and accuracy of the DNN are affected by the initial choice of weights and bias according to the input data distribution. Improper weight and bias initializations would slow the training speed and increase the generalization error. We explored four efficient weight initializations for the asymmetric activation functions selected for the AGBD regression, including Random Normal Initializer, Truncate Normal Initializer, LeCun Normal Initializer (LeCun et al., 2012), Glorot Normal Initializer, Glorot Uniform Initializer, and He Normal Initializer (He et al., 2015). Additionally, two bias initializations were tested, including Zero Initializer and Constant Initializer.

3.3.2 Linear regression model and conventional machine learning methods

Linear regression and two conventional machine learning methods were used to compare the performance of the proposed DNN. Linear regression model was commonly used to model the relationship between AGBD and predictor variables. Linear regression model is easy to apply and interpret. The model form was shown as follows:

$$\widehat{Y} = \widehat{\beta_0} + \widehat{\beta_1}X_1 + \widehat{\beta_2}X_2 + \cdots + \widehat{\beta_n}X_n \qquad 3.8$$

where $\widehat{Y}$ is the modeled AGBD, $X_1,\ X_2,\ \ldots,\ X_n$are predictor variables, and $\widehat{\beta_0},\ \widehat{\beta_1},\ \widehat{\beta_2},\ \ldots,\ \widehat{\beta_n}$are model parameters. In this study, the ordinary least-square with *lm* function in R software was used to estimate the model parameters.

Two conventional machine learning methods were widely applied in estimating forest biomass in literature. Random Forest (RF) method is an ensemble-learning algorithm consisting of a set of regression trees (Breiman, 2001). Each regression tree uses a different bootstrap sample of input data. Each node of a tree is split by the predictor variables randomly selected from all input variables and the best split is determined with the lowest Gini Index (Breiman, 2001). Due to the advantages of being less sensitive to noise and low risks of overfitting, RF is popular in mapping forest biomass over large areas (e.g., Baccini et al., 2008; Zald et al., 2016; Matesic et al., 2018). Support Vector Regression (SVR) is formulated as an optimization problem by minimizing the convex ξ-insensitive loss function and finding the flattest tube that contains the most training samples (Awad and Khanna, 2015).

3.3.3 Evaluation of models' performance

In order to examine the importance of spectral bands and vegetation indices derived from Landsat 8 imagery in estimating aboveground biomass, we designed two schemes. The first scheme includes spectral bands, vegetation indices, and Tasseled Cap components. The second scheme only contains seven spectral bands (**Table 3.4**). 70% of the samples were used to train the model and 30% of the samples were used to evaluate the model's performance in terms of R^2 and RMSE.

Table 3.4 Two schemes of predictors

Scheme	Predictors
Scheme 1	SR Band 1- 7, NDVI, EVI, EVI2, NIRv, TCB, TCG, TCW
Scheme 2	SR Band 1-7

3.4 Results

A total of 157,200 samples were generated for experiments in this study. Among them, 110,040 samples (70%) were used to train each model, and 47,160 samples (30%) were used to evaluate the results. The optimal base architecture of the DNN consists of 1 input layer, 8 hidden layers, and 1 output layer. The number of neurons (128-128-128-64-64-64-32-32-32) at each hidden layer and trainable parameters in each layer is listed in **Table 3.5**. A total of 54,816 parameters were trained. This base architecture was used for all other experiments.

Table 3.5 Architecture and hyperparameters of the proposed DNN model

Layers	Output Shape	# Trainable Parameters
Fully Connected	(N, 128)	1024
Fully Connected	(N, 128)	16512
Fully Connected	(N, 128)	16512
Fully Connected	(N, 64)	8256
Fully Connected	(N, 64)	4160
Fully Connected	(N, 64)	4160
Fully Connected	(N, 32)	2080
Fully Connected	(N, 32)	1056
Fully Connected	(N, 32)	1056

The activation function played an important role in deep learning techniques. We evaluated six unbounded activation functions with the testing dataset (**Table 3.6**). The results showed that the model with SELU had the best performance, which achieved 0.64 for R^2 and 55.7 Mg/ha for RMSE. In contrast, ELU had the lowest accuracy, which yielded an R^2 of 0.59 and RMSE of 61.7 Mg/ha. We also tested different values of β in Swish, including 0.01, 0.1, 0.5, 1, and

5. However, the value of β did not have a significant effect on the model performance. When 0.1 was chosen for β, the highest R^2 of 0.61 and the lowest RMSE of 58.1 Mg/ha were achieved. When 0.01 was chosen, the lower R^2 of 0.57 and the highest RMSE of 62.9 Mg/ha were yielded.

Table 3.6 Comparison of DNN model performance with different activation functions

Activation Function	R^2	RMSE (Mg/ha)
ELU	0.59	61.7
ReLU	0.59	61.7
Leaky ReLU	0.60	59.2
Swish	0.61	58.1
PReLU	0.62	57.3
SELU	0.64	55.7

The results of the comparison of model performance with different optimizers indicated that optimization algorithms significantly affected the model accuracy (**Table 3.7**). The values of R^2 ranged from -0.04 to 0.64, and the values of RMSE ranged from 102.1 Mg/ha to 55.7 Mg/ha. The model with the Adam optimizer had the highest accuracy and the model with the Adagrad optimizer yielded the lowest accuracy. Therefore, the Adam optimization algorithm was selected as the optimizer to test the effectiveness of batch size and learning rate.

Table 3.7 Comparison of DNN model performance with different optimization algorithms

Optimization Algorithm	R^2	RMSE (Mg/ha)
Adagrad	-0.04	102.1
Adadelta	-0.04	102.1
RMSprop	0.56	63.7
SGD	0.58	62.2
Adam	0.64	55.7

We found that the choice of batch size and epoch only had significant effects on the model training time but not on the model accuracy (**Table 3.8**). The executing time was almost doubled when increasing the epoch number from 1,000 to 2,000, but the accuracies kept similar. Besides, when the batch size was set to 800, the model slightly outperformed others. Accordingly, 1,000 and 800 were chosen for epoch and batch size, respectively. In order to understand the effect of learning rates on the model capacity, we plotted the loss value of each epoch in **Figure 3.3**. Both too large and too small learning rates could not achieve the optimal results. Therefore, the learning rate of 0.001 was chosen for the Adam optimizer.

Table 3.8 Comparison of DNN model performance and training time with different values of epoch and batch size

Epoch	Batch Size	Executing Time	R^2	RMSE (Mg/ha)
1000	500	34m33s	0.61	58.1
	800	14m24s	0.64	55.7
	1,000	12m22s	0.63	56.1
	1,200	10m22s	0.63	56.3
2000	500	45m25s	0.61	58.1
	800	30m25s	0.63	56.1
	1,000	26m15s	0.60	59.2
	1,200	21m12s	0.63	56.1

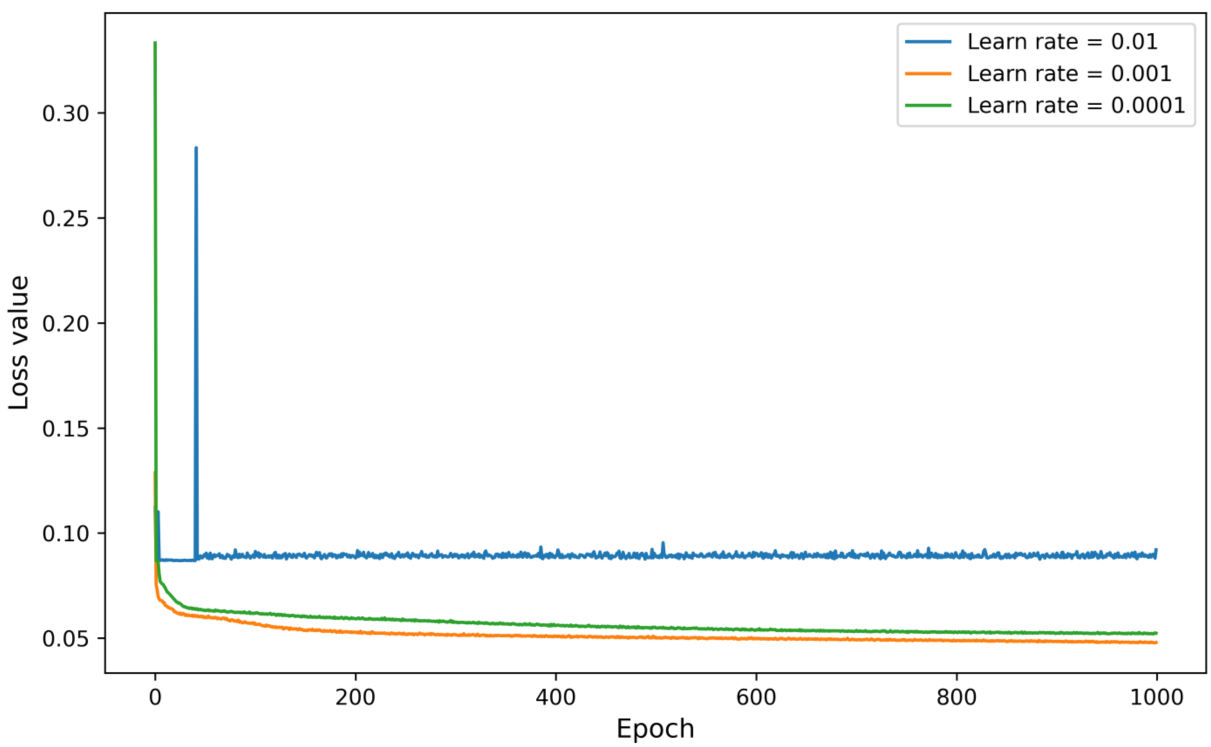

Figure 3.3 Plot of loss values

Weight initializations had a slight influence on the model performance (**Table 3.9**). The model with Truncate Normal weight initialization achieved the highest R^2 and the lowest RMSE.

However, the models with other weight initializations had very similar accuracies. Besides, after testing Zero Initializer and Constant Initializer, we also found that bias initializations had little influence on model accuracies as well.

Table 3.9 Comparison of DNN model performance with different weight initialization

Weight Initialization	R^2	RMSE (Mg/ha)
Random Normal	0.56	63.7
Truncate Normal	0.64	55.7
LeCun Normal	0.61	58.1
He Normal	0.61	58.1
Glorot Normal	0.62	57.3
Glorot Uniform	0.59	61.7

Table 3.10 summarizes the values of R^2 and RMSE of DNN, RF, SVR, and linear regression model. It can be seen that DNN has the best performance. Obviously, SVR and linear regression could not effectively deal with the complex relationship between AGBD and Landsat metrics. It is different from our expectation that including VIs and TC components did not improve the accuracy for all models.

Table 3.10 Comparison of DNN, RF, SVR, and linear regression model with two schemes

	Scheme 1 (7 predictors)		Scheme 2 (14 predictors)	
Regression Model	R^2	RMSE (Mg/ha)	R^2	RMSE (Mg/ha)
DNN	0.64	55.7	0.61	58.4
RF	0.50	65.9	0.50	65.9
SVR	0.03	91.9	0.04	91.6
Linear regression	-0.0002	105.3	-0.0002	105.3

The distribution map of AGBD was generated by the optimal DNN model with 7 SR band predictors for the study area (**Figure 3.4**). The maximum and minimum values of AGBD are 632.1 Mg/ha and 0.8 Mg/ha. The average value is 46.9 Mg/ha. Overall, the higher values are concentrated in the eastern part. Some lower values can be observed along the western side of the Amazon River.

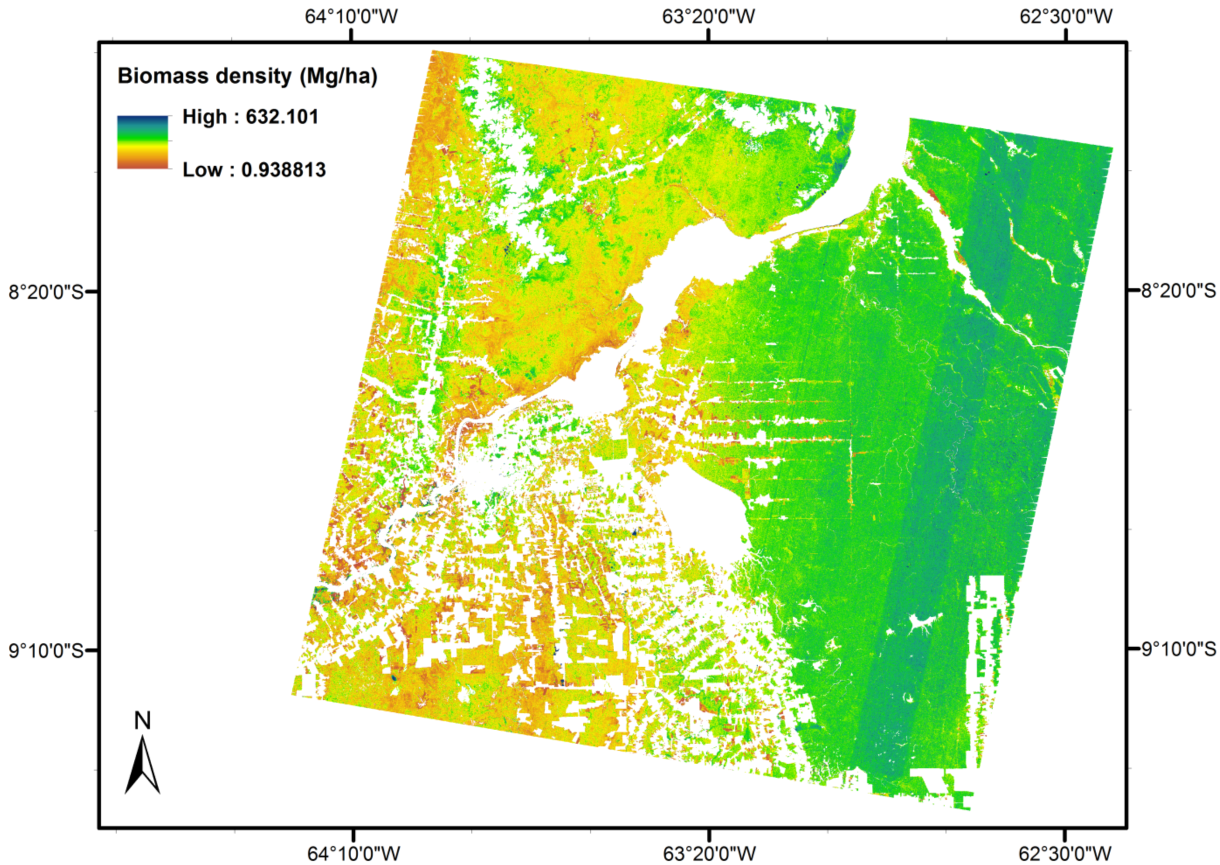

Figure 3.4 Map of AGBD generated by DNN model for the study area

3.5 Discussion

Deep learning techniques bring new opportunities to forest biomass estimation. However, two challenges need to be addressed. First, it is challenging to collect a large amount of sample data to train sophisticated neural networks. Field inventory data is too cost-consuming to be generated. Only 0.001% of the Brazilian Amazon biome area is sampled (Tejada et al., 2019). The development of LiDAR techniques offers a new way to extend the sample size. The Sustainable Landscape Project (SL) is a leading project launching airborne LiDAR surveys over the Amazon biomes. This study takes advantage of the SL project to generate 157,200 sample data from 20 LiDAR transects for training and validating the proposed DNN model. The second challenge is related to tuning hyperparameters of deep neural networks. Few studies focus on the application of deep learning in estimating forest biomass. Therefore, the understanding of hyperparameters' effects on model accuracy is lacking.

The neural network structure is directly related to the number of network parameters. When the neural network becomes deeper and wider, the model capacity increases. At the same time, the model would require more training sample to train increased parameters. Therefore, it is challenging to keep the number of network parameters low and preserve the model predicting ability. Different network structures are used in previous studies. For example, Narine et al. (2019) designed a shallow but wide structure with three hidden layer (500-300-60). Both Ogana and Ercanl (2021) and Ercanl (2020) used a deep and symmetric structure with 6-8 hidden layers (100 neurons in each hidden layer). Astola et al. (2021) found that a shallow and narrow structure with 2 hidden layers (67-24) was efficient. The network structure used in this study is deep and asymmetric with 8 hidden layers (128-128-128-64-64-64-32-32-32). The number of neurons in hidden layers followed a decreasing trend from the first to the last layer, as it in Narine et al. (2019) and Astola et al. (2021). These different network structures were compared in terms of R^2 and RMSE (**Table 3.11**). The model 1 with a deep and asymmetric structure proposed in this study had the highest accuracy and had less trainable parameters compared to deep and symmetric model 2. The model 4 with a shallow and narrow structure had a lower accuracy than the model 3 with a shallow but wide structure due to less trainable parameters. It is worthy to note that the model 3 had the highest number of trainable parameters but it did not have the best prediction performance. The deep and asymmetric structure proposed in this study keeps the balance between the number of network parameters and the model predicting ability.

Table 3.11 Comparison of DNN model performances with different structures

Model	The Number of Hidden Layers	The Number of Neurons in Hidden Layers	Total Trainable Parameters	R^2	RMSE (Mg/ha)
1(proposed in this study)	8	128-128-128-64-64-64-32-32-32	54,816	0.64	55.7
2 (deep and symmetric)	8	100 in each layer	71,500	0.59	61.7
3 (shallow but wide)	3	500-300-60	172,360	0.55	63.0
4 (shallow and narrow)	2	67-24	2,158	0.51	64.8

Vegetation indices (VIs) and Tasseled Cap (TC) components are commonly reported as valuable variables to estimate forest biomass. However, we found that including vegetation indices and TC components cannot improve the model accuracies for DNN, RF, SVR, and linear regression model. Compared to previous studies, this study involves a very large size of sample data (157,200 samples). Sufficient sample data may deliver enough information to determine the relationship between biomass and Landsat spectral bands. Besides, the mathematics behind DNN may contribute as well. A large amount of nonlinear functions exists in hidden layers of DNN. When only SR bands used as predictors, the output of these hidden layers may carry the similar information as VIs and TC components carried. Therefore, involving VIs and TC component cannot provides additional useful information. The final DNN model includes 7 SR band predictors, which is more efficient to map biomass over a large area since no additional calculations of VIs and TC components are needed.

Five sources of uncertainty would be associated with the AGBD map generated in this study: (1) the first source is related to the field inventory sampling design. Specifically, the distribution of inventory plots and LiDAR transects and plot sizes would bring uncertainties to the results; (2) the second source is associated with allometric models, including the errors related to explanatory variables (e.g., species diversity, wood density, and tree height and DBH field measurements) and model parameter estimates; (3) the third source is related to the regression models linking field AGBD with remote sensing metrics; (4) the fourth source is the coregistered error; (5) the last one is related to the temporal differences between the field and remote sensed data. In this study, we only consider the third source of uncertainty. For the first source, the inventory plots and LiDAR transects are relatively evenly distributed over the Brazilian Amazon (Figure 3.1). And Mascaro et al. (2011) found that the influence of differing plot shape on estimate accuracy is very low (1.5 Mg C /ha). For the second and fourth source, we cannot assess them due to the lack of access to destructive AGB datasets and more information related to GPS positional error. We carefully minimized the fifth source by selecting the Landsat imagery to match the acquisition dates of field and LiDAR campaigns.

3.6 Conclusions

This study develops a deep feedforward fully connected neural network (DNN) model to estimate and map aboveground biomass in the Arch of Deforestation with airborne LiDAR and Landsat 8 imagery. The proposed DNN model achieved the R^2 of 0.64 and RMSE of 55.7 Mg/ha, which significantly outperformed the Random Forest model, Support Vector Regression model, and linear regression model. After comprehensively investigating the effects of hyperparameter selection on the DNN model performances with a large size of sample data. We found that the model with SELU had the best performance compared to other activation functions. Besides, optimization algorithms significantly affected the model accuracy. The values of R^2 ranged from -0.04 to 0.64, and the values of RMSE ranged from 102.1 Mg/ha to 55.7 Mg/ha with different optimization algorithms. Additionally, we found that 1000 and 800 are the optimal choices for epoch and batch size respectively. And both too large and too small learning rates cannot achieve optimal results. The learning rate of 0.001 was chosen for the Adam optimizer. Furthermore, the weight and bias initializations had slight influences on the model accuracy. Different from previous studies, we found that including vegetation index and Tasseled Cap components did not improve the model performance. This study provides new insight into the application of deep learning in estimating forest biomass.

Chapter 4 Mapping Forest Aboveground Biomass in the Brazilian Amazon using Airborne LiDAR, Landsat time-series Imagery, and Recurrent Neural Network

Abstract

Due to the high level of biomass and heterogeneity of tropical forests, the previous studies with conventional machine learning models and parametric regression models have lower accuracies in tropical forests compared to boreal and temperate forests. Landsat time-series data provide a promising opportunity to improve the accuracy by enhancing the relationship between Landsat spectral reflectance and forest aboveground biomass with disturbance and recovery dynamics. Compared to the single-date image, Landsat time-series data can capture abrupt spectral changes (e.g., harvesting and fire) and show the regrowth process in forested pixels. However, very limited studies take advantage of Landsat time-series data to estimate aboveground biomass in tropical forests. Recurrent neural networks (RNN) are powerful deep learning techniques to capture time dependencies in sequence data. However, RNN has not been used to estimate forest biomass yet. Therefore, this study is the first attempt to propose an RNN-FNN model for estimating forest biomass with Landsat time-series imagery and airborne LiDAR data. The RNN-FNN model integrates the long short-term memory network (LSTM) and the fully connected neuron network (FNN). We compared the RNN-FNN model with the Random Forest model and linear regression model implemented with single-date predictors. The results indicated that the RNN-FNN model significantly outperformed the Random Forest model and linear regression model with the R^2 of 0.63 and RMSE of 25.5 Mg/ha. This study demonstrates the value of RNN and Landsat time-series imagery in estimating forest biomass.

4.1 Introduction

The deforestation rate in the Brazilian Amazon averaged 1.89 ± 0.6 million hectares per year from 1995 to 1999, not including areas affected by degradation (INPE, 2000). Brazilian Amazon forests can be a source of CO_2 due to deforestation and degradation. Therefore, accurately mapping forest aboveground biomass (AGB) can help consistently monitor carbon stock changes (e.g., Kashongwe et al., 2020; Santos et al., 2019; Bourgoin et al., 2018; Zald et al. 2016; Saatchi et al., 2007; Houghton et al., 2001). However, traditional methods used for mapping AGB heavily rely on field measurements that is not widely available in the Amazon forest. In addition, field measurements in the Amazon forest are too sparse in time and space to allow spatially sufficient and accurate estimations of aboveground biomass. The airborne LiDAR can be used as an extensive sampling tool to provide supplemental ground information. However, due to the high acquisition cost, the wall-to-wall LiDAR data are always not available over large areas. The combination of airborne LiDAR and Landsat imagery becomes the most practical way to mapping AGB over large areas by taking advantage of reliable structure information derived from LiDAR data and continuous spectral reflectance derived from Landsat imagery (e.g., Wang et al., 2020; Zhang et al., 2019; Ediriweera et al., 2014; Yavasli, 2016).

Due to the high level of biomass and heterogeneity of tropical forests, the previous studies with conventional machine learning models and parametric regression models have lower accuracies in tropical forests compared to boreal and temperate forests (e.g., Bourgoin et al., 2018; Santos et al., 2019; Kashongwe et al., 2020). To enhance the relationship between Landsat spectral reflectance and AGB, previous studies have successfully incorporated the Landsat time-series data (LTS) for AGB estimations (e.g., Copper et al., 2021; Nguyen et al., 2020; Matasic et al., 2018; Kennedy et al., 2018; Boisvenue et al., 2016; Zald et al., 2016; Gómez et al., 2014; Pflugmacher et al. 2012, 2014; Powell et al., 2010, 2014). An early example conducted in the Blue Mountains of eastern Oregon, USA showed that disturbance and regrowth trajectories derived from spectral profiles of annual LTS have a higher correlation with AGB than variables derived from single-date imagery (Pflugmacher et al., 2012). They reported that disturbance and regrowth history metrics significantly improved model accuracy compared to single-date data (R^2 increased from 0.58 to 0.80, RMSE decreased from 65.1 Mg/ha to 46.9 Mg/ha). The value of utilizing disturbance and regrowth change metrics derived from LTS in estimating AGB is further evaluated by recent studies. For instance, Nguyen et al. (2020) derived change metrics from LTS to characterize the changing pattern of AGB in Victoria, Australia. The model with change metrics achieved the RMSE value of 132.9 Mg/ha (RMSE% = 46.3%) and the R^2 value of 0.56. In addition, the relationship of Landsat temporal trajectory metrics and AGB relies on the choice of predictor variables (Deo et al., 2017). For example, Pflugmacher et al. (2012) indicated the strong correlations between live biomass and Tasseled Cap angle (TCA) before and after the greatest disturbance. Zald et al. (2016) indicated Tasseled Cap (TC) indices (including TC angle and TC distance), change metrics (change magnitude, post-change magnitude, years since the greatest change, and post-change evolution rate), and elevation were the most important predicting variables related to AGB. Deo et al. (2017) used six predictors for aboveground biomass modeling: band-5 surface reflectance, normalized difference vegetation index (NDVI), normalized burn ratio (NBR), integrated forest z-score (IFZ), tasseled cap angle (TCA), and disturbance index (DI). However, most previous studies focus on boreal and temperate forests in North America and Europe, none of them explores the relationship between temporal information derived from LST and AGB in tropical forests.

Instead of calculating change metrics from sequence data, recurrent neural networks (RNN) are powerful deep learning methods for directly using sequence data as input to capture time dependencies in modelling process (Sherstinsky, 2020). Two most recent studies have demonstrated the effectiveness and efficiency of RNN, specifically the long short-term memory model (LSTM), in predicting corn and soybean yield (Khaki et al., 2020) and sorghum biomass (Masjedi et al., 2019). Khaki et al. (2020) integrated Conventional Neural Network (CNN) and RNN to forecast corn and soybean yield across the Corn Belt in the United States for years 2016, 2017, and 2018 using historical data. They concluded that the CNN-RNN model was able to capture the time dependencies of environmental factors and the CNN-RNN model outperformed other popular methods (Least Absolute Shrinkage and Selection Operator, Random Forest, and Deep Connected Neural Network). Masjedi et al. (2019) applied RNN to predict sorghum biomass with multi-temporal LiDAR and hyperspectral data. They compared the model performances of RNN and Support Vector Regression (SVR). The results showed that the R^2 of predictions with RNN was higher than those with SVR. The advantages of RNN have also been demonstrated in other research fields, such as the prediction of COVID-19 (Chimmula and Zhang, 2020; Shahid et al., 2020), financial market forecasting (Bukhari et al., 2020; Wang et al., 2021), cyberattacks detection (Gasmi et al., 2019; Kim et al., 2020). However, no studies take advantage of RNN in estimating AGB with LTS data.

In this study, we propose a recurrent neuron network- fully connected neural network (RNN-FNN) model to map forest aboveground biomass in Arc of Deforestation, Brazil with LTS and airborne LiDAR data. The major contributions of this study include: (1) it is the first attempt to utilize RNN in estimating AGB; (2) this study tests the hypothesis that disturbance and regrowth information carried by LTS can significantly improve model accuracy compared to single-date Landsat data in the AGB estimation; (3) this study explores the ability of RNN to deal with LTS data in estimating AGB for tropical forests.

4.2 Study Area and Data

4.2.1 Study area

The study area is located in the Arc of Deforestation, Brazil (**Figure 4.1A**). This region corresponds to one Landsat scene (WRS-2 Path/Row 232/066). GlobeLand30 was applied to understand the land cover and land use in the study area, which is a 30-meter resolution global land cover data product developed by China (Jun et al., 2014). GlobeLand30 can be downloaded from the National Geomatics Center of China (http://www.ngcc.cn/ngcc/html/1/396/400/16121.html). According to the land cover map, eight land cover classes exist in the study area including Cultivated land, Forest, Grassland, Shrub land, Wetland, Water bodies, Artificial surfaces, and Bare land. The Forest class is defined as the land covered with trees, with vegetation cover over 30%. Accordingly, the areas classified as Forest were extracted for further analysis (**Figure 4.1B**).

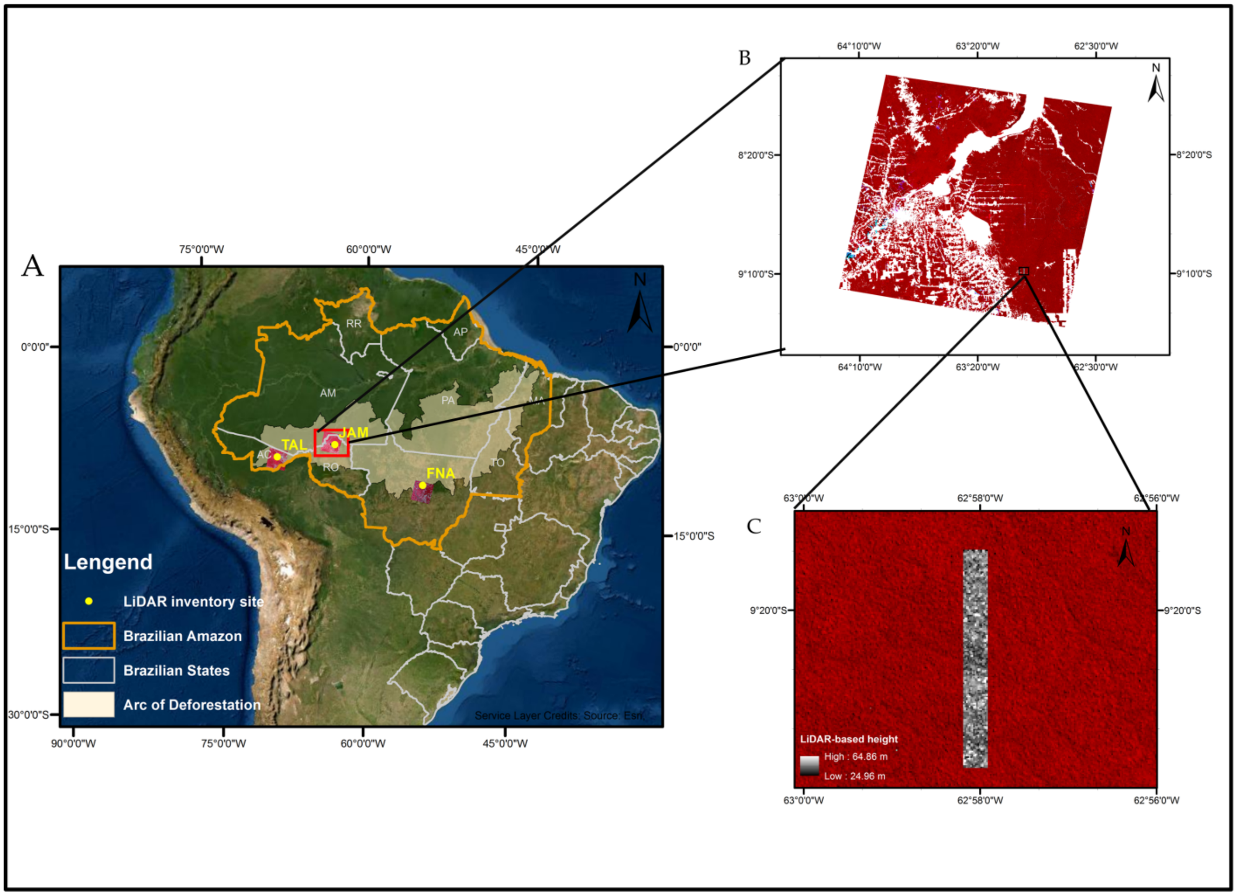

Figure 4.1 Location of study area (A); False color Landsat imagery of forested areas in the study area (B); LiDAR data overlaid on Landsat scene of the study area (C)

4.2.2 Single-date LiDAR-based aboveground biomass calculation

Airborne LiDAR can be used as a sampling tool to significantly increase the number of samples in forests (Wulder et al., 2012b). In this study, single-date LiDAR data was used to generate aboveground biomass density (AGBD) for training and validating the RNN-FNN model. The airborne LiDAR data partially cover the Landsat imagery (**Figure 4.1C**). Three airborne LiDAR inventory sites are available in and near the study area including TAL, JAM, and FNA (Figure 4.1A). The airborne LiDAR data was acquired in 2013 by Geoid Laser Mapping Ltda with the Optech ALTM Orion M-200 sensor. The average flight altitude was 850-900 m above ground and the percentage of flightline overlap was around 65%. The average return density is 34 pt/m^2. The '*lidR*' package (Roussel and Auty, 2019) in R software (R Core Team., 2013) was used to extract LiDAR metrics. According to Equation 4.1 developed in Chapter 2, the LiDAR-based

AGBD is generated in a 30*30 m grid corresponding to the spatial resolution of Landsat 7 ETM+ imagery.

$$\widehat{AGBD} = 0.52H_{max}^{-0.75}H_{entropy}^{-1.78}H_{65th}^{1.49}H_{90th}^{0.83} * 1.24 \quad (4.1)$$

4.2.3 Landsat time-series data pre-processing

Landsat 7 ETM+ surface reflectance images which covered the three LiDAR inventory transects were downloaded from the United States Geological Survey (USGS) website (https://earthexplorer.usgs.gov/). Landsat 7 ETM+ surface reflectance data are generated using the Landsat Ecosystem Disturbance Adaptive Processing System (LEDAPS) algorithm by USGS, which utilizes Moderate Resolution Imaging Spectroradiometer (MODIS) atmospheric correction routines to the standard data product of the Landsat sensors (Masek et al., 2006). The images were acquired from 2004 to 2013 (**Table 4.1**). In order to avoid the effect of phenology, only images acquired from May to September were downloaded. Clouds were manually removed. Due to the failure of scan line corrector (SLC), the Landsat 7 ETM+ images have gaps in a systematic wedge-shaped pattern outside of the central 22 km swath of the imagery since July 2003 (Wulder et al., 2008). The SLC-off gaps were filled with the '*landsat_gapfill*' tool provided by ENVI. Note that the SLC-off images were used in model training phase to avoid involving additional uncertainties. The SLC gap-filled images were only used for generating the final maps.

In total, one hundred and eighty cloud-free WRS-2 scenes of annual Landsat 7 ETM+ surface reflectance images were used to extract surface reflectance (SR) bands, vegetation indices (VIs), and Tasseled Cap (TC) components. Four VIs and three TC components were calculated as predictor variables to compensate for SR bands. They are Normalized Difference Vegetation Index (NDVI), Enhanced Vegetation Index (EVI), Enhanced Vegetation Index 2 (EVI2), Near-infrared reflectance of vegetation (NIRv), Tasseled Cap Brightness (TCB), Tasseled Cap Greenness (TCG), and Tasseled Cap Wetness (TCW). The coefficients for the Tasseled Cap Functions are listed in **Table 4.2.**

Table 4.1 WRS-2 Path/Row and acquisition date of three scenes Landsat 7 ETM+ imagery covering airborne LiDAR inventory sites

Airborne LiDAR Inventory Sites	WRS-2 Path/Row	Date Acquired
JAM	232/066	July 2004; Aug 2005; July 2006; Aug 2007; Aug 2008; June 2009; Aug 2010; July 2011; Sep 2012; July 2013.
TAL	002/067	May 2004; Sep 2005; Sep 2006; Aug 2007; Aug 2008; Aug 2009; June 2010 June 2011; Aug 2012; July 2013.
FNA	226/069	Aug 2004; Aug 2005; Aug 2006; July 2007; July 2008; Aug 2009; Aug 2010; Aug 2011; July 2012; Aug 2013.

Table 4.2 Coefficients for the Tasselled Cap Functions for Landsat ETM+ surface reflectance data (DeVries et al., 2016)

Band	1	2	3	4	5	7
Brightness	0.2043	0.4158	0.5524	0.5741	0.3124	0.2303
Greenness	-0.1603	0.2819	-0.4934	0.7940	-0.0002	-0.1446
Wetness	0.0315	0.2021	0.3102	0.1594	-0.6806	-0.6109

4.3 Methods

4.3.1 RNN-FNN model

The proposed RNN-FNN model, integrating long short-term memory network (LSTM) and fully connected neural network (FNN), consists of k LSTM memory cells and n fully connected layers. **Figure 4.2** demonstrates the architecture of the proposed model. The LSTM network learns the temporal dynamic from the LTS predictors (described in Section 4.2.3) from years t - k to t. The output of LSTM feeds into FNN to predict the AGBD of year t.

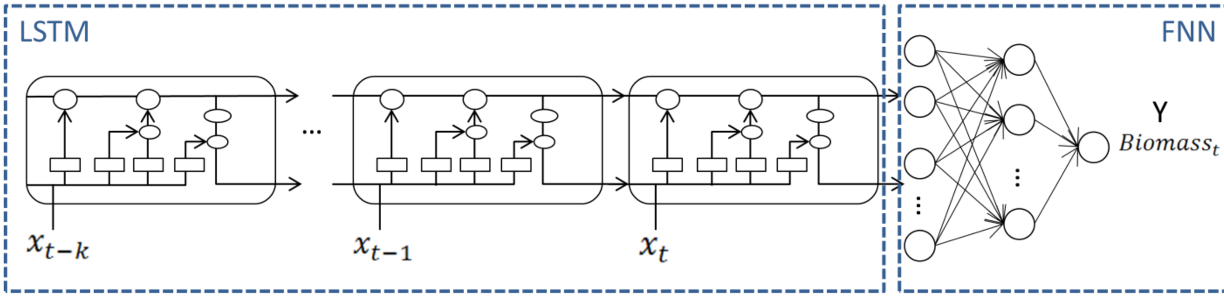

Figure 4.2 Architecture of the proposed RNN-FNN model

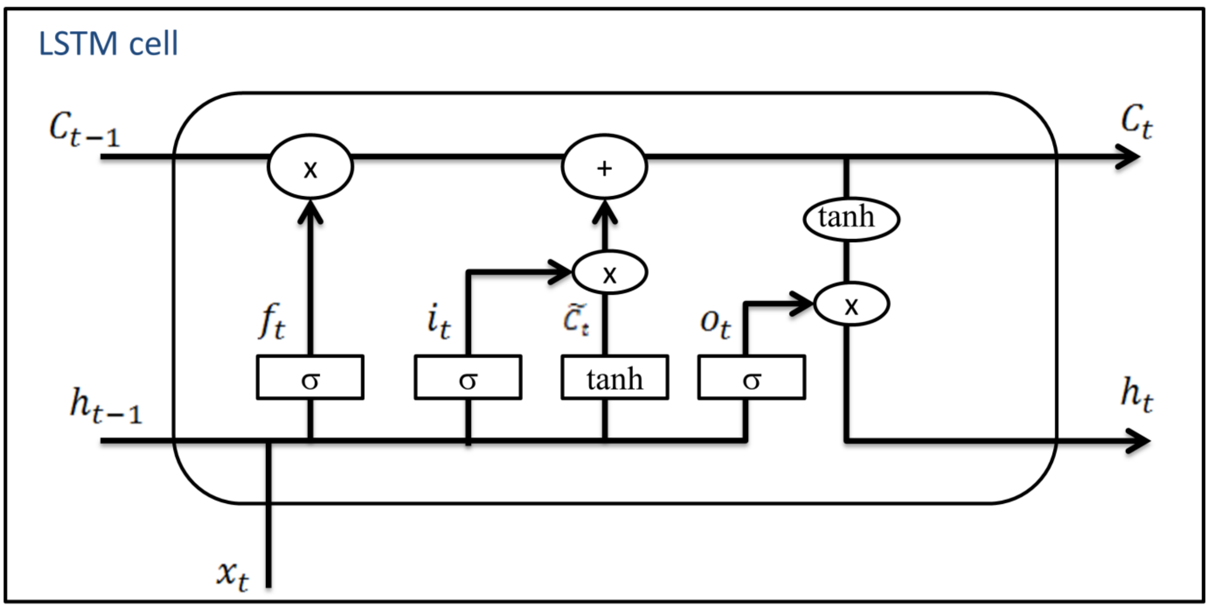

Figure 4.3 Structure of the LSTM cell (Modified and adopted from Reddy et al. (2018))

LSTM is an advanced variant of the traditional recurrent neural network (RNN) that suffers the long-term dependencies problem. LSTM and traditional RNN have similar chain structures. This chain-like nature enables them to connect previous information to the present output. However, unlike traditional RNN, each LSTM memory cell has the gate structure to capture the time dependencies (Hochreiter and Schmidhuber, 1997). The gate structure is composed of three gates including forget gate (f_t), input gate (i_t), and output gate (o_t) (**Figure 4.3**). The first step of a LSTM memory cell is to feed h_{t-1} and $x_t$into the forget gate layer f_t to decide if the information comes from last year should be kept or throw away. The information is completely forgotten if the output is 0. In contrast, all the information is kept if the output is 1 (Equation 4.2). Next, the input gate layer i_t determines the new information that will be stored in the cell (Equation 4.3). Afterward, the candidate C_t is updated by $\tilde{C}_t$ (Equation 4.4, 4.5). Then the output layer o_t generates the information for the output of the cell (Equation 4.6). At last, the output of the memory cell h_t is determined by a *tanh* layer (Equation 4.7) (Equation 4.2 – 4.7 adopted from Reddy et al., (2018)).

$$f_t = \sigma(W_{xf}x_t + W_{hf}h_{t-1} + b_f) \quad 4.2$$

$$i_t = \sigma(W_{xi}x_t + W_{hi}h_{t-1} + b_i) \quad 4.3$$

$$\tilde{C}_t = \tanh(W_{xc}x_t + W_{hc}h_{t-1} + b_c) \quad 4.4$$

$$C_t = f_t C_{t-1} + i_t\tilde{C}_t \quad 4.5$$

$$o_t = \sigma(W_{xo}x_t + W_{ho}h_{t-1} + b_o) \quad 4.6$$

$$h_t = o_t * \tanh(C_t) \quad 4.7$$

The output of LSTM layer feeds into the fully connected layers. The final output *yt* of the FNN is the prediction of AGBD in year *t* (Equation 4.8)

$$y_t = f(\sum wx + b) \quad 4.8$$

where $f(\cdot)$ is the activation function.

4.3.2 Experimental procedure

In order to understand how the time-series length affects the accuracy of RNN-FNN model, the time-series ranging from 1 to 10 years were tested separately. The structure of input 3D tensor of LSTM was reshaped according to different time-series lengths. The three input dimensions represent samples, time steps, and features. **Figure 4.3** demonstrates the example structure of input 3D tensor of LSTM with different time steps. Other hyperparameters of the RNN-FNN model, such as activation function, hidden units, batch size, and kernel initialization, were determined by trial and error.

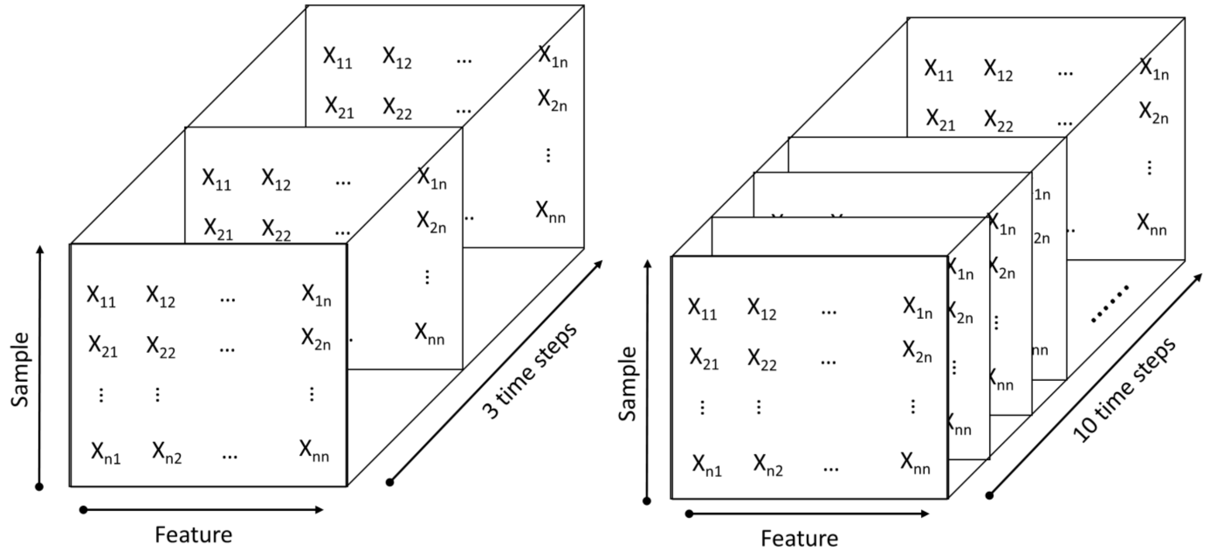

Figure 4.4 Structure of input 3D tensor of LSTM with 3 time steps and 10 time steps

The linear regression model and Random Forest (RF) model were implemented to estimate the AGBD with single-date predictors, i.e., the predictors derived from Landsat ETM+ surface reflectance images in 2013. Eighty percent of the data were used as the training dataset and the other twenty percent of the data were used as the test dataset to evaluate the model performance of the proposed RNN-FNN model with LTS predictors and two classic models with single-date predictors in terms of R^2, RMSE.

The experiments were conducted on Keras with the TensorFlow backend in Python. The free Google Colaboratory 12GB GPU was used to train and test the model.

4.4 Results

4.4.1 Vegetation index dynamics

Throughout the 10-year time-series length (2004-2013), the values of VIs in the JAM, FNA, and TAL sites were demonstrated in **Figure 4.5.** The fluctuation of vegetation conditions in JAM is less significant than it in TAL and FNA. The high occurrences of logging activities and fire events resulted in the fluctuation patterns in the three sites (Longo et al., 2016). In 2010, FNA and TAL were affected by fire events. In the same year, about 35% of JAM had interventions in preparation for logging activities. Accordingly, the values of VIs decreased in 2011. Afterward, recovery was observed. In 2012, fires events occurred again in FNA. So there was a slight decrease in 2013. Although slight differences existed in the patterns of the four VIs in the three sites, they exhibited some general fluctuations of vegetation conditions during the 10 years. It can be observed that the peak values occurred in 2007, 2010, and 2012 year. After these peak years, a low value was observed in the following year, such as 2008, and 2011. The pattern helps the LSTM cells in the RNN-FNN model capture the time dependencies, i.e., a peak value would be followed by a low value.

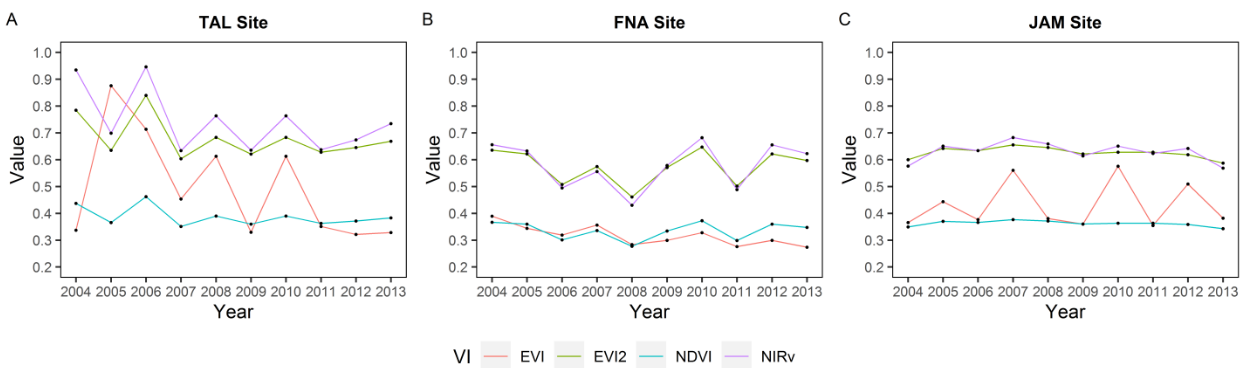

Figure 4.5 Average vegetation Index dynamics over the 10-year time-series (2004-2013) in TAL site (A), FNA site (B), and JAM site (C)

4.4.2 Model performance and comparison

In this study, we propose the RNN-FNN model to predict AGB in 2013 with 13 predictors derived from annual Landsat 7 ETM+ surface reflectance images from 2004 to 2013. In total, 8,354 values of single-date AGB and 13 LTS predictors were generated to train and validate the model. The proposed RNN-FNN model consists of 1 LSTM layer and three fully layers. The model contains 2,389 trainable parameters, including 1,740 parameters in the LSTM layer and 649 are in the fully connected layers. The optimal hyperparameter was determined by independent experiments with a time-series length of 10 years (2004-2013) (**Table 4.3**). Adaptive Momentum Estimation (Adam) was selected as the optimizer and the mean absolute error was used as the loss function. The batch size of 200 and the epoch of 1000 were used to train the model. The same hyperparameters were used in other experiments to evaluate time-series lengths.

Table 4.3 Architecture and hyperparameters of the proposed RNN-FNN model

Layers	Output Shape	Activation Function	# Trainable Parameters
LSTM	(N, 15)	tanh	1740
Fully Connected	(N, 32)	ReLU	512
Fully Connected	(N, 4)	ReLU	132
Fully Connected	(N, 1)	Linear	5

Note: N is the input sample size.

To understand the influence of time-series lengths on the accuracy of RNN-FNN model, time lengths ranging from 2 to 10 years were explored separately. From **Table 4.4**, the model prediction accuracy gradually increased with increasing the time length. The values of testing R^2 increase from 0.44 to 0.63, and the values of RMSE decrease from 31.2 Mg/ha to 25.5 Ma/ha. It can be observed that the accuracy remains stable after 5 years with the testing dataset. Therefore, we assume that the time-series length of 7 years is adequate to capture the trajectory.

Table 4.4 RNN-FNN model performance with different time-series lengths

	Training		Testing	
Time-series Lengths	R^2	RMSE (Mg/ha)	R^2	RMSE (Mg/ha)
2 years (2012-2013)	0.38	35.8	0.44	31.2
3 years (2011-2013)	0.62	28.0	0.46	30.6
4 years (2010-2013)	0.49	32.5	0.56	27.6
5 years (2009-2013)	0.68	25.7	0.53	28.5
6 years (2008-2013)	0.64	27.3	0.60	26.5
7 years (2007-2013)	0.61	28.3	0.62	25.6
8 years (2006-2013)	0.62	28.0	0.60	26.4
9 years (2005-2013)	0.65	27.0	0.62	25.8
10 years (2004-2013)	0.62	28.0	0.63	25.5

To explore the efficiency of the RNN-FNN model with LTS data, linear regression model and RF were used to predict AGB with the same predictors derived from single-date data. The RNN-FNN significantly outperformed linear regression model and RF with the R^2 of 0.63 and RMSE of 25.5 Mg/ha (**Table 4.5**). Although we carefully tuned the parameters of RF, such as the number of trees, it still suffered a serious overfitting problem. That means the RF would have bad performance on unseen data even if it had a very high R^2 in the training phase. In the contrast, the RNN-FNN had similar values of R^2 and RMSE in the training and testing phase, indicating that it would have a similar performance on extrapolation.

Table 4.5 Performance comparison of RNN-FNN model, linear regression model, and RF

		Training		Testing	
Model	Dataset	R^2	RMSE (Mg/ha)	R^2	RMSE (Mg/ha)
RNN-FNN	10-year LTS data (2004-2013)	0.62	28.0	0.63	25.5
RF	Single-date data (2013)	0.90	13.8	0.45	35.2
Linear regression	Single-date data (2013)	0.38	34.6	0.34	38.7

4.4.2 Aboveground biomass distribution

The RNN-FNN model was used to generate the AGBD map of the study area with 10-year time-series predictors (2004-2013) (**Figure 4.6**). The maximum and minimum values of AGBD are 497.2 Mg/ha and 8.5 Mg/ha. The average value is 57.6 Mg/ha. Overall, no obvious AGBD distribution pattern can be observed. Relatively high values can be observed in the northern part and lower values are more concentrated in the middle part.

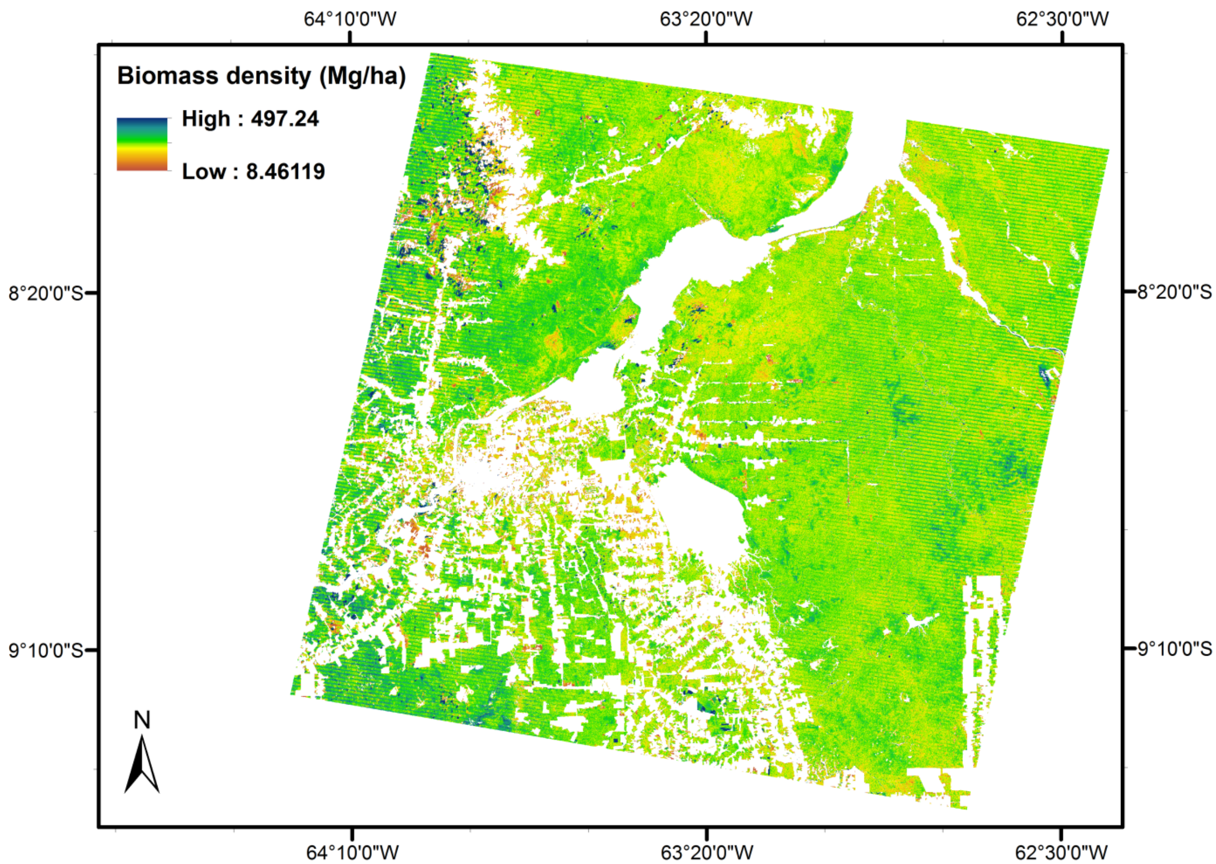

Figure 4.6 Map of AGBD generated by the RNN-FNN model for the study area

4.5 Discussion

This study is the first attempt to utilize RNN in estimating forest biomass. The availability of airborne LiDAR and LTS provides an opportunity to improve the accuracy of biomass estimation in tropical forests with RNN. Limited sample data is the main obstacle to implementing RNN due to its requirement of the volume of training data. In this study, airborne LiDAR provided by Sustainable Landscape Project (SL) was used to significantly increase the sample size. Besides SL, other airborne LiDAR projects (e.g., Improving Biomass Estimation Methods for the Amazon project) and spaceborne LiDAR (e.g., Global Ecosystem Dynamic Investigation) are continuously developing to provide more LiDAR data for forest management. Therefore, the wide application of RNN in forest biomass estimation is promising.

The application of LTS is an ongoing topic of interest, and its value in estimating forest biomass has been demonstrated by previous studies (e.g., Copper et al., 2021; Nguyen et al., 2020; Matasic et al., 2018). However, no attempt has been made to explore the utilization of LTS for estimating biomass in tropical forests. Our results indicate that the RNN-FNN model with LTS significantly outperformed the RF and linear regression models with single-date Landsat data in the Brazilian Amazon. In addition, the model prediction accuracy gradually increased with increasing the time-series length (Table 4.4). We found that the accuracy remains stable after 5 years in this study. A similar conclusion was generated by Pflugmacher et al. (2014). They indicated that as little as 5 years of history were meaningful to derive a relationship between Landsat-based disturbance history and AGB. In addition, they suggested that at least 10-20 years are necessary for a strong relationship in their study region located in the Blue Mountains of eastern Oregon, USA. Similarly, Gómez et al. (2014) indicated that 15-25 years is sufficient for capturing significant temporal patterns to estimate AGB in pine forests, Spain. However, our results suggest that as little as 7 years of history can achieve high accuracy. This may be explained by the shorter recovery period in tropical forests than in temperate forests.

Different LTS change detection methods were used in previous studies, such as Vegetation Change Tracker (Huang et al., 2010), Continuous Change Detection and Classification (Zhu and Woodcock, 2012), Breaks for additive Season and Trend Monitor (Devries et al., 2015), and Landsat-based detection of Trends in Disturbance and Recovery (Kennedy et al., 2010). The performances of these methods on disturbances detections depend on the magnitudes of target changes. High-impact or stand-clearing disturbances can be accurately detected, while changes caused by medium/low-impact disturbances (e.g., selective logging) are more difficult to distinguish and characterize (H Nguyen et al., 2020, Cohen et al. 2017). Therefore, the selection of an appropriate change detection algorithm relies on clear understandings of the target changes, which may be challenging for some specific applications. Instead of using change metrics generated by LTS change detection methods, the RNN-FNN models directly use LTS sequence data as the input in the modeling process. Therefore, the selection of LTS change detection methods is not needed if the RNN-FNN model is used.

Although the advances of the RNN-FNN have been demonstrated in this study, the black box property is the principal shortcoming of deep learning models (Khaki et al., 2020). Due to the complex structures of neural networks, what is learned in their hidden layers is unknown. An increasing number of studies have been conducted to understand the learning behaviors of deep learning models (e.g., Khaki et al., 2020; Shen et al., 2020; Guo et al., 2019; Chen et al., 2018). For example, Khaki et al. (2020) performed a feature selection method to make the CNN-RNN model more explainable. Shen et al. (2020) proposed a visual analytics system to interpret RNNs on multi-dimensional time-series forecasts. Further exploration of model interpretation is needed for the proposed RNN-CNN applied in estimating forest biomass.

4.6 Conclusions

This study proposed an RNN-FNN model, integrating the LSTM and FNN, to estimate AGB with LTS and airborne LiDAR data. The RNN-FNN model yielded an R^2 of 0.63 and RMSE of 25.5 Mg/ha with 10-year time-series data (2004-2013), which outperformed the Random Forest model and linear regression model with single date data. The model prediction accuracy gradually increased with increasing the time-series length. The values of testing R^2 increased from 0.44 to 0.63, and the values of RMSE decreased from 31.2 Mg/ha to 25.5 Ma/ha when the time-series length increased from 2 to 10 years. It can be observed that the accuracy became stable after 5 years with the testing dataset. Therefore, we assume that the time-series length of 7 years is adequate to capture the forest disturbance and recovery trajectory in the study area. At last, the RNN-FNN model was used to generate a map of AGBD for the study area, which demonstrated the practical value of the proposed model.

Chapter 5 Conclusion

5.1 Main Findings

The overarching goal of this research is to develop an efficient framework upscaling biomass from field inventory plot to airborne LiDAR transects and wall-to-wall Landsat imagery level. Three research questions were explored and addressed during the development. The research questions and related findings are summarized as follows.

Question 1: *Which is the best fitting approach to estimate model parameters for multiplicative power models used to explore the relationship between airborne LiDAR metrics and aboveground biomass?*

This question was explored and addressed in Chapter 2. Airborne LiDAR is considered the most accurate remote sensing method for estimate forest biomass (Nguyen et al., 2020). Determining and calibrating the regression model that links LiDAR metrics and biomass inventory data is crucial to accurately map forest biomass over a large area. Multiplicative power models were commonly used to represent the relationship between biomass and LiDAR metrics. There are two approaches to fit the models. The first one is to directly estimate the parameters without log-transformation. The other one is to fit the linear model on a log-transformed scale using the ordinary least squares (OLS) and then back-transform the final model form. However, the differences between the two fitting approaches for the biomass-LiDAR metrics model are not explored. Therefore, three multiplicative power models fitted by nonlinear least-square (NLR), linear ordinary least-square (OLSR), and weighted linear least-square (WLSR) were compared to find the most accurate regression model that would be used to calculate the LiDAR-based biomass in the subsequent chapters.

The ANOVA results indicate significant differences among the three models (OLSR, WLSR, and NLR) in both fitting and prediction phases with 1000 bootstrap realizations in terms of the R^2_{pseudo}, RMSE, %RMSE, and Bias (Table 2.5 & 2.6). Furthermore, the results of Tukey's Test indicate that significant differences existed between the NLR and OLSR or WLSR at 99% confidence level. More extreme predictions were generated by NLR compared to OLSR and

WLSR. NLR had a worse prediction performance. In contrast, OLSR and WLSR were more accurate in prediction.

Question 2: *Can the deep learning techniques improve the accuracy of aboveground biomass estimation in tropical forests with Landsat 8 imagery and airborne LiDAR data?*

This question was explored and addressed in Chapter 3. Due to the high level of biomass and heterogeneity of tropical forests, the commonly used models perform worse in tropical forests compared to boreal and temperate forests. In recent years, deep learning methods have been increasingly used across a variety of remote sensing tasks. However, few studies have utilized deep learning in estimating forest biomass. Therefore, the question aims to explore the capabilities of deep learning in biomass estimations.

A deep feedforward fully connected neural network regression model (DNN) is proposed to link LiDAR-based biomass and Landsat spectral metrics. Compared to the Random Forest model, Support Vector Regression model, and linear regression model, the proposed DNN improved the R^2 from -0.0002 (linear regression model) to 0.64 and reduced the RMSE from 105.3 Mg/ha (linear regression model) to 55.7 Mg/ha (Table 3.9). Different from previous studies, this study found that including vegetation indices and Tasseled Cap components cannot improve the model accuracies. The mathematics behind DNN may contribute to this. A large amount of nonlinear functions exists in hidden layers of DNN. When only SR bands used as predictors, the output of these hidden layers may carry the similar information as VIs and TC components carried. Therefore, it can be concluded that the proposed DNN model can accurately and efficiently to map biomass over a large area without additional calculations of vegetation indices and Tasseled Cap components.

Question 3: *How can the forest disturbance and recovery history derived from Landsat time-series data improve the accuracy of biomass estimation with state-of-art deep learning techniques?*

This question was explored and addressed in Chapter 4. Disturbance and regrowth change metrics derived from Landsat time-series data have been demonstrate of great value in estimating biomass in boreal and temperate forests. However, no studies explore the relationship between

Landsat time-series data and biomass in tropical forests. The study conducted in Chapter 4 proposed an RNN-FNN model to address the research questions.

The proposed RNN-FNN model integrates the long short-term memory network (LSTM) and the fully connected neuron network (FNN). The LSTM network learned the temporal dynamic from the 13 LTS predictors from 2004 to 2013. The output of LSTM fed into FNN to predict the AGBD of the year 2013. The accuracy of RNN-FNN model gradually increased with increasing the time-series length. The values of testing R^2 increased from 0.44 (2 years) to 0.63 (10 years), and the values of RMSE decreased from 31.2 Mg/ha (2 years) to 25.5 Ma/ha (10 years). The RNN-FNN model was compared to the Random Forest model and linear regression implemented with single-date predictors. The results indicate that the RNN-FNN model significantly outperformed the Random Forest model and linear regression model.

5.2 Future Research Opportunities

The accuracy and generality of the regression model linking LiDAR metrics and field-based biomass can be increased to generate more accurate tropical forest biomass maps. Developing separate regression models based on stratified inventory plots is a promising opportunity. The height-diameter (H-D) allometric relationship might be a clue to stratify the inventory plots. However, it remains several challenges. Thomas et al. (1996) used an asymptotic model to describe the H-D relationships in 38 species within 6 genera of Malaysian rain forests. They found that the H-D relationships were affected by species-specific asymptotic maximal tree height. That means that large trees often essentially cease height growth but continue to increase in stem diameter. However, it is challenging to obtain species-specific asymptotic maximal tree height. Thomas et al. (1996) used height and diameter field measurements to estimate asymptotic maximal tree height. But the species in the Malaysian rain forests are different from Amazon forests. Besides, environmental and climatic factors also affect the tropical tree H-D relationship. Feldpausch et al. (2011) found H-D allometry varies along spatial and environmental gradients. Stand-level average H declines more sharply with elevation than does the average D. Soil substrate may also interact with elevation to modulate the H-D relationship. In addition, tree height is limited by water availability. Maximum tree height may be expected to coincide with rainfall distribution. Furthermore, they found that trees growing in regions characterized by occasional but extreme wind events, such as cyclones or hurricanes, would tend to be shorter for a given D than those growing in less perturbed environments. Gorgens et al. (2021) explored the distribution of the tallest trees in the Amazon basin. They found that trees grow taller in areas with high soil clay content (> 42%), lower radiation (< 130 clear days per year), and an optimal precipitation range of 1,500 to 2,500 mm/yr. Therefore, more explorations are needed due to the complexity of the H-D relationship.

Spaceborne LiDAR has the potential to provide consistent measurements of the forest canopy height and canopy vertical structure on a global scale. The Global Ecosystem Dynamic Investigation (GEDI) instrument was launched in December 2018 and starts collecting scientific data in operational mode in March 2019. GEDI is expected to produce about 10 billion cloud-free observations during its 2-year mission length. A very recent study has employed GEDI data and Landsat data to generate a 30 m spatial resolution global forest canopy height map for the year 2019 (Potapov et al., 2021). This study demonstrates the value of integrating GEDI data and Landsat time-series imagery in estimating forest canopy height. The availability of GEDI and Landsat provides the promising opportunity for mapping forest biomass on a continental or global scale.

REFERENCE

Aber, J.D. and Driscoll, C.T., 1997. Effects of land use, climate variation, and N deposition on N cycling and C storage in northern hardwood forests. *Global Biogeochemical Cycles, 11*(4), pp.639-648.

Abshire, J.B., Sun, X., Riris, H., Sirota, J.M., McGarry, J.F., Palm, S., Yi, D. and Liiva, P., 2005. Geoscience laser altimeter system (GLAS) on the ICESat mission: on-orbit measurement performance. *Geaophysical research letters*, *32*(21).

Alencar, A., Nepstad, D. and Diaz, M.C.V., 2006. Forest understory fire in the Brazilian Amazon in ENSO and non-ENSO years: area burned and committed carbon emissions. *Earth Interactions*, *10*(6), pp.1-17.

Andersen, H.E., Barrett, T., Winterberger, K., Strunk, J. and Temesgen, H., 2009, May. Estimating forest biomass on the western lowlands of the Kenai Peninsula of Alaska using airborne lidar and field plot data in a model-assisted sampling design. In *Proceedings of the IUFRO Division 4 Conference:"Extending Forest Inventory and Monitoring over Space and Time* (pp. 19-22).

Andersen, H.E., Reutebuch, S.E., McGaughey, R.J., d'Oliveira, M.V. and Keller, M., 2014. Monitoring selective logging in western Amazonia with repeat lidar flights. *Remote Sensing of Environment*, *151*, pp.157-165.

Angelsen, A. ed., 2008. *Moving ahead with REDD: issues, options and implications*. Cifor.

Arevalo, C.B., Volk, T.A., Bevilacqua, E. and Abrahamson, L., 2007. Development and validation of aboveground biomass estimations for four Salix clones in central New York. Biomass and Bioenergy, 31(1), pp.1-12

Ayrey, E., Hayes, D.J., Kilbride, J.B., Fraver, S., Kershaw, J.A., Cook, B.D. and Weiskittel, A.R., 2019. Synthesizing Disparate LiDAR and Satellite Datasets through Deep Learning to Generate Wall-to-Wall Regional Forest Inventories. *bioRxiv,* p.580514.

Asner, G.P. and Ollinger, S.V., 2009. Remote sensing for terrestrial biogeochemical modeling. The SAGE handbook of remote sensing. *SAGE Publications Ltd., London*, pp.411-422.

Asner, G.P., Powell, G.V., Mascaro, J., Knapp, D.E., Clark, J.K., Jacobson, J., Kennedy-Bowdoin, T., Balaji, A., Paez-Acosta, G., Victoria, E. and Secada, L., 2010. High-resolution forest carbon stocks and emissions in the Amazon. *Proceedings of the National Academy of Sciences*, *107*(38), pp.16738-16742.

Asner, G.P., Mascaro, J., Muller-Landau, H.C., Vieilledent, G., Vaudry, R., Rasamoelina, M., Hall, J.S. and Van Breugel, M., 2012. A universal airborne LiDAR approach for tropical forest carbon mapping. *Oecologia*, *168*(4), pp.1147-1160.

Asner, G.P. and Mascaro, J., 2014. Mapping tropical forest carbon: Calibrating plot estimates to a simple LiDAR metric. Remote Sensing of Environment, 140, pp.614-624.

Avitabile, V., Baccini, A., Friedl, M.A. and Schmullius, C., 2012. Capabilities and limitations of Landsat and land cover data for aboveground woody biomass estimation of Uganda. Remote Sensing of Environment, 117, pp.366-380.

Avitabile, V., Herold, M., Heuvelink, G.B., Lewis, S.L., Phillips, O.L., Asner, G.P., Armston, J., Ashton, P.S., Banin, L., Bayol, N. and Berry, N.J., 2016. An integrated pan-tropical biomass map using multiple reference datasets. *Global change biology*, *22*(4), pp.1406-1420.

Awad, M. and Khanna, R., 2015. Support vector regression. In *Efficient learning machines* (pp. 67-80). Apress, Berkeley, CA.

Babcock, C., Finley, A.O., Andersen, H.E., Pattison, R., Cook, B.D., Morton, D.C., Alonzo, M., Nelson, R., Gregoire, T., Ene, L. and Gobakken, T., 2018. Geostatistical estimation of forest biomass in interior Alaska combining Landsat-derived tree cover, sampled airborne lidar and field observations. *Remote Sensing of Environment*, *212*, pp.212-230.

Baccini, A.G.S.J., Goetz, S.J., Walker, W.S., Laporte, N.T., Sun, M., Sulla-Menashe, D., Hackler, J., Beck, P.S.A., Dubayah, R., Friedl, M.A. and Samanta, S., 2012. Estimated carbon dioxide emissions from tropical deforestation improved by carbon-density maps. *Nature climate change*, *2*(3), pp.182-185.

Baccini, A., Friedl, M.A., Woodcock, C.E. and Warbington, R., 2004. Forest biomass estimation over regional scales using multisource data. *Geophysical research letters*, *31*(10).

Baskerville, G.L., 1972. Use of logarithmic regression in the estimation of plant biomass. Canadian Journal of Forest Research, 2(1), pp.49-53.

Benami, E. and Curran, L.M., 2017, December. Oil Palm Expansion in the Brazilian Amazon (2006-2014): Effects of the 2010 Sustainable Oil Palm Production Program. In *AGU Fall Meeting Abstracts* (Vol. 2017, pp. GC43A-1050).

Bengio, Y., 2009. *Learning deep architectures for AI*. Now Publishers Inc.

Bengio, Y., Courville, A. and Vincent, P., 2013. Representation learning: A review and new perspectives. *IEEE transactions on pattern analysis and machine intelligence*, *35*(8), pp.1798-1828.

Blackard, J.A., Finco, M.V., Helmer, E.H., Holden, G.R., Hoppus, M.L., Jacobs, D.M., Lister, A.J., Moisen, G.G., Nelson, M.D., Riemann, R. and Ruefenacht, B., 2008. Mapping US forest biomass using nationwide forest inventory data and moderate resolution information. *Remote sensing of Environment*, *112*(4), pp.1658-1677.

Boisvenue, C., Smiley, B.P., White, J.C., Kurz, W.A. and Wulder, M.A., 2016. Integration of Landsat time series and field plots for forest productivity estimates in decision support models. *Forest Ecology and Management*, *376*, pp.284-297.

Bourgoin, C., Blanc, L., Bailly, J.S., Cornu, G., Berenguer, E., Oszwald, J., Tritsch, I., Laurent, F., Hasan, A.F., Sist, P. and Gond, V., 2018. The potential of multisource remote sensing for mapping the biomass of a degraded Amazonian forest. *Forests*, *9*(6), p.303.

Breiman, L., 2001. Random forests. *Machine learning*, 45(1), pp.5-32.

Brosofske, K.D., Froese, R.E., Falkowski, M.J. and Banskota, A., 2014. A review of methods for mapping and prediction of inventory attributes for operational forest management. *Forest Science*, *60*(4), pp.733-756.

Brown, I.F., Martinelli, L.A., Thomas, W.W., Moreira, M.Z., Ferreira, C.C. and Victoria, R.A., 1995. Uncertainty in the biomass of Amazonian forests: an example from Rondonia, Brazil. *Forest Ecology and Management*, *75*(1-3), pp.175-189.

Brown, S., Gillespie, A.J. and Lugo, A.E., 1989. Biomass estimation methods for tropical forests with applications to forest inventory data. *Forest science*, *35*(4), pp.881-902.

Brown, S.A.N.D.R.A. and Lugo, A.E., 1992. Aboveground biomass estimates for tropical moist forests of the Brazilian Amazon. *Interciencia. Caracas*, *17*(1), pp.8-18.

Bukhari, A.H., Raja, M.A.Z., Sulaiman, M., Islam, S., Shoaib, M. and Kumam, P., 2020. Fractional neuro-sequential ARFIMA-LSTM for financial market forecasting. *IEEE Access*, *8*, pp.71326-71338.

Clevert, D.A., Unterthiner, T. and Hochreiter, S., 2015. Fast and accurate deep network learning by exponential linear units (elus). *arXiv preprint arXiv:1511.07289*.

Chave, J., Coomes, D., Jansen, S., Lewis, S.L., Swenson, N.G. and Zanne, A.E., 2009. Towards a worldwide wood economics spectrum. Ecology letters, 12(4), pp.351-366.

Chen, J., Song, L., Wainwright, M. and Jordan, M., 2018, July. Learning to explain: An information-theoretic perspective on model interpretation. *In International Conference on Machine Learning* (pp. 883-892). PMLR.

Chen, Q., Laurin, G.V., Battles, J.J. and Saah, D., 2012. Integration of airborne lidar and vegetation types derived from aerial photography for mapping aboveground live biomass. *Remote Sensing of Environment*, *121*, pp.108-117.

Chen, Q. and Qi, C., 2013. Lidar remote sensing of vegetation biomass. *Remote sensing of natural resources*, *399*, pp.399-420.

Chen, Q., Lu, D., Keller, M., Dos-Santos, M.N., Bolfe, E.L., Feng, Y. and Wang, C., 2016. Modeling and mapping agroforestry aboveground biomass in the Brazilian Amazon using airborne lidar data. *Remote Sensing*, *8*(1), p.21.

Change, I.P.O.C., 2001. Climate change 2007: Impacts, adaptation and vulnerability. *Genebra, Suíça*.

Chambers, J.Q., Higuchi, N., Schimel, J.P., Ferreira, L.V. and Melack, J.M., 2000. Decomposition and carbon cycling of dead trees in tropical forests of the central Amazon. Oecologia, 122(3), pp.380-388.

Chimmula, V.K.R. and Zhang, L., 2020. Time series forecasting of COVID-19 transmission in Canada using LSTM networks. *Chaos, Solitons & Fractals*, *135*, p.109864.

Chirici, G., McRoberts, R.E., Fattorini, L., Mura, M. and Marchetti, M., 2016. Comparing echo-based and canopy height model-based metrics for enhancing estimation of forest aboveground biomass in a model-assisted framework. *Remote Sensing of Environment*, *174*, pp.1-9.

Cochran, W.G., 2007. *Sampling techniques*. John Wiley & Sons.

Coltin, B., McMichael, S., Smith, T. and Fong, T., 2016. Automatic boosted flood mapping from satellite data. *International Journal of Remote Sensing*, *37*(5), pp.993-1015.

Cohen, W.B., Healey, S.P., Yang, Z., Stehman, S.V., Brewer, C.K., Brooks, E.B., Gorelick, N., Huang, C., Hughes, M.J., Kennedy, R.E. and Loveland, T.R., 2017. How similar are forest disturbance maps derived from different Landsat time series algorithms?. *Forests, 8*(4), p.98.

Cooper, S., Okujeni, A., Pflugmacher, D., van der Linden, S. and Hostert, P., 2021. Combining simulated hyperspectral EnMAP and Landsat time series for forest aboveground biomass mapping. *International Journal of Applied Earth Observation and Geoinformation*, *98*, p.102307.

Corona, P., Fattorini, L., Franceschi, S., Scrinzi, G. and Torresan, C., 2014. Estimation of standing wood volume in forest compartments by exploiting airborne laser scanning information: model-based, design-based, and hybrid perspectives. *Canadian Journal of Forest Research*, *44*(11), pp.1303-1311.

Cortés, L., Hernández, J., Valencia, D. and Corvalán, P., 2014. Estimation of above-ground forest biomass using Landsat ETM+, Aster GDEM and Lidar. *Forest Res*, *3*(117), p.2.

Crist, E.P. and Cicone, R.C., 1984. A physically-based transformation of Thematic Mapper data---The TM Tasseled Cap. *IEEE Transactions on Geoscience and Remote sensing*, (3), pp.256-263.

Crowley, T.J., 2000. Causes of climate change over the past 1000 years. *Science, 289*(5477), pp.270-277.

Dalto, M., Matuško, J. and Vašak, M., 2015, March. Deep neural networks for ultra-short-term wind forecasting. In *2015 IEEE international conference on industrial technology (ICIT)* (pp. 1657-1663). IEEE.

Dean, J., Corrado, G.S., Monga, R., Chen, K., Devin, M., Le, Q.V., Mao, M.Z., Ranzato, M.A., Senior, A., Tucker, P. and Yang, K., 2012. Large scale distributed deep networks.

DeVries, B., Pratihast, A.K., Verbesselt, J., Kooistra, L. and Herold, M., 2016. Characterizing forest change using community-based monitoring data and Landsat time series. *PloS one*, *11*(3), p.e0147121.

Deo, R.K., Russell, M.B., Domke, G.M., Woodall, C.W., Falkowski, M.J. and Cohen, W.B., 2017. Using Landsat time-series and LiDAR to inform aboveground forest biomass baselines in northern Minnesota, USA. *Canadian Journal of Remote Sensing*, *43*(1), pp.28-47.

Deo, R.K., Domke, G.M., Russell, M.B., Woodall, C.W. and Andersen, H.E., 2018. Evaluating the influence of spatial resolution of Landsat predictors on the accuracy of biomass models for large-area estimation across the eastern USA. *Environmental Research Letters*, *13*(5), p.055004.

DeVries, B., Verbesselt, J., Kooistra, L. and Herold, M., 2015. Robust monitoring of small-scale forest disturbances in a tropical montane forest using Landsat time series. *Remote Sensing of Environment, 161*, pp.107-121.

d'Oliveira, M.V., Reutebuch, S.E., McGaughey, R.J. and Andersen, H.E., 2012. Estimating forest biomass and identifying low-intensity logging areas using airborne scanning lidar in Antimary State Forest, Acre State, Western Brazilian Amazon. *Remote Sensing of Environment*, *124*, pp.479-491.

Dhyani, M. and Kumar, R., 2021. An intelligent Chatbot using deep learning with Bidirectional RNN and attention model. *Materials Today: Proceedings*, *34*, pp.817-824.

Doukim, C.A., Dargham, J.A. and Chekima, A., 2010, May. Finding the number of hidden neurons for an MLP neural network using coarse to fine search technique. In *10th International Conference on Information Science, Signal Processing and their Applications (ISSPA 2010)* (pp. 606-609). IEEE.

Dozat, T., 2016. Incorporating nesterov momentum into adam.

Drake, J.B., Dubayah, R.O., Clark, D.B., Knox, R.G., Blair, J.B., Hofton, M.A., Chazdon, R.L., Weishampel, J.F. and Prince, S., 2002. Estimation of tropical forest structural characteristics using large-footprint lidar. *Remote Sensing of Environment*, *79*(2-3), pp.305-319.

Duchi, J., Hazan, E. and Singer, Y., 2011. Adaptive subgradient methods for online learning and stochastic optimization. *Journal of machine learning research*, *12*(7).

Duncanson, L.I., Niemann, K.O. and Wulder, M.A., 2010. Integration of GLAS and Landsat TM data for aboveground biomass estimation. *Canadian Journal of Remote Sensing*, *36*(2), pp.129-141.

Ediriweera, S., Pathirana, S., Danaher, T. and Nichols, D., 2014. Estimating above-ground biomass by fusion of LiDAR and multispectral data in subtropical woody plant communities in topographically complex terrain in North-eastern Australia. *Journal of forestry research*, *25*(4), pp.761-771.

Ercanl, İ., 2020. Artificial intelligence with deep learning algorithms to model relationships between total tree height and diameter at breast height. *Forest systems*, 29(2), pp.118-1

Eskelson, B.N., Temesgen, H., Lemay, V., Barrett, T.M., Crookston, N.L. and Hudak, A.T., 2009. The roles of nearest neighbor methods in imputing missing data in forest inventory and monitoring databases. *Scandinavian Journal of Forest Research*, *24*(3), pp.235-246.

FAO (2010) Global forests resources assessment 2010. Forestry Paper 163. Food and Agriculture Organization, Rome, Italy.

Fearnside, P.M., 1997. Greenhouse gases from deforestation in Brazilian Amazonia: net committed emissions. *Climatic Change*, *35*(3), pp.321-360.

Fearnside, P.M., 2000. Global warming and tropical land-use change: greenhouse gas emissions from biomass burning, decomposition and soils in forest conversion, shifting cultivation and secondary vegetation. *Climatic change*, *46*(1), pp.115-158.

Fearnside, P., 2017. Deforestation of the Brazilian Amazon. In *Oxford research encyclopedia of environmental science*.

Feldpausch, T.R., Banin, L., Phillips, O.L., Baker, T.R., Lewis, S.L., Quesada, C.A., Affum-Baffoe, K., Arets, E.J., Berry, N.J., Bird, M. and Brondizio, E.S., 2011. Height-diameter allometry of tropical forest trees. *Biogeosciences*, *8*(5), pp.1081-1106.

Feldpausch, T.R., Lloyd, J., Lewis, S.L., Brienen, R.J., Gloor, M., Monteagudo Mendoza, A., Lopez-Gonzalez, G., Banin, L., Abu Salim, K., Affum-Baffoe, K. and Alexiades, M., 2012. Tree height integrated into pantropical forest biomass estimates. *Biogeosciences*, pp.3381-3403.

Friedlingstein, P., Jones, M.W., O'sullivan, M., Andrew, R.M., Hauck, J., Peters, G.P., Peters, W., Pongratz, J., Sitch, S., Le Quéré, C. and Bakker, D.C., 2019. Global carbon budget 2019. *Earth System Science Data, 11*(4), pp.1783-1838.

Fritz, S., Bartholomé, E., Belward, A., Hartley, A., Stibig, H.J., Eva, H., Mayaux, P., Bartalev, S., Latifovic, R., Kolmert, S. and Agrawal, S., 2003. Harmonisation, mosaicing and production of the Global Land Cover 2000 database (Beta Version).

Gasmi, H., Laval, J. and Bouras, A., 2019. Information extraction of cybersecurity concepts: an lstm approach. *Applied Sciences*, *9*(19), p.3945.

Gibbons, J.D. and Chakraborti, S., 2014. *Nonparametric statistical inference: revised and expanded*. CRC press.

Gonçalves, F., Treuhaft, R., Law, B., Almeida, A., Walker, W., Baccini, A., Dos Santos, J.R. and Graça, P., 2017. Estimating aboveground biomass in tropical forests: field methods and error analysis for the calibration of remote sensing observations. *Remote Sensing*, *9*(1), p.47.

Gobakken, T., Næsset, E., Nelson, R., Bollandsås, O.M., Gregoire, T.G., Ståhl, G., Holm, S., Ørka, H.O. and Astrup, R., 2012. Estimating biomass in Hedmark County, Norway using national forest inventory field plots and airborne laser scanning. *Remote Sensing of Environment*, *123*, pp.443-456.

Gómez, C., White, J.C., Wulder, M.A. and Alejandro, P., 2014. Historical forest biomass dynamics modelled with Landsat spectral trajectories. *ISPRS Journal of Photogrammetry and Remote Sensing*, *93*, pp.14-28.

Goodman, R.C., Phillips, O.L., del Castillo Torres, D., Freitas, L., Cortese, S.T., Monteagudo, A. and Baker, T.R., 2013. Amazon palm biomass and allometry. Forest Ecology and Management, 310, pp.994-1004.

Gorgens, E.B., Nunes, M.H., Jackson, T., Coomes, D., Keller, M., Reis, C.R., Valbuena, R., Rosette, J., de Almeida, D.R., Gimenez, B. and Cantinho, R., 2021. Resource availability and disturbance shape maximum tree height across the Amazon. *Global Change Biology*, *27*(1), pp.177-189.

Guo, T., Lin, T. and Antulov-Fantulin, N., 2019, May. Exploring interpretable lstm neural networks over multi-variable data. *In International conference on machine learning* (pp. 2494-2504). PMLR.

Hall, R.J., Skakun, R.S., Arsenault, E.J. and Case, B.S., 2006. Modeling forest stand structure attributes using Landsat ETM+ data: Application to mapping of aboveground biomass and stand volume. *Forest ecology and management*, *225*(1-3), pp.378-390.

Harris, N.L., Brown, S., Hagen, S.C., Saatchi, S.S., Petrova, S., Salas, W., Hansen, M.C., Potapov, P.V. and Lotsch, A., 2012. Baseline map of carbon emissions from deforestation in tropical regions. *Science*, *336*(6088), pp.1573-1576.

Harris, N.L., Gibbs, D.A., Baccini, A., Birdsey, R.A., De Bruin, S., Farina, M., Fatoyinbo, L., Hansen, M.C., Herold, M., Houghton, R.A. and Potapov, P.V., 2021. Global maps of twenty-first century forest carbon fluxes. *Nature Climate Change, 11*(3), pp.234-240.

Hawkins, D.M., Basak, S.C. and Mills, D., 2003. Assessing model fit by cross-validation. *Journal of chemical information and computer sciences*, 43(2), pp.579-586.

Hawryło, P., Francini, S., Chirici, G., Giannetti, F., Parkitna, K., Krok, G., Mitelsztedt, K., Lisańczuk, M., Stereńczak, K., Ciesielski, M. and Wężyk, P., 2020. The Use of Remotely Sensed Data and Polish NFI Plots for Prediction of Growing Stock Volume Using Different Predictive Methods. *Remote Sensing, 12*(20), p.3331.

He, K., Zhang, X., Ren, S. and Sun, J., 2015. Delving deep into rectifiers: Surpassing human-level performance on imagenet classification. In *Proceedings of the IEEE international conference on computer vision* (pp. 1026-1034).

He, K., Zhang, X., Ren, S. and Sun, J., 2016. Deep residual learning for image recognition. In *Proceedings of the IEEE conference on computer vision and pattern recognition* (pp. 770-778).

He, K., Gkioxari, G., Dollár, P. and Girshick, R., 2017. Mask r-cnn. In *Proceedings of the IEEE international conference on computer vision* (pp. 2961-2969).

Hewamalage, H., Bergmeir, C. and Bandara, K., 2021. Recurrent neural networks for time series forecasting: Current status and future directions. *International Journal of Forecasting*, *37*(1), pp.388-427.

Helmer, E.H., Lefsky, M.A. and Roberts, D.A., 2009. Biomass accumulation rates of Amazonian secondary forest and biomass of old-growth forests from Landsat time series and the Geoscience Laser Altimeter System. *Journal of Applied Remote Sensing*, *3*(1), p.033505.

Higuchi, N., 1995. Fitomassa e conteúdo de carbono de espécies arbóreas da Amazônia. *Emissão x Seqüestro de CO2-Uma Nova Oportunidade de Negócios para o Brasil, pgs. 125-154*.

Hinton, G. and Tieleman, T., 2012. Lecture 6.5-rmsprop. *COURSERA: Neural networks for machine learning*.

H Nguyen, T., Jones, S., Soto-Berelov, M., Haywood, A. and Hislop, S., 2020. Landsat time-series for estimating forest aboveground biomass and its dynamics across space and time: A review. *Remote Sensing, 12*(1), p.98.

Hochreiter, S. and Schmidhuber, J., 1997. Long short-term memory. *Neural computation, 9(8)*, pp.1735-1780.

Houghton, R.A., Skole, D.L., Nobre, C.A., Hackler, J.L., Lawrence, K.T. and Chomentowski, W.H., 2000. Annual fluxes of carbon from deforestation and regrowth in the Brazilian Amazon. *Nature*, *403*(6767), pp.301-304.

Houghton, R.A., Lawrence, K.T., Hackler, J.L. and Brown, S., 2001. The spatial distribution of forest biomass in the Brazilian Amazon: a comparison of estimates. *Global Change Biology*, *7*(7), pp.731-746.

Houghton, R.A. and Nassikas, A.A., 2017. Global and regional fluxes of carbon from land use and land cover change 1850–2015. *Global Biogeochemical Cycles, 31*(3), pp.456-472.

Houghton, R.A., 2005. Aboveground forest biomass and the global carbon balance. *Global change biology*, *11*(6), pp.945-958.

Houghton, R.A. and Nassikas, A.A., 2017. Global and regional fluxes of carbon from land use and land cover change 1850–2015. *Global Biogeochemical Cycles*, *31*(3), pp.456-472.

Huang, G.B., 2003. Learning capability and storage capacity of two-hidden-layer feedforward networks. *IEEE transactions on neural networks*, *14*(2), pp.274-281.

Huang, C., Goward, S.N., Masek, J.G., Thomas, N., Zhu, Z. and Vogelmann, J.E., 2010. An automated approach for reconstructing recent forest disturbance history using dense Landsat time series stacks. *Remote Sensing of Environment, 114*(1), pp.183-198.

Hyde, P., Dubayah, R., Walker, W., Blair, J.B., Hofton, M. and Hunsaker, C., 2006. Mapping forest structure for wildlife habitat analysis using multi-sensor (LiDAR, SAR/InSAR, ETM+, Quickbird) synergy. *Remote Sensing of Environment*, *102*(1-2), pp.63-73.

Knapp, N., Fischer, R., Cazcarra-Bes, V. and Huth, A., 2020. Structure metrics to generalize biomass estimation from lidar across forest types from different continents. *Remote Sensing of Environment, 237*, p.111597.

Ide, H. and Kurita, T., 2017, May. Improvement of learning for CNN with ReLU activation by sparse regularization. In *2017 International Joint Conference on Neural Networks (IJCNN)* (pp. 2684-2691). IEEE.

IPCC, 2007. Climate Change 2007: the physical science basis. Contribution of Working Group I to the Fourth Assessment Report of the Intergovernmental Panel on Climate Change. WMO/UNEP, Paris, France, 18 pp.

IPCC Climate Change 2014: Synthesis Report (eds Core Writing Team,Pachauri, R. K. & Meyer L. A.) (IPCC, 2014).

IPCC Special Report on Climate Change, Desertification, Land Degradation, Sustainable Land Management, Food Security, and Greenhouse Gas Fluxes in Terrestrial Ecosystems (IPCC, 2019).

INPE, 2000. Deforestation estimates in the Brazilian Amazon. Instituto Nacional de Pesquisas Espaciais, Sa˜o Jose´ dos Campos, Brazil.

Isensee, F., Jaeger, P.F., Kohl, S.A., Petersen, J. and Maier-Hein, K.H., 2021. nnU-Net: a self-configuring method for deep learning-based biomedical image segmentation. *Nature Methods*, *18*(2), pp.203-211.

Ithapu, V.K., Ravi, S.N. and Singh, V., 2017. On architectural choices in deep learning: From network structure to gradient convergence and parameter estimation. *arXiv preprint arXiv:1702.08670*.

Jakubauskas, M.E., 1996. Thematic Mapper characterization of lodgepole pine seral stages in Yellowstone National Park, USA. *Remote sensing of environment*, *56*(2), pp.118-132.

Jakubauskas, M.E. and Price, K.P., 1997. Emperical relationships between structural and spectral factors of yellowstone lodgepole pine forests. *Photogrammetric engineering and remote sensing*, *63*(12), pp.1375-1380.

Jiang, X., Li, G., Lu, D., Chen, E. and Wei, X., 2020. Stratification-Based Forest Aboveground Biomass Estimation in a Subtropical Region Using Airborne Lidar Data. *Remote Sensing*, 12(7), p.1101.

Jiménez, E., Vega, J.A., Fernandez-Alonso, J.M., Vega-Nieva, D., Ortiz, L., Lopez-Serrano, P.M. and López-Sánchez, C.A., 2017. Estimation of aboveground forest biomass in Galicia (NW Spain) by the combined use of LiDAR, LANDSAT ETM+ and National Forest Inventory data. *iForest-Biogeosciences and Forestry*, *10*(3), p.590.

Jin, L., Yan, J., Du, X., Xiao, X. and Fu, D., 2020. RNN for solving time-variant generalized Sylvester equation with applications to robots and acoustic source localization. *IEEE Transactions on Industrial Informatics*, *16*(10), pp.6359-6369.

Jordan, C.F. and CF, J., 1978. Biomass of a" tierra firme" forest of the Amazon Basin.

Jun, C., Ban, Y. and Li, S., 2014. Open access to Earth land-cover map. *Nature, 514*(7523), pp.434-434.

Jurjević, L., Liang, X., Gašparović, M. and Balenović, I., 2020. Is field-measured tree height as reliable as believed–Part II, A comparison study of tree height estimates from conventional field measurement and low-cost close-range remote sensing in a deciduous forest. *ISPRS Journal of Photogrammetry and Remote Sensing, 169*, pp.227-241.

Kashongwe, H.B., Roy, D.P. and Bwangoy, J.R.B., 2020. Democratic Republic of the Congo Tropical Forest Canopy Height and Aboveground Biomass Estimation with Landsat-8 Operational Land Imager (OLI) and Airborne LiDAR Data: The Effect of Seasonal Landsat Image Selection. *Remote Sensing*, *12*(9), p.1360.

Keller, M., Palace, M., Asner, G.P., Pereira Jr, R. and Silva, J.N.M., 2004. Coarse woody debris in undisturbed and logged forests in the eastern Brazilian Amazon. Global Change Biology, 10(5), pp.784-795.

Kennedy, R.E., Yang, Z. and Cohen, W.B., 2010. Detecting trends in forest disturbance and recovery using yearly Landsat time series: 1. LandTrendr—Temporal segmentation algorithms. *Remote Sensing of Environment*, *114*(12), pp.2897-2910.

Kennedy, R.E., Ohmann, J., Gregory, M., Roberts, H., Yang, Z., Bell, D.M., Kane, V., Hughes, M.J., Cohen, W.B., Powell, S. and Neeti, N., 2018. An empirical, integrated forest biomass monitoring system. *Environmental Research Letters*, *13*(2), p.025004.

Klambauer, G., Unterthiner, T., Mayr, A. and Hochreiter, S., 2017. Self-normalizing neural networks. *arXiv preprint arXiv:1706.02515*.

Kim, G., Lee, C., Jo, J. and Lim, H., 2020. Automatic extraction of named entities of cyber threats using a deep Bi-LSTM-CRF network. *International journal of machine learning and cybernetics*, *11*(10), pp.2341-2355.

Kingma, D.P. and Ba, J., 2014. Adam: A method for stochastic optimization. *arXiv preprint arXiv:1412.6980*.

Khaki, S., Wang, L. and Archontoulis, S.V., 2020. A cnn-rnn framework for crop yield prediction. *Frontiers in Plant Science*, *10*, p.1750.

Khumprom, P. and Yodo, N., 2019. A data-driven predictive prognostic model for lithium-ion batteries based on a deep learning algorithm. *Energies*, *12*(4), p.660.

Lang, N., Schindler, K. and Wegner, J.D., 2019. Country-wide high-resolution vegetation height mapping with Sentinel-2. *Remote Sensing of Environment, 233*, p.111347.

Larsen, A., Hanigan, I., Reich, B.J., Qin, Y., Cope, M., Morgan, G. and Rappold, A.G., 2021. A deep learning approach to identify smoke plumes in satellite imagery in near-real time for health risk communication. *Journal of exposure science & environmental epidemiology, 31(1)*, pp.170-176.

Lathuilière, S., Mesejo, P., Alameda-Pineda, X. and Horaud, R., 2019. A comprehensive analysis of deep regression. *IEEE transactions on pattern analysis and machine intelligence*, *42*(9), pp.2065-2081.

Le Toan, T., Quegan, S., Woodward, I., Lomas, M., Delbart, N. and Picard, G., 2004. Relating radar remote sensing of biomass to modelling of forest carbon budgets. *Climatic Change*, *67*(2), pp.379-402.

LeCun, Y.A., Bottou, L., Orr, G.B. and Müller, K.R., 2012. Efficient backprop. In *Neural networks: Tricks of the trade* (pp. 9-48). Springer, Berlin, Heidelberg.

LeCun, Y., Bengio, Y. and Hinton, G., 2015. Deep learning. *nature*, *521*(7553), pp.436-444.

Lefsky, M.A., Cohen, W.B., Parker, G.G. and Harding, D.J., 2002. Lidar remote sensing for ecosystem studies: Lidar, an emerging remote sensing technology that directly measures the three-dimensional distribution of plant canopies, can accurately estimate vegetation structural attributes and should be of particular interest to forest, landscape, and global ecologists. *BioScience*, *52*(1), pp.19-30.

Liaw, A. and Wiener, M., 2002. Classification and regression by randomForest. R news, 2(3), pp.18-22.

Liu, H., Shen, X., Cao, L., Yun, T., Zhang, Z., Fu, X., Chen, X. and Liu, F., 2020. Deep Learning in Forest Structural Parameter Estimation Using Airborne LiDAR Data. IEEE Journal of Selected Topics in *Applied Earth Observations and Remote Sensing, 14*, pp.1603-1618.

Longo, M., Keller, M., dos-Santos, M.N., Leitold, V., Pinagé, E.R., Baccini, A., Saatchi, S., Nogueira, E.M., Batistella, M. and Morton, D.C., 2016. Aboveground biomass variability across intact and degraded forests in the Brazilian Amazon. *Global Biogeochemical Cycles*, *30*(11), pp.1639-1660.

Lu, D., 2005. Aboveground biomass estimation using Landsat TM data in the Brazilian Amazon. *International journal of remote sensing*, *26*(12), pp.2509-2525.

Lu, D., 2006. The potential and challenge of remote sensing-based biomass estimation. *International journal of remote sensing*, *27*(7), pp.1297-1328.

Lu, D., Chen, Q., Wang, G., Moran, E., Batistella, M., Zhang, M., Vaglio Laurin, G. and Saah, D., 2012. Aboveground forest biomass estimation with Landsat and LiDAR data and uncertainty analysis of the estimates. *International Journal of Forestry Research*, *2012*.

Luo, Y., Chen, Z. and Yoshioka, T., 2020, May. Dual-path rnn: efficient long sequence modeling for time-domain single-channel speech separation. In *ICASSP 2020-2020 IEEE International Conference on Acoustics, Speech and Signal Processing (ICASSP)* (pp. 46-50). IEEE

Lymburner, L., Beggs, P.J. and Jacobson, C.R., 2000. Estimation of canopy-average surface-specific leaf area using Landsat TM data. *Photogrammetric Engineering and Remote Sensing*, *66*(2), pp.183-192.

Maas, A.L., Hannun, A.Y. and Ng, A.Y., 2013, June. Rectifier nonlinearities improve neural network acoustic models. In *Proc. icml* (Vol. 30, No. 1, p. 3).

Magurran, A.E., 2013. *Measuring biological diversity*. John Wiley & Sons.

Matasci, G., Hermosilla, T., Wulder, M.A., White, J.C., Coops, N.C., Hobart, G.W. and Zald, H.S., 2018. Large-area mapping of Canadian boreal forest cover, height, biomass and other structural attributes using Landsat composites and lidar plots. *Remote sensing of environment*, *209*, pp.90-106.

Mascaro, J., Litton, C.M., Hughes, R.F., Uowolo, A. and Schnitzer, S.A., 2011. Minimizing bias in biomass allometry: model selection and log-transformation of data. Biotropica, 43(6), pp.649-653.

Masek, J.G., Vermote, E.F., Saleous, N.E., Wolfe, R., Hall, F.G., Huemmrich, K.F., Gao, F., Kutler, J. and Lim, T.K., 2006. A Landsat surface reflectance dataset for North America, 1990-2000*. IEEE Geoscience and Remote Sensing Letters, 3*(1), pp.68-72.

Masjedi, A., Carpenter, N.R., Crawford, M.M. and Tuinstra, M.R., 2019. Prediction of sorghum biomass using UAV time series data and recurrent neural networks. In *Proceedings of the IEEE/CVF Conference on Computer Vision and Pattern Recognition Workshops* (pp. 0-0).

Means, J.E., Acker, S.A., Harding, D.J., Blair, J.B., Lefsky, M.A., Cohen, W.B., Harmon, M.E. and McKee, W.A., 1999. Use of large-footprint scanning airborne lidar to estimate forest stand characteristics in the Western Cascades of Oregon. *Remote sensing of environment*, *67*(3), pp.298-308.

Merkel, G.D., Povinelli, R.J. and Brown, R.H., 2018. Short-term load forecasting of natural gas with deep neural network regression. *Energies*, *11*(8), p.2008.

Mitchard, E.T., Feldpausch, T.R., Brienen, R.J., Lopez-Gonzalez, G., Monteagudo, A., Baker, T.R., Lewis, S.L., Lloyd, J., Quesada, C.A., Gloor, M. and Ter Steege, H., 2014. Markedly divergent estimates of A mazon forest carbon density from ground plots and satellites. *Global Ecology and Biogeography*, *23*(8), pp.935-946.

Mourgias-Alexandris, G., Tsakyridis, A., Passalis, N., Tefas, A., Vyrsokinos, K. and Pleros, N., 2019. An all-optical neuron with sigmoid activation function. *Optics express*, *27*(7), pp.9620-9630.

Nair, V. and Hinton, G.E., 2010, January. Rectified linear units improve restricted boltzmann machines. In *Icml*.

Narine, L.L., Popescu, S.C. and Malambo, L., 2019. Synergy of ICESat-2 and Landsat for mapping forest aboveground biomass with deep learning. *Remote Sensing*, *11*(12), p.1503.

Neigh, C.S., Nelson, R.F., Ranson, K.J., Margolis, H.A., Montesano, P.M., Sun, G., Kharuk, V., Næsset, E., Wulder, M.A. and Andersen, H.E., 2013. Taking stock of circumboreal forest carbon with ground measurements, airborne and spaceborne LiDAR. *Remote Sensing of Environment*, *137*, pp.274-287.

Nelson, R., Gobakken, T., Næsset, E., Gregoire, T.G., Ståhl, G., Holm, S. and Flewelling, J., 2012. Lidar sampling—Using an airborne profiler to estimate forest biomass in Hedmark County, Norway. *Remote sensing of environment*, *123*, pp.563-578.

Nevavuori, P., Narra, N. and Lipping, T., 2019. Crop yield prediction with deep convolutional neural networks. *Computers and electronics in agriculture, 163*, p.104859.

Nogueira, E.M., Fearnside, P.M., Nelson, B.W., Barbosa, R.I. and Keizer, E.W.H., 2008. Estimates of forest biomass in the Brazilian Amazon: New allometric equations and adjustments to biomass from wood-volume inventories. *Forest Ecology and Management*, *256*(11), pp.1853-1867.

Nogueira, E.M., Yanai, A.M., Fonseca, F.O. and Fearnside, P.M., 2015. Carbon stock loss from deforestation through 2013 in Brazilian Amazonia. *Global change biology*, *21*(3), pp.1271-1292.

Nguyen, T.H., Jones, S.D., Soto-Berelov, M., Haywood, A. and Hislop, S., 2020. Monitoring aboveground forest biomass dynamics over three decades using Landsat time-series and single-date inventory data. *International Journal of Applied Earth Observation and Geoinformation*, *84*, p.101952.

Ogana, F.N. and Ercanli, I., 2021. Modelling height-diameter relationships in complex tropical rain forest ecosystems using deep learning algorithm. *Journal of Forestry Research*, pp.1-16.

Otto, P., Vallejo-Rodríguez, R., Keesstra, S., León-Becerril, E., de Anda, J., Hernández-Mena, L., del Real-Olvera, J. and Díaz-Torres, J.D.J., 2020. Time Delay Evaluation on the Water-Leaving Irradiance Retrieved from Empirical Models and Satellite Imagery. *Remote Sensing*, *12*(1), p.87.

Overman, J.P.M., Witte, H.J.L. and Saldarriaga, J.G., 1994. Evaluation of regression models for above-ground biomass determination in Amazon rainforest. *Journal of tropical Ecology*, *10*(2), pp.207-218.

Palace, M., Keller, M., Asner, G.P., Silva, J.N.M. and Passos, C., 2007. Necromass in undisturbed and logged forests in the Brazilian Amazon. Forest Ecology and Management, 238(1-3), pp.309-318.

Pan, Y., Birdsey, R.A., Fang, J., Houghton, R., Kauppi, P.E., Kurz, W.A., Phillips, O.L., Shvidenko, A., Lewis, S.L., Canadell, J.G. and Ciais, P., 2011. A large and persistent carbon sink in the world's forests. *Science*, *333*(6045), pp.988-993.

Parton, W.J., Stewart, J.W. and Cole, C.V., 1988. Dynamics of C, N, P and S in grassland soils: a model. *Biogeochemistry, 5*(1), pp.109-131.

Phillips, O.L., Malhi, Y., Higuchi, N., Laurance, W.F., Núnez, P.V., Vásquez, R.M., Laurance, S.G., Ferreira, L.V., Stern, M., Brown, S. and Grace, J., 1998. Changes in the carbon balance of tropical forests: evidence from long-term plots. *Science*, *282*(5388), pp.439-442.

Phua, M.H., Johari, S.A., Wong, O.C., Ioki, K., Mahali, M., Nilus, R., Coomes, D.A., Maycock, C.R. and Hashim, M., 2017. Synergistic use of Landsat 8 OLI image and airborne LiDAR data for above-ground biomass estimation in tropical lowland rainforests. *Forest ecology and management*, *406*, pp.163-171.

Potter, C.S., 1999. Terrestrial biomass and the effects of deforestation on the global carbon cycle: results from a model of primary production using satellite observations. *BioScience*, *49*(10), pp.769-778.

Powell, S.L., Cohen, W.B., Healey, S.P., Kennedy, R.E., Moisen, G.G., Pierce, K.B. and Ohmann, J.L., 2010. Quantification of live aboveground forest biomass dynamics with Landsat time-series and field inventory data: A comparison of empirical modeling approaches. *Remote Sensing of Environment*, *114*(5), pp.1053-1068.

Powell, S.L., Cohen, W.B., Kennedy, R.E., Healey, S.P. and Huang, C., 2014. Observation of trends in biomass loss as a result of disturbance in the conterminous US: 1986–2004. *Ecosystems*, *17*(1), pp.142-157.

Putz, F.E., Zuidema, P.A., Synnott, T., Peña-Claros, M., Pinard, M.A., Sheil, D., Vanclay, J.K., Sist, P., Gourlet-Fleury, S., Griscom, B. and Palmer, J., 2012. Sustaining conservation values in selectively logged tropical forests: the attained and the attainable. *Conservation Letters*, *5*(4), pp.296-303.

Putz, Francis E., et al. "Sustaining conservation values in selectively logged tropical forests: the attained and the attainable." *Conservation Letters* 5.4 (2012): 296-303.

R Core Team (2013). R: A language and environment for statistical computing. R Foundation for Statistical Computing, Vienna, Austria. ISBN 3-900051-07-0, URL http://www.R-project.org/.

Ramachandran, P., Zoph, B. and Le, Q.V., 2017. Swish: a self-gated activation function. *arXiv preprint arXiv:1710.05941*, *7*, p.1.

Raschka, S., 2018. Model evaluation, model selection, and algorithm selection in machine learning. arXiv preprint arXiv:1811.12808.

Reddy, D.S. and Prasad, P.R.C., 2018. Prediction of vegetation dynamics using NDVI time series data and LSTM. *Modeling Earth Systems and Environment, 4*(1), pp.409-419.

Reddy, T., RM, S.P., Parimala, M., Chowdhary, C.L., Hakak, S. and Khan, W.Z., 2020. A deep neural networks based model for uninterrupted marine environment monitoring. *Computer Communications*, *157*, pp.64-75.

Ren, S., He, K., Girshick, R., & Sun, J. (2015). Faster r-cnn: Towards real-time object detection with region proposal networks. *arXiv preprint arXiv:1506.01497*.

Roussel, Jean-Romain and Auty, David (2019). lidR: Airborne LiDAR Data Manipulation and Visualization for Forestry Applications. R package version 2.0.3. https://CRAN.R-project.org/package=lidR

Saldarriaga, J.G., West, D.C., Tharp, M.L. and Uhl, C., 1988. Long-term chronosequence of forest succession in the upper Rio Negro of Colombia and Venezuela. *The Journal of Ecology*, pp.938-958.

Saatchi, S.S., HOUGHTON, R.A., Dos Santos Alvala, R.C., Soares, J.V. and Yu, Y., 2007. Distribution of aboveground live biomass in the Amazon basin. *Global change biology*, *13*(4), pp.816-837.

Saatchi, S.S., Harris, N.L., Brown, S., Lefsky, M., Mitchard, E.T., Salas, W., Zutta, B.R., Buermann, W., Lewis, S.L., Hagen, S. and Petrova, S., 2011. Benchmark map of forest carbon stocks in tropical regions across three continents. *Proceedings of the national academy of sciences*, *108*(24), pp.9899-9904.

Saatchi, S.S., Harris, N.L., Brown, S., Lefsky, M., Mitchard, E.T., Salas, W., Zutta, B.R., Buermann, W., Lewis, S.L., Hagen, S. and Petrova, S., 2011. Benchmark map of forest carbon stocks in tropical regions across three continents. *Proceedings of the national academy of sciences*, *108*(24), pp.9899-9904.

Santos, E.G.D., Shimabukuro, Y.E., Mendes De Moura, Y., Gonçalves, F.G., Jorge, A., Gasparini, K.A., Arai, E., Duarte, V. and Ometto, J.P., 2019. Multi-scale approach to estimating aboveground biomass in the Brazilian Amazon using Landsat and LiDAR data. *International Journal of Remote Sensing*, *40*(22), pp.8635-8645.

Schimel, D., Stephens, B.B. and Fisher, J.B., 2015. Effect of increasing CO2 on the terrestrial carbon cycle. *Proceedings of the National Academy of Sciences, 112*(2), pp.436-441.

Schnitzer, S.A., DeWalt, S.J. and Chave, J., 2006. Censusing and Measuring Lianas: A Quantitative Comparison of the Common Methods 1. Biotropica, 38(5), pp.581-591.

Schwarz, G., 1978. Estimating the dimension of a model. The annals of statistics, 6(2), pp.461-464.

Shahid, F., Zameer, A. and Muneeb, M., 2020. Predictions for COVID-19 with deep learning models of LSTM, GRU and Bi-LSTM. *Chaos, Solitons & Fractals*, *140*, p.110212.

Shao, Z., Zhang, L. and Wang, L., 2017. Stacked sparse autoencoder modeling using the synergy of airborne LiDAR and satellite optical and SAR data to map forest above-ground biomass. *IEEE Journal of Selected Topics in Applied Earth Observations and Remote Sensing, 10(12)*, pp.5569-5582

Shen, Q., Wu, Y., Jiang, Y., Zeng, W., Alexis, K.H., Vianova, A. and Qu, H., 2020, June. Visual interpretation of recurrent neural network on multi-dimensional time-series forecast. *In 2020 IEEE Pacific Visualization Symposium* (PacificVis) (pp. 61-70). IEEE.

Sherstinsky, A., 2020. Fundamentals of recurrent neural network (RNN) and long short-term memory (LSTM) network. *Physica D: Nonlinear Phenomena*, *404*, p.132306.

Shuman, C.A., Zwally, H.J., Schutz, B.E., Brenner, A.C., DiMarzio, J.P., Suchdeo, V.P. and Fricker, H.A., 2006. ICESat Antarctic elevation data: Preliminary precision and accuracy assessment. *Geophysical Research Letters*, *33*(7).

Smith, L.N., 2018. A disciplined approach to neural network hyper-parameters: Part 1--learning rate, batch size, momentum, and weight decay. *arXiv preprint arXiv:1803.09820*.

Simonyan, K. and Zisserman, A., 2014. Very deep convolutional networks for large-scale image recognition. *arXiv preprint arXiv:1409.1556*.

Silva, C.A., Santilli, G., Sano, E.E. and Laneve, G., 2021. Fire occurrences and greenhouse gas emissions from deforestation in the Brazilian Amazon. *Remote Sensing*, *13*(3), p.376.

Silveira, E.M., Silva, S.H.G., Acerbi-Junior, F.W., Carvalho, M.C., Carvalho, L.M.T., Scolforo, J.R.S. and Wulder, M.A., 2019a. Object-based random forest modelling of aboveground forest biomass outperforms a pixel-based approach in a heterogeneous and mountain tropical environment. *International Journal of Applied Earth Observation and Geoinformation*, *78*, pp.175-188.

Silveira, E.M., Santo, F.D.E., Wulder, M.A., Júnior, F.W.A., Carvalho, M.C., Mello, C.R., Mello, J.M., Shimabukuro, Y.E., Terra, M.C.N.S., Carvalho, L.M.T. and Scolforo, J.R., 2019b. Pre-stratified modelling plus residuals kriging reduces the uncertainty of aboveground biomass estimation and spatial distribution in heterogeneous savannas and forest environments. *Forest ecology and management*, *445*, pp.96-109.

Song, Y., Zhou, H., Wang, P. and Yang, M., 2019. Prediction of clathrate hydrate phase equilibria using gradient boosted regression trees and deep neural networks. *The Journal of Chemical Thermodynamics*, *135*, pp.86-96.

Song, Y., Zheng, S., Li, L., Zhang, X., Zhang, X., Huang, Z., Chen, J., Wang, R., Zhao, H., Zha, Y. and Shen, J., 2021. Deep learning enables accurate diagnosis of novel coronavirus (COVID-19) with CT images. *IEEE/ACM Transactions on Computational Biology and Bioinformatics*.

Song, Z., Sui, H. and Hua, L., 2021. A hierarchical object detection method in large-scale optical remote sensing satellite imagery using saliency detection and CNN. *International Journal of Remote Sensing, 42(8)*, pp.2827-2847.

Ståhl, G., Holm, S., Gregoire, T.G., Gobakken, T., Næsset, E. and Nelson, R., 2011. Model-based inference for biomass estimation in a LiDAR sample survey in Hedmark County, Norway. *Canadian journal of forest research*, *41*(1), pp.96-107.

Ståhl, G., Saarela, S., Schnell, S., Holm, S., Breidenbach, J., Healey, S.P., Patterson, P.L., Magnussen, S., Næsset, E., McRoberts, R.E. and Gregoire, T.G., 2016. Use of models in large-area forest surveys: comparing model-assisted, model-based and hybrid estimation. *Forest Ecosystems*, *3*(1), pp.1-11.

Steininger, M.K., 2000. Satellite estimation of tropical secondary forest above-ground biomass: data from Brazil and Bolivia. *International journal of remote sensing*, *21*(6-7), pp.1139-1157.

Szegedy, C., Toshev, A. and Erhan, D., 2013. Deep neural networks for object detection.

Tejada, G., Görgens, E.B., Espírito-Santo, F.D.B., Cantinho, R.Z. and Ometto, J.P., 2019. Evaluating spatial coverage of data on the aboveground biomass in undisturbed forests in the Brazilian Amazon. *Carbon balance and management,* 14(1), pp.1-18.

Tejada, G., Görgens, E.B., Ovando, A. and Ometto, J.P., 2020. Mapping data gaps to estimate biomass across Brazilian Amazon forests. *Forest Ecosystems, 7(1),* pp.1-15.

Thomas, S.C., 1996. Asymptotic height as a predictor of growth and allometric characteristics in Malaysian rain forest trees. *American journal of Botany*, *83*(5), pp.556-566.

Tyukavina, A., Hansen, M.C., Potapov, P.V., Stehman, S.V., Smith-Rodriguez, K., Okpa, C. and Aguilar, R., 2017. Types and rates of forest disturbance in Brazilian Legal Amazon, 2000–2013. *Science advances*, *3*(4), p.e1601047.

UNFCCC, 2015. Adoption of the Paris Agreement FCCC/CP/2015/10/Add.1.

U.S. Energy Information Administration, 2020. https://www.eia.gov/environment/emissions/carbon/

Van der Werf, G.R., Morton, D.C., DeFries, R.S., Olivier, J.G., Kasibhatla, P.S., Jackson, R.B., Collatz, G.J. and Randerson, J.T., 2009. CO 2 emissions from forest loss. *Nature geoscience*, *2*(11), pp.737-738.

Vaswani, A., Shazeer, N., Parmar, N., Uszkoreit, J., Jones, L., Gomez, A.N., Kaiser, L. and Polosukhin, I., 2017. Attention is all you need. *arXiv preprint arXiv:1706.03762*.

Vermote, E., Justice, C., Claverie, M. and Franch, B., 2016. Preliminary analysis of the performance of the Landsat 8/OLI land surface reflectance product. *Remote Sensing of Environment*, *185*, pp.46-56.

Wang, A.X., Tran, C., Desai, N., Lobell, D. and Ermon, S., 2018, June. Deep transfer learning for crop yield prediction with remote sensing data. In *Proceedings of the 1st ACM SIGCAS Conference on Computing and Sustainable Societies* (pp. 1-5).

Wang, M., Sun, R. and Xiao, Z., 2018. Estimation of forest canopy height and aboveground biomass from spaceborne LiDAR and Landsat imageries in Maryland. *Remote Sensing*, *10*(2), p.344.

Wang, V., Gao, J. and Schwendenmann, L., 2020. Assessing changes of urban vegetation cover and aboveground carbon stocks using LiDAR and Landsat imagery data in Auckland, New Zealand. *International Journal of Remote Sensing*, *41*(6), pp.2140-2158.

Wang, J., Sun, T., Liu, B., Cao, Y. and Zhu, H., 2021. CLVSA: A convolutional LSTM based variational sequence-to-sequence model with attention for predicting trends of financial markets. *arXiv preprint arXiv:2104.04041*.

Wangda, P., Hussin, Y.A., Bronsveld, M.C. and Karna, Y.K., 2019. Species stratification and upscaling of forest carbon estimates to landscape scale using GeoEye-1 image and lidar data in sub-tropical forests of Nepal. *International Journal of Remote Sensing*, *40*(20), pp.7941-7965.

White, J.C., Coops, N.C., Wulder, M.A., Vastaranta, M., Hilker, T. and Tompalski, P., 2016. Remote sensing technologies for enhancing forest inventories: A review. *Canadian Journal of Remote Sensing*, *42*(5), pp.619-641.

Willett, J.B. and Singer, J.D., 1988. Another cautionary note about R 2: Its use in weighted least-squares regression analysis. The American Statistician, 42(3), pp.236-238.

Wolanin, A., Mateo-García, G., Camps-Valls, G., Gómez-Chova, L., Meroni, M., Duveiller, G., Liangzhi, Y. and Guanter, L., 2020. Estimating and understanding crop yields with explainable deep learning in the Indian Wheat Belt. *Environmental Research Letters, 15(2)*, p.024019.

Wulder, M.A., Ortlepp, S.M., White, J.C. and Maxwell, S., 2008. Evaluation of Landsat-7 SLC-off image products for forest change detection. *Canadian Journal of Remote Sensing, 34*(2), pp.93-99.

Wulder, M.A., White, J.C., Nelson, R.F., Næsset, E., Ørka, H.O., Coops, N.C., Hilker, T., Bater, C.W. and Gobakken, T., 2012a. Lidar sampling for large-area forest characterization: A review. *Remote Sensing of Environment*, *121*, pp.196-209.

Wulder, M.A., White, J.C., Bater, C.W., Coops, N.C., Hopkinson, C. and Chen, G., 2012b. Lidar plots—A new large-area data collection option: Context, concepts, and case study. *Canadian Journal of Remote Sensing, 38*(5), pp.600-618.

Xu, L., Saatchi, S.S., Yang, Y., Yu, Y., Pongratz, J., Bloom, A.A., Bowman, K., Worden, J., Liu, J., Yin, Y. and Domke, G., 2021. Changes in global terrestrial live biomass over the 21st century. *Science Advances, 7*(27), p.eabe9829.

Yavaşlı, D.D., 2016. Estimation of above ground forest biomass at Muğla using ICESat/GLAS and Landsat data. *Remote Sensing Applications: Society and Environment*, *4*, pp.211-218.

Zald, H.S., Wulder, M.A., White, J.C., Hilker, T., Hermosilla, T., Hobart, G.W. and Coops, N.C., 2016. Integrating Landsat pixel composites and change metrics with lidar plots to predictively map forest structure and aboveground biomass in Saskatchewan, Canada. *Remote Sensing of Environment*, *176*, pp.188-201.

Zanne, A.E., Lopez-Gonzalez, G., Coomes, D.A., Ilic, J., Jansen, S., Lewis, S.L., Miller, R.B., Swenson, N.G., Wiemann, M.C. and Chave, J., 2009. Data from: Towards a worldwide wood economics spectrum. Dryad Digital Repository.

Zhang, L., Shao, Z., Liu, J. and Cheng, Q., 2019. Deep learning based retrieval of forest aboveground biomass from combined LiDAR and landsat 8 data. *Remote Sensing*, *11*(12), p.1459.

Zhang, J., Lu, C., Xu, H. and Wang, G., 2019. Estimating aboveground biomass of Pinus densata-dominated forests using Landsat time series and permanent sample plot data. *Journal of Forestry Research*, *30*(5), pp.1689-1706.

Zar, J.H., 1968. Calculation and miscalculation of the allometric equation as a model in biological data. BioScience, 18(12), pp.1118-1120.

Zeiler, M.D., 2012. Adadelta: an adaptive learning rate method. *arXiv preprint arXiv:1212.5701*.

Zhu, Z., Wang, S. and Woodcock, C.E., 2015. Improvement and expansion of the Fmask algorithm: Cloud, cloud shadow, and snow detection for Landsats 4–7, 8, and Sentinel 2 images. *Remote Sensing of Environment*, *159*, pp.269-277.

Zhu, Z. and Woodcock, C.E., 2012. Object-based cloud and cloud shadow detection in Landsat imagery. *Remote sensing of environment, 118*, pp.83-94.

Zwally, H.J., Schutz, B., Abdalati, W., Abshire, J., Bentley, C., Brenner, A., Bufton, J., Dezio, J., Hancock, D., Harding, D. and Herring, T., 2002. ICESat's laser measurements of polar ice, atmosphere, ocean, and land. *Journal of Geodynamics*, *34*(3-4), pp.405-445.